INFLUENCE OF SURFACE TOPOLOGY ON THE AERODYNAMICS OF RECTANGULAR CYLINDERS

By

Kian Kalan

A DISSERTATION

Submitted to
Michigan State University
in partial fulfillment of the requirements
for the degree of

Mechanical Engineering – Doctor of Philosophy

2023

ABSTRACT

Precision Airdrop Systems (PADS) face difficulties in controlling their landing accuracy when flow-induced vibrations of the suspension lines occur. Recent research has identified a previously unknown cause of these vibrations: galloping of the suspension cables. Galloping is a type of vibration that can occur in cylinders with non-circular cross-sections. The suspension cables in PADS have a cross-section that is approximately rectangular in shape with rounded corners, but with the added complexity of surface topology (due to braiding of the lines). Using load measurements, recent experiments have shown that the presence of surface topology can alter the stability of rectangular cylinders to galloping; an effect that is dependent on Reynolds numbers. Knowledge of the corresponding topology effect on the flow around the cylinders is presently lacking. Therefore, this study aims to investigate the impact of surface topology on the boundary layer and near-wake flow around a rectangular cylinder with a side-ratio of 2.5 and fully-rounded corners (half-circular leading and trailing edges). The Reynolds number based on the cylinder thickness (d) is in the range $Re_d = 800 - 2500$. The surface topology is defined using spatial Fourier modes with an amplitude of 5% of d, applied along the perimeter only (2D geometry) and along both the perimeter and the span (3D geometry) of the cylinder. While not an exact replica, this surface topology represents the characteristics of the actual suspension cable reasonably well. The study also investigates the effects of different topology amplitudes by using cylinders with 2.5% and 10% of d. Single-component molecular tagging velocimetry is employed to measure the streamwise velocity and visualize the flow field at various locations above the surface and in the wake of the cylinder.

Mean and root-mean-square velocity profiles are analyzed to examine the development of the boundary layer and separated flow on the top and bottom surfaces of the cylinder. The mean

separation bubble and the development of the shear layer unsteadiness over the surface of the cylinders are discussed at $\alpha = 0°$ and at different Reynolds numbers. The results demonstrate the Reynolds number-dependent effect of the surface topology cross-sectional geometry and its variation along the span. An interpretation is provided of how these results could influence the galloping instability of the cylinder.

The wake flow is investigated to help better understand the relationship between wake structures, surface topology, and the characteristics of the boundary layer. To achieve this, wake mean and rms velocity profiles are interrogated and the effect of the geometry on the Strouhal number of the wake vortex shedding is analyzed. An examination is also conducted to investigate the unsteady flow physics of the boundary layer and its relationship to the wake flow. This examination uses quantitative measures and flow visualization, and focuses on the smooth-surface cylinder. The analysis identifies and compares different Reynolds number dependent boundary-layer flow regimes. The correlation between the wake vortex shedding structure and various boundary-layer regimes is examined and compared to established understanding in literature for a sharp-corner rectangular cylinder.

The results reveal that the details of the topology near the leading edge of the cylinder are most significant in affecting the behavior of the boundary layer flow. For the particular topology wavelength used in the present study, the biggest effect is found when a topology peak is present at the leading edge for the 2D (2Dp) geometry. In comparison to the smooth cylinder, the 2Dp topology substantially increases the separation zone thickness and the separated shear layer unsteadiness. The ensuing wake flow, exhibits an increased wake closure length, slower recovery of the mean centerline velocity, lower vortex shedding Strouhal number, and disrupted wake vortex organization.

ACKNOWLEDGMENTS

To my

Parisa

parents, Mohammadreza and Robab

siblings, Keihan and Aysan

advisors: Dr. Ahmed Naguib and Dr. Manoochehr Koochesfahani

committee: Dr. Mohsen Zayernoori and Dr. Phanikumar Mantha

lab mates: Dr. Mark Feero, Dr. David Olson, Dr. Alireza Safaripour, Dr. Mitchell Albrecht, Dr. Basil Abdelmegied, Borhan Alhosseini, and Dr. Patrick Hammer

undergraduate mentor: Dr. Behshad Shafii

dearest friends

and College of Engineering and Department of Mechanical Engineering, especially Dr. Katy Colbry

It was impossible without you.

Thank you!

TABLE OF CONTENTS

Chapter 1. Introduction

1.1 Motivation

Geometries with non-circular cross-sections are susceptible to large-amplitude self-sustained vibration known as galloping, which arises from fluid forces induced by structural vibration in a fluid flow. Transverse, or plunge, galloping occurs when the orientation of the geometry to the oncoming flow changes, resulting in changes in the aerodynamic forces. Winter winds can induce galloping in ice-coated power lines, as can they do so in bridge decks, skyscrapers, etc. Marine structures are not safe from galloping in the ocean current and, specifically motivating the current study, suspension cables of US Army precision airdrop systems (PADS) are seen to suffer from this aeroelastic instability which deteriorates the controllability and the accuracy of the army airdrop cargo delivery [1, 2].

An elastically mounted round-corner rectangular cylinder allowed to have an oscillatory motion in y direction due to an environmental disturbance is shown in Figure 1. The oscillatory motion velocity ($\dot{y}$) in the transverse direction will change the effective angle of attack α, or AoA, with time, thereby changing the lift (F_L) and drag (F_D) forces. The corresponding change in the transverse force (F_y) coefficient with α can be calculated from the lift and drag coefficients from Equation (1).

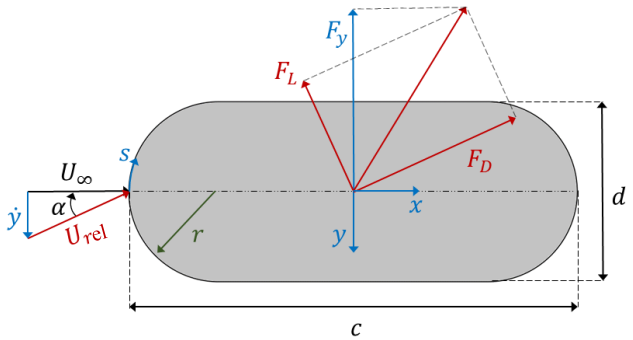

Figure 1. Schematic of the cross-section of the cylinder with zero amplitude topology and forces acting on it upon oscillating in the transverse (y) direction.

$$C_y = \frac{F_y}{0.5\rho {U_\infty}^2 dl} = -\frac{1}{\cos^2 \alpha}(C_L \cos \alpha + C_D \sin \alpha), \quad (1)$$

where the lift and drag coefficients (C_L and C_D, respectively) are calculated as below:

$$C_L = \frac{F_L}{0.5\rho U_{rel}^2 dl}, \quad (2)$$

$$C_D = \frac{F_D}{0.5\rho U_{rel}^2 dl}. \quad (3)$$

In the above equations, U_∞ and U_{rel} are the steady freestream and the instantaneous oncoming (relative to the moving cylinder) velocities, respectively, where

$$U_{rel} = \sqrt{U_\infty^2 + \dot{y}^2}, \quad (4)$$

is the magnitude of the vector difference between the freestream velocity and the cylinder velocity $\dot{y} = dy/dt$, ρ is the fluid density, d is the cylinder width, and l is the cylinder span. Galloping can occur when F_y increases with increasing the angle of attack; hence, reinforcing the oscillation and making the structure unstable [1]. Considering objects facing air flows, which is most pertinent to the PADS application, the galloping oscillation frequency is typically sufficiently smaller than that of vortex shedding f_s, in which case galloping is assumed to be quasi-steady. Accordingly, the relevant criterion for instability to galloping is based on the variation of F_y with α for a *static* cylinder [3]. This quasi-steady assumption is typically valid at high reduced velocities U_r (i.e. inverse of the non-dimensional oscillation frequency, which is the same as the structure natural frequency f_n):

$$U_r = \frac{U_\infty}{f_n d} > 20. \quad (5)$$

Another prominent mechanism for flow-induced vibration is vortex induced vibration, which takes place at a reduced velocity in the vicinity of U_R, which is the reduced velocity at which the natural

frequency of the elastic system equals the vortex shedding, or Strouhal frequency and is defined as:

$$U_R = \frac{1}{St} = \frac{U_\infty}{f_s d} \tag{6}$$

The Strouhal number, St, for the rectangular cylinders is reported by Parkinson [4] to be in the order of 10^{-1}. More specifically related to the current study, St falls within the range of (0.1-0.25) for the sharp and circular leading-edge cylinders based on the experimental studies of Okajima [5] and Parker&Welsh [6]. As a result, the reduced velocity corresponding to the vortex shedding will be in the range of (4-10).

If the cylinder is modelled as a single-degree-of-freedom mass-spring-damper system, the equation of motion for the cylinder will be in the form

$$m\ddot{y} + 2m\zeta_y\omega_y\dot{y} + k_y y = F_y = \frac{1}{2}\rho U_\infty^2 d C_y, \tag{7}$$

where m is the mass per unit span of the cylinder, ζ_y is the damping factor due to structural dissipation, k_y is the spring constant, $\omega_y = \left(\frac{k_y}{m}\right)^{1/2} = 2\pi f_y$ is the circular natural frequency of plunging, and $f_y = f_n$ is the natural frequency in Hz. For small angles of attack, α, U_{rel} and C_y can be expanded in power series as:

$$\alpha = \arctan\left(\frac{\dot{y}}{U_\infty}\right) = \frac{\dot{y}}{U_\infty} + O(\alpha^2), \tag{8}$$

$$U_{rel} = U_\infty + O(\alpha^2), \tag{9}$$

$$C_y(\alpha) = C_y|_{\alpha=0} + \frac{\partial C_y}{\partial \alpha}|_{\alpha=0}\alpha + O(\alpha^2). \tag{10}$$

At $\alpha = 0$, the lift direction is parallel to the galloping direction and the force coefficient in the y direction is equal to the negative lift coefficient, $C_y(\alpha = 0) = -C_L(\alpha = 0)$; see Equation (1). Substituting for this in Equation (10) and using the result, up to linear power in α, to replace C_y in Equation (7), yields:

$$m\ddot{y} + 2m\omega_y(\zeta_y - \frac{\rho U_\infty d}{4m\omega_y}\frac{\partial C_y}{\partial \alpha}|_{\alpha=0})\dot{y} + k_y y = -\frac{1}{2}\rho U_\infty^2 dC_L|_{\alpha=0} \quad (11)$$

Setting the term in parentheses on the left-hand side of Equation (11) to

$$\zeta_T = \zeta_y - \frac{\rho U_\infty d}{4m\omega_y}\frac{\partial C_y}{\partial \alpha}|_{\alpha=0}, \quad (12)$$

the net damping factor (including both structural and fluid damping), the solution to Equation (11) will be:

$$y = \frac{\frac{1}{2}\rho U_\infty^2 dC_L|_{\alpha=0}}{k_y} + A_y e^{-\zeta_T \omega_y t}\sin\left[\omega_y(1-\zeta_T^2)^{\frac{1}{2}}t + \phi\right], \quad (13)$$

where, A_y is the amplitude of oscillation and ϕ is the corresponding phase shift. As seen from the solution, the stability condition, determining whether the oscillations increase over time, depends on the net damping coefficient sign ζ_T. If $\zeta_T > 0$, vibrations would decay with time and the stability condition is met. Equivalently, referring to Equation (12), the model is stable if

$$\frac{\partial C_y}{\partial \alpha}|_{\alpha=0} < 0, \quad (14)$$

and otherwise it can be unstable. Specifically, if $\frac{\partial C_y}{\partial \alpha} > 0$, a critical velocity can be found above which the net damping coefficient becomes negative, which marks the onset of plunge galloping instability. The critical reduced velocity is found by setting $\zeta_T = 0$ in Equation (12), leading to:

$$\frac{U_{crit}}{f_y d} = \frac{4m(2\pi\zeta_y)}{\rho d^2} \Big/ \frac{\partial C_y}{\partial \alpha}|_{\alpha=0}. \quad (15)$$

1.2 Literature Review

Suspension lines of precision airdrop systems have been recently shown to be susceptible to galloping [1, 2]; with possible consequent negative effect on the performance and the controllability of PADS. The cross-section of these suspension lines is typically non-circular and resembles a rectangle with rounded corners, as given in Figure 1. Additionally, due to braiding, the surface of the lines is not smooth, but is rather characterized by topological surface height

variations [1, 2]. Thus, it is important to understand the effect of the surface topology of these suspension lines on their aeroelastic behavior; specifically, their static $C_y - \alpha$ characteristics. Siefers et al. [2] observed that a Dacron cable at low Reynolds numbers can show low-frequency vibrations, at a much lower frequency compared to that based on the vortex shedding Strouhal number they measured in the wake of the object. They hypothesized that galloping is the dominant form of instability leading to the suspension line vibration, but this hypothesis needed to be assessed by directly measuring the aerodynamic loads acting on the line.

In a recent study, Feero et al. [7, 8] observed that the presence of the surface topology can change the galloping stability of cylinders of the same geometry, as shown in Figure 2, somewhere in the Reynolds numbers $Re_d = U_\infty d/\nu$ of 1100 to 2500 which is within the relevant range for PADS (1000 to 10000). These conclusions were made based on measurement of the mean transverse force coefficient (C_y) variation with AoA for the cylinders. More specifically, referring to Figure 2-left, at Re_d=1100, the smooth cylinder shows negative slope of C_y at α=0°; meaning that galloping could not occur. On the other hand, the cylinder with surface topology (Figure 2-right) shows a positive slope at the same Reynolds number; i.e., susceptibility to galloping. At $Re_d = 2500$ and higher Reynolds numbers, both cylinders behave similarly, exhibiting stability to galloping. Thus, the effect of surface topology on galloping instability of the cylinders is Reynolds number dependent.

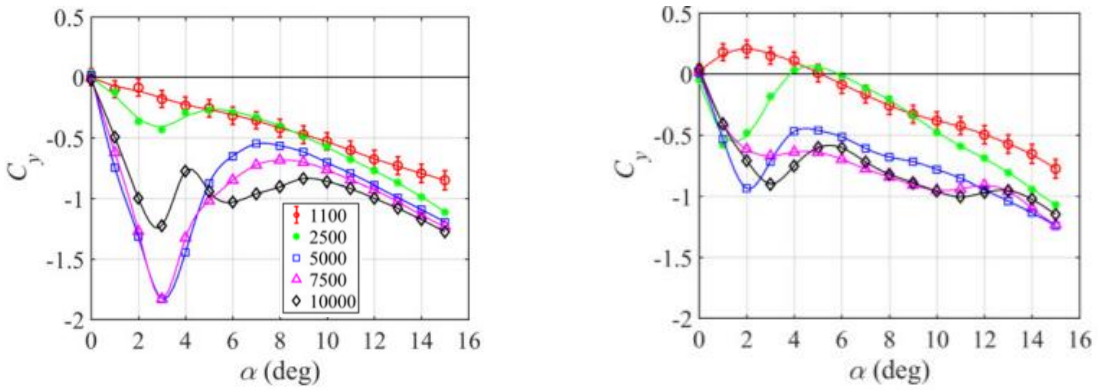

Figure 2. Galloping force coefficient characteristics of the smooth cylinder (left) and the cylinder with surface topology (right) reported in [7, 8] in a different test facility. Legend shows Re_d values.

It is well established in the literature that galloping instability of bluff bodies is closely connected to the separation and reattachment behavior of the boundary layer. Rectangular cylinders with *sharp corners*, whose galloping characteristics are one of the most studied, are prone to galloping when their side-ratio falls within $0.75 < c/d < 3$ (where c is the cylinder chord as defined in Figure 1). In a review paper, Parkinson [4] explains that the link between galloping instability and side-ratio for these cylinders lies in the body length downstream of the boundary layer separation point. Knowing that the shear layer separation occurs at the sharp corners of the leading edge, the afterbody of the cylinders with side-ratio less than 0.75 is too short that the separated shear layer and its vortices are not able to interact with the cylinder lateral surface and exert pressure distribution favorable for galloping. When the side-ratio is large enough (approximately $c/d \geq 3$), the separated shear layers reattach to the lateral surfaces of the cylinder before finally separating at the sharp corners downstream and there is no afterbody for the separated shear layer vortices to interact with the cylinder sides. Therefore, these cylinders show stability to galloping.

Given the generally small number of studies for the cylinders at relatively low Reynolds numbers ($Re_d \leq 10^4$), Feero et al. [9] conducted a study on the rectangular cylinders with sharp

corners and side-ratio c/d range of $1-3$. They observed that when the Reynolds number is sufficiently low, in their case below 5000, even the cylinder with long afterbody is prone to galloping. From the surface pressure data, they observed that the reattachment point on the bottom side surface of the cylinder does not move with increasing α from $0°$ to $5°$ where the force data indicates positive $C_y - \alpha$ slope. The opposite of this behavior is observed at higher Reynolds numbers where the separation bubble on the bottom side is seen to shrink in length with α. They, therefore, hypothesized that the separated shear layer reattachment on the bottom side of the cylinder is necessary but not sufficient to prevent galloping instability. For stability, the separation bubble length has to shrink with increasing α as well. Interestingly, they also observed that below $Re_d = 5000$, increasing the side ratio in the range of 1-3 results in higher instability to galloping which is deduced from higher $C_y - \alpha$ curve slope (corresponding to lower critical reduced velocity; see Equation 15).

Carassale et al. [10] studied square cylinders ($c/d = 1$) with sharp and round corners with r/d of 0.067 and 0.133 at high Reynolds numbers $Re > 10^4$. They observed that above a critical Reynolds number and in a turbulent freestream, the separating shear layer behavior on the top side of the cylinder with the largest corner radius plays a significant role in determining the lift coefficient. They found that the shear layer reattaches to the top and bottom surfaces of the cylinder at small α notwithstanding the very short afterbody length. In addition to this so-called supercritical behavior, surface pressure measurements also indicate shrinkage of the separation bubble on the bottom side with α, resulting in more pressure recovery and lift increase. The separation bubble on the top surface, on the other hand, lengthens and exerts higher suction which contributes to even more lift. Therefore, considering that $C_L \approx -C_y$ at small α, lift increasing with α is opposing to the favorable conditions to galloping and the geometry is stable. When α is large

enough, the separated shear layer on the top side is not able to reattach and suction drops and the lift coefficient decreases with α (i.e., C_y increases with α). The latter behavior is similar to that at sub-critical Reynolds numbers starting from $\alpha = 0$ for the case of a laminar freestream.

1.3 Scope of the Current Study

Understanding the flow field associated with galloping instability of the PADS' suspension lines motivates the current study. The main focus of the current work is on understanding the boundary layer development on the cylinder surface, and how this development is affected by the surface topology and Reynolds number. A range of geometries is studied to systematically investigate and distinguish the effects of cross-sectional geometry, topology amplitude, and presence of topology variation along the span. This investigation is carried out in a water tunnel in the Reynolds number range $Re_d = 800 - 2500$, which is pertinent to the galloping problem of PADS. The same range has been examined, *from force characteristics perspective only*, in the wind tunnel, as discussed above [7, 8]. However, it is important to note that the flow and the force characteristics in two different test facilities may be different notwithstanding matching of Re_d. Such differences may be caused by discrepancies in freestream turbulence intensity, cylinder aspect ratio, model end conditions, and test section blockage. For this reason, complementary force measurements were done by a collaborator on the same cylinder models and experimental setup employed in the present study [11]. These results, included here in Figure 3 for reference, show that similar to the data in Figure 2-right, the present cylinder model with topology is unstable to galloping at $Re_d = 1100$, but it is stable at $Re_d = 2400$. The crossover point appears to be at $Re_d = 1800$.

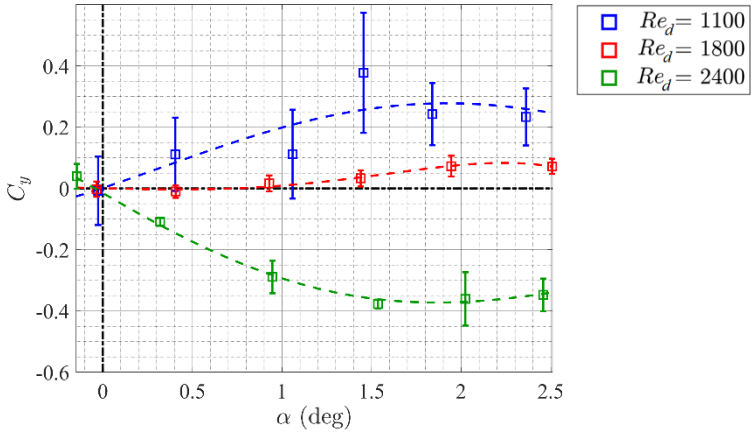

Figure 3. Comparison of the $C_y - \alpha$ behavior for the cylinder with surface topology similar to [7, 8] for Re_d = 1100, 1800 and 2400 [11].

In addition to investigating the boundary layer, the wake of the cylinder is also examined at $\alpha = 0°$ in the same Reynolds number range used for the boundary layer study. The main focus for the wake results presented here is to measure the vortex shedding frequency for the cylinders, with versus without topology, given the relevance of this knowledge to the possibility of interaction of galloping with vortex induced vibrations (in which case quasi-steady analysis is not accurate). The connection between the boundary layer/separated shear layer behavior with the wake, and the initial wake width with the shedding frequency are also investigated in this work.

1.4 Outline

The discussions from here on are organized in four chapters. Flow facility and experimental techniques are introduced in Chapter 2, where the procedure for 3D printing the test models are explained, the implementation of single-component molecular tagging velocimetry (1-c MTV) and the characterization of uncertainties are outlined, and the image processing approaches are described.

The primary results are categorized and discussed in three chapters. Chapter 3 focuses on the streamwise-velocity mean and rms characteristics of the boundary layer flow over the

cylinders. In this chapter, the effect of the complex surface topology on the boundary layer flow is broken into sub-problems by separately studying the effect of topology amplitude, cross-sectional feature, and variation along the span. Furthermore, Chapter 3 investigates how the effect of different surface topology features on the boundary layer flow undergoes changes with varying the Reynolds number. Finally, based on the current understanding in literature of the connection between the boundary layer flow behavior and instability of the cylinders to galloping, the effect of different surface topology features and Reynolds number on the stability of the cylinders will be analyzed. Chapter 4 focuses on the wake flow of the cylinders and how the mean and rms characteristics of the streamwise velocity in the wake of the cylinders are affected by the surface topology features. The vortex shedding frequency and how it is affected by the surface topology will be studied against Reynolds number in this chapter. In Chapter 5, the investigation will focus on unsteady flow characteristics in an effort to gain a deeper understanding of the connection between the boundary layer and wake flow. The study will utilize flow visualization techniques and conduct additional statistical analysis to characterize various flow regimes. Subsequently, the phase-averaged velocity in the wake will be analyzed for each flow regime.

Chapter 2. Experimental Techniques

2.1 Flow Facility and Test Models

The experiments are conducted in a closed-return, free-surface water tunnel (Engineering Laboratory Design, ELD, Model 502 6") in the Turbulent Mixing and Unsteady Aerodynamics Laboratory (TMUAL) at Michigan State University. The contraction ratio between the settling chamber and the test section of this tunnel is 6:1. The impeller circulating the water in the tunnel is driven by an electric motor, controlled by a TOSHIBA VF-S9 inverter which facilitates accurate setting of the tunnel flow speed. The test section dimensions are 152 mm × 152 mm × 457 mm. An additional flow management in the form of a 38.1 mm (1.5") long honeycomb with 3.2 mm (1/8") diameter cells is implemented downstream of the contraction section with its downstream face located about 13 mm (0.5") upstream of the start of the plexiglass test section. This was done to reduce the turbulence level of the tunnel below that achievable with flow conditioning upstream of the contraction alone. Installation of this extra honeycomb has shown to decrease the turbulence (rms) level of the tunnel and improve the uniformity of the freestream mean velocity profile across the tunnel (Kalan's M.S. project [12]). The tunnel was operated for several hours before the measurements were done to make the water temperature as uniform and steady as possible. Due to possible room temperature variations, water temperature in the test section was measured with a calibrated Omega 450 ATH thermometer equipped with a T-type thermocouple with $\pm 0.2°$ C accuracy before each experiment. The actual tunnel speed was then set to meet the target Reynolds number based on the kinematic viscosity value at the measured water temperature. It is noteworthy that the tunnel temperature was again measured after each experiment to confirm that no considerable temperature difference had occurred during the measurements. In all cases, the tunnel temperature variation before and after the measurements was within the thermocouple accuracy.

Placement of the model in the test section results in a 9.8% geometrical blockage (at $\alpha = 0°$). The measurements are performed at $Re_d = 800, 1100, 1400, 1800$ and 2500, corresponding to $U_\infty = 4.7, 6.5, 8.3, 10.7,$ and 14.8 cm/s respectively, at water temperature of 25°C, where freestream turbulence level of the tunnel is found to be below $1.7\%, 1.5\%, 1.4\%, 1.2\%,$ and 1% for the aforementioned Reynolds numbers, respectively. No effort is made to decompose the turbulence fluctuations into slushing and broadband components.

The models are 3D printed cylinders with a 11.4 mm-diameter (7/16") tight-tolerance multipurpose stainless-steel rod inserted along their centerline to prevent warping. This shaft extends beyond the cylinder's span on one end, passing through a skimmer plate (Figure 4), and is clamped to a closed-loop Applied Motion Products TSM17Q-1RG stepper motor with encoder that controls the angular position of the cylinder, and hence the AoA of the model, with an angular resolution of 0.02°. The cylinder mounting setup is built on a rigid structure isolated from but assembled around the water tunnel to prevent the transfer of any possible vibrations from the tunnel to the cylinder.

A Plexiglass skimmer plate, spanning 76 mm (5.1d) upstream and downstream of the model's center, is utilized to provide a well-defined wall boundary condition at the free surface of the test section. There is a 0.5 mm clearance between the ends of the cylinder and both the tunnel bottom surface and the skimmer plate. The streamwise position of the cylinder is such that its centerline is 13.3*d* downstream of the test section entrance.

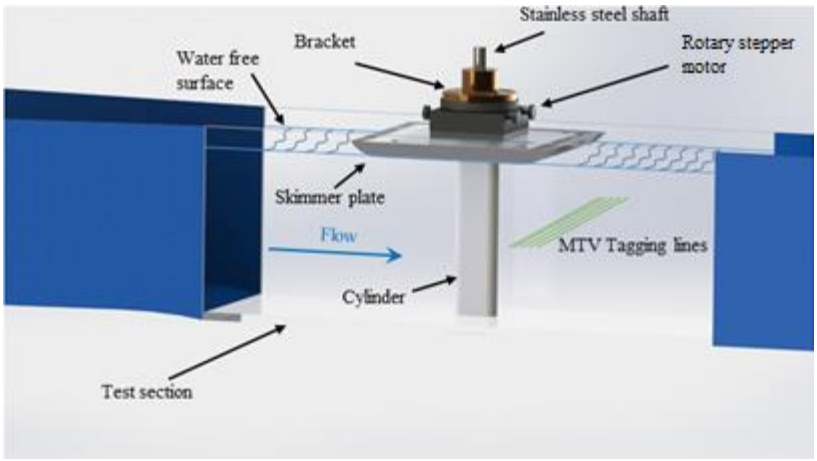

(a)

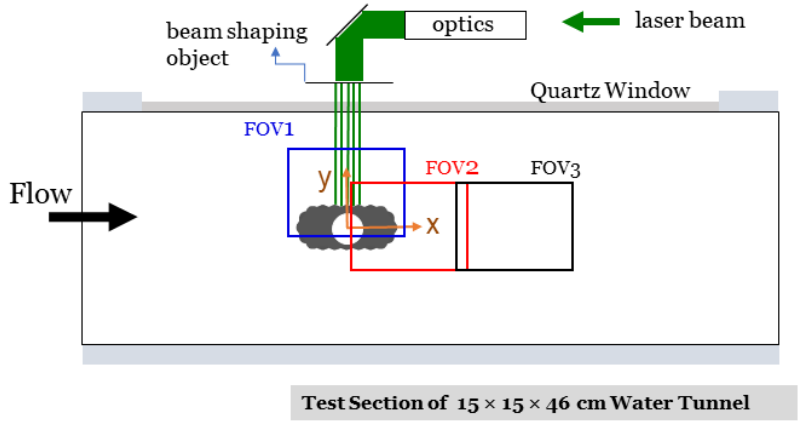

(b)

Figure 4. (a) 3D model of the experimental setup in the test section. (b) Schematic of the top view of the optical system for 1c-MTV measurements and the tunnel test section. Imaging fields of view (FOV) utilized for MTV measurements are indicated on the schematic.

An idealized definition is used to prescribe the surface topology of the test cylinder, instead of using a replica of an actual PAD suspension line's geometry. This is motivated by two factors: first, the present study aims at providing general basic understanding of the effect of surface topology independent of specific applications; second, the idealized topology is defined precisely using two-dimensional Fourier-mode synthesis. Specifically, the topology ε (see Figure 5), which is the deviation of the cylinder surface from the baseline smooth cylinder cross-section (depicted in Figure 1 and Section A-A in Figure 5), is given as follows:

$$\varepsilon = \frac{\varepsilon_0}{2}\left[\cos\left[2\pi\left(\frac{s}{\lambda_s} + \frac{z}{\lambda_z}\right)\right] + \cos\left[2\pi\left(\frac{s}{\lambda_s} - \frac{z}{\lambda_z}\right)\right]\right], \quad (16)$$

where s is the wall-tangential coordinate defined along the surface of the *baseline* (*smooth*) model (see Section A-A in Figure 5), z is the coordinate along the span of the cylinder, ε_0 is the topology amplitude, and λ_s and λ_z are the topology wavelengths in s and z directions, respectively (see Figure 5). The wavelength along the s direction is equal to P/n with P and n being the baseline model's perimeter, and the integer number of topology wavelengths around the perimeter, respectively.

The values of the geometric parameters of the test models are selected such that they approximate the Dacron parachute suspension line used by Siefers [13]. This typical suspension line has the following geometrical parameters: $c/d \approx 2.4$, $r/d \approx 0.4$, $\varepsilon_0/d \approx 5\%$, and a 24-strand braid. For the cylinder models used here, the cross-sectional dimensions of the baseline (smooth surface) model give a side ratio $c/d = 2.5$, and a fully-round LE and TE, $r/d = 0.5$ (see Figure 1 for definition of terms). $\lambda_z/\lambda_s = 1.5$ and $n = 10$ are chosen based on counting the number of wavelengths around the perimeter of the Dacron line and measuring the peak to peak distance along the span. Different topology amplitudes of $\varepsilon_0/d = 2.5\%, 5\%$ and 10% are investigated, with the $\varepsilon_0/d = 5\%$ case being the closest to the actual Dacron cable.

The test models are enlarged by a factor of 7.7 relative to the actual Dacron cable scale, where the width, chord, and corner radius are $d = 15$ mm, $c = 37.5$ mm, and $r = 7.5$ mm, respectively. The span of the models is $l = 139.6$ mm, which extends over the full height of the test section and results in an aspect ratio l/d of 9.3.

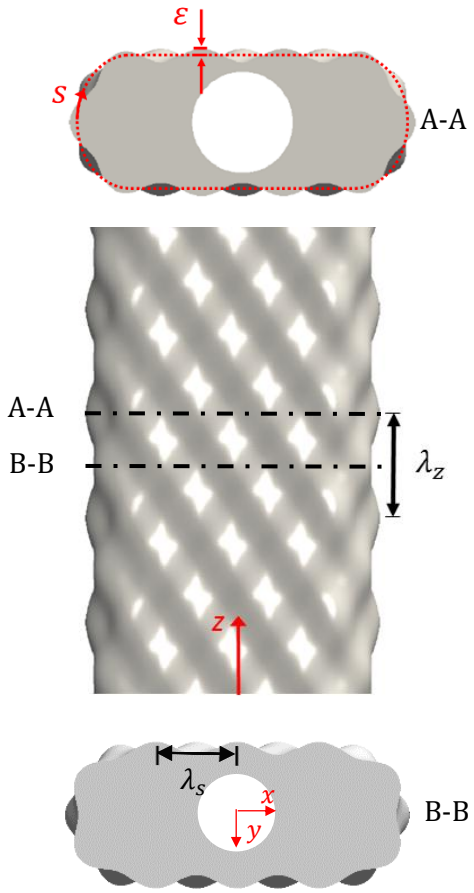

Figure 5. Top and cross-sectional views of the cylinder with ε_0/d =5%, n=10, and λ_z/λ_s=1.5.

To systematically study the effect of the surface topology, several models are investigated, in addition to the main geometry shown in Figure 5. A model with zero topology amplitude (i.e. smooth cylinder) is employed as a baseline case. A second set of models is made with surface topology, where the cross-section is constant along the whole span ($\lambda_z = \infty$). This set, which is referred to as the 2D set, includes two different cross-section shapes: one with a peak in the topology at the LE, and the other with a valley. These "peak-leading" and "valley-leading" shapes are the same as cross-sections A-A and B-B, respectively, of the 3D cylinder geometry in Figure 5. The 2D models are used to study the effect of the topology on the flow in the absence of flow three-dimensionality induced by the spanwise waviness of the topology. Comparing results from the 2D models to those from the 3D model is expected to provide insight into the significance of

the spanwise variation of the topology. For the 3D geometry, measurements are done at two spanwise planes corresponding to sections A-A and B-B in Figure 5. These cases are indicated as 3Dp and 3Dv respectively, where the p and v in the notation signify the presence of a peak and a valley, respectively, at the cylinder's leading edge. The corresponding 2D model cases are denoted as 2Dp and 2Dv, respectively.

Models following the prescribed surface topology are 3D printed by an Objet Connex350 multi-material 3D printing system. The nominal resolution of this printer is 30 microns along y axis and 100 microns along x and z axes as defined in Figure 5. The material used to print the cylinders is Stratasys RGD450 Rigur which is a rigid opaque white material. Given that the readable input file format to this 3D printer is '.stl', the cylinders should be designed in a way that can be further translated to this format. The process of doing so is that the surface topology is defined mathematically in MATLAB (see code in Appendix) and discrete points are generated to make a point cloud which is afterwards introduced to SolidWorks software in text '.txt' format. In this software, this point cloud is transformed into a mesh by the 'mesh prep wizard' feature. It is possible then to save this mesh as a .stl file. However, no manipulation can be directly done on this mesh in SolidWorks and any change has to be done to the main point cloud. In the course of the study, manipulation of the mesh became necessary to generate a through hole for fitting a metallic shaft in the 3D printed cylinders in order to reinforce them. These sorts of alterations are much easier to conduct in a CAD software in comparison to defining them mathematically in the process of point cloud generation. To go around this issue, the '.stl' file was loaded into SpaceClaim software which is an Autodesk product. This software provides capability of making a concentric through hole inside the cylinders with the desired diameter.

Accuracy of the 3D printed objects is investigated using a KEYENCE VR3200 3D scanner device. The accuracy of this device in surface height measurements is $\pm 2\mu m$. The measurements are done on the surface of a cylinder with a 3D surface topology that is close but not identical to the models used in the measurements. Specifically, some parameters such as ratio of the wavelengths and corner radius are slightly different, but the topology amplitude is the same. This cylinder is used in preliminary studies. The results shown in Figure 6 are samples of the measured surface profiles, on one of the sides and one of the edges of the cylinder, compared with the design topology profile produced by the mathematical definition. Since the resolution of the 3D printer is better along the y-axis, as seen in Figure 6, a better surface quality of the 3D printed cylinder is obtained on the side of the cylinder than along the edge. The rms deviation from the design profile is 2.3% and 10.5% of the design wave amplitude on the side and along the edge, respectively and it can be seen that, overall, the printed geometry is satisfactory and follows the intended profile.

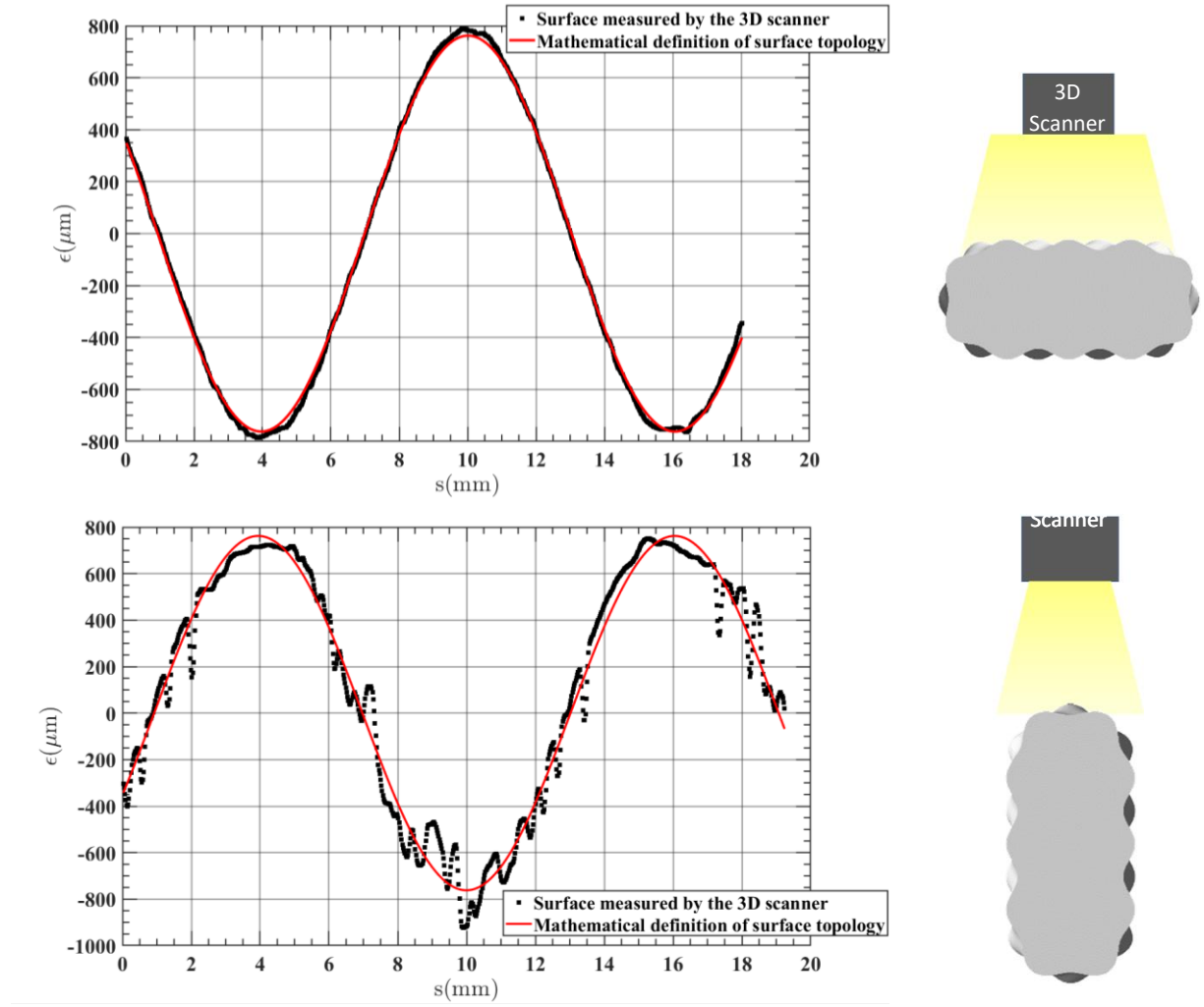

Figure 6. Accuracy of the 3D printed object. Surface measured by the scanner is compared to the design sinusoidal wave.

2.2 Molecular Tagging Velocimetry

One-component molecular tagging velocimetry (1c-MTV) is utilized to measure the flow velocity. MTV is a whole-field non-intrusive measurement technique that relies on using a flowing medium premixed with molecules that can be turned into long-lifetime tracers upon excitation by photons of a particular wavelength [14, 15]. Typically, a pulsed laser is used to "tag" the regions of interest, and those tagged regions are interrogated at two successive times within the lifetime of the tracer to make an image pair of so called 'delayed' and 'undelayed' images as seen in Figure 7.

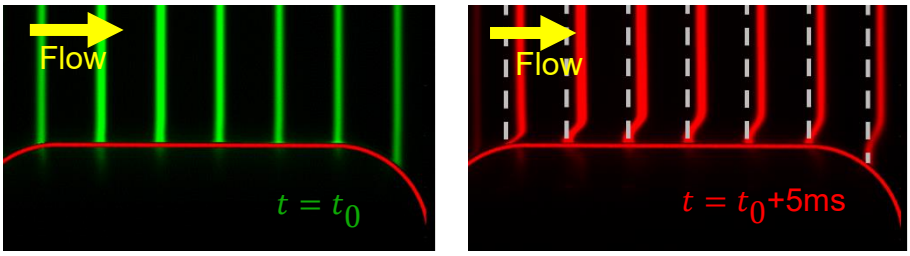

Figure 7. 1c-MTV images. 'delayed' image on the right is taken 5ms after capturing the 'undelayed' image on the left. The lines have been colored to enhance their visibility.

The present implementation of MTV employs a phosphorescent supramolecule tracer [14] with chemical composition of 1×10^{-4} M of maltosyl-β-cyclodextrin, 0.055 M of cyclohexanol, and $\sim 1 \times 10^{-5}$ M of 1-bromonaphthalene, which assures its solution saturation. The tracers are excited by a Lambda Physik LPX 210i XeCl 308 nm UV excimer laser. The discharged rectangular laser beam passes through a pair of coated converging spherical lenses to form a travelling parallel beam, that is then steered through a set of coated mirrors toward the tunnel test section. Prior to entering the test section, the parallel laser beam passes through a pair of converging cylindrical lenses. This process creates a thin laser sheet with a thickness of less than 1 mm across the tunnel test section. Laser lines are formed after the laser sheet passes through a beam shaping object, as depicted Figure 4-b. The beam shaping object is a thin metal sheet with a custom pattern of vertical narrow slots to form the desired tagging pattern. For the present work, between 28 to 38 tagged lines are oriented to measure the streamwise velocity component with a spacing of $0.08d$ in the streamwise direction. The individual tagging lines, being as narrow as about 0.7 mm each (based on full width $1/e^2$), enter the test section on the side where quartz window inserts are installed. Other test section walls are made out of Plexiglas, which enables imaging of the molecular emission while blocking the UV laser light from exiting the test section. The optical system is positioned on a manually movable three-degree-of-freedom traversable optics bench, which is mounted on the tunnel but kept separate from it to prevent the transmission of tunnel vibrations.

One-component MTV measures the Lagrangian displacement of the fluid particles in the direction normal to a tagging line at every pixel along the line, providing one component of the flow velocity at very high spatial resolution. The technique for calculating the line displacement using spatial correlation is described in [16]. For the present work, the tagged lines are oriented to measure the streamwise velocity component with a spacing of 40 μm ($0.003d$) along each of the lines. This high spatial resolution makes 1c-MTV particularly suited for boundary-layer-resolved measurements. Three fields of view (FOV) are adopted for data acquisition by translating the optical tray downstream (see Figure 4-b). The first one stretches between $x/d =$ -1.15, near the leading edge (LE), to $x/d =$ 1.15, near the trailing edge (TE) to measure the boundary layer flow. Its cross-stream dimension extends from $y/d \approx -0.5$ to 1.9 focusing on the boundary layer flow. The second field of view, stretching between $x/d \approx$ 0.17 and 3.80 covers the downstream half and the immediate wake of the cylinder to allow simultaneous boundary layer and the near wake measurements. Finally, the third field of view covers the wake farther downstream from $x/d \approx$ 2.97 up to 6. The implementation of overlapping fields of view enables precise alignment and assembly of the results. The latter two fields of view stretch between $y/d \approx -1.2$ and 1.2 in the cross-stream direction to symmetrically capture the wake flow.

There are different sources of uncertainty contributing to the accuracy of the measurements. Among them, laser pulses inconsistency and possible vibrations of the setup, along with MTV settings such as signal to noise ratio SNR, correlation window size, tagging line thickness and spacing, line shape, etc. can affect the subpixel accuracy [16]. Furthermore, the delayed images can be correlated to a single undelayed image, as in the current study, which is usually a time-average image from a time series of instantaneous undelayed images. This assumption is only valid when the variations between the instantaneous and average undelayed

images are small. Correlating the instantaneous undelayed images with their temporal average gives an estimation of the total uncertainty of the measurements, or subpixel accuracy, introduced by the above-mentioned sources. Such analysis is conducted with the instantaneous undelayed images acquired at a SNR representative of the delayed images of the velocity measurements. Subpixel accuracy of the measurements in terms of rms are calculated to be around 0.16 pixels.

The undelayed image is taken $1\ \mu s$ after the laser pulse to avoid capturing the florescence emission of the tracers. The time delay Δt between the two MTV images (undelayed and delayed) changes between different Reynolds numbers from 8ms for $Re_d = 800$ to 3.5ms for $Re_d = 2500$. The exposure time of the images is set to 10% of the time delay Δt. The time delay is customized for each Reynolds number to ensure proper pixel displacement of the tagged region during the time delay. The exposure time is adjusted accordingly to maintain the highest possible SNR, and simultaneously minimize the pixel displacement during the exposure. 3072 images are acquired at the lower Reynolds numbers $Re_d = 800$ and 1100, and for the remaining Reynolds numbers, 2048 images are acquired at a sampling rate of 7 Hz. The duration of the time series corresponds to a convective time scale of $1375\ d/U_\infty$ for $Re_d = 800$ and $2977\ d/U_\infty$ for $Re_d = 2500$. Based on the shedding frequency measured at the far wake, by calculating power spectral density from velocity time series, this corresponds to about 290 and 610 shedding cycles at the lowest and highest Reynolds numbers, respectively. A pco.pixelfly camera equipped with a Nikon Nikkor 58mm f/1.2 lens and an 11 mm Nikon extension ring is utilized for image acquisition.

The camera has a 14-bit charge-coupled device (CCD) sensor with a resolution of 1392 × 1040 pixels and a pixel size of $6.45\ \mu m \times 6.45\ \mu s$. The maximum acquisition frequency at the maximum frame size without any pixel binning is about 7 frames per second.

Statistical convergence uncertainty, which is another important source of uncertainty, is reported in Table 1, for the largest uncertainty over the entire measurement domain. The uncertainties are reported as % of U_∞ for the mean velocity and % of the local u_{rms} for the rms velocity, calculated based on the work of Benedict and Gould [17]:

$$\sigma_{\overline{U}} = \frac{u_{rms}}{\sqrt{N}}, \tag{17}$$

$$\sigma_{u_{rms}} = \frac{u_{rms}}{\sqrt{2N}}, \tag{18}$$

where N is the number of the independent samples and is taken here to be the number of the vortex shedding cycles occurring in the duration of the time series.

Table 1. Convergence uncertainty of mean and rms velocity measurements as percentage of U_∞ and local u_{rms}, respectively.

	$Re_d = 800$	$Re_d = 1100$	$Re_d = 1400$	$Re_d = 1800$	$Re_d = 2{,}500$
Mean velocity	1.67%	1.97%	2.27%	2.28%	1.61%
rms velocity	4.73%	4.01%	4.46%	4.13%	3.17%

Convergence uncertainty of the mean displacement and velocity due to the subpixel accuracy, are estimated to be 0.012 pixels and 0.1% of U_∞, respectively. Convergence uncertainty of the rms displacement due to the subpixel accuracy is calculated to be 0.009 pixels which corresponds to 0.075% of U_∞.

Chapter 3. Boundary Layer Statistics - Mean and rms Velocity

The current study aims to reveal the underlying flow physics related to the complex geometry of the rectangular cylinders with round corners and surface topology. This should ultimately provide fundamental understanding of the unique behavior of these cylinders at low Reynolds numbers, as reported in the previous studies [7, 8]. As a step towards this goal, this chapter covers results related to the streamwise velocity field in the boundary layer of the cylinders. In the following sections, mean and rms velocity profiles and color contour maps from MTV measurements along the surface of the cylinders will be discussed. The focus of Sections 3.1 through 3.3 will be on the boundary layer measurements carried out at the angle of attack α = 0°. In order to distinguish the effects of the cross-sectional geometry on flow behavior from those due to shape variation along the span, Section 3.1 will focus on the 2D geometries, with the amplitude pertinent to the PADS application ($\varepsilon/d = 5\%$), and how they compare with the *baseline* smooth geometry. Section 3.2 is focused on the study of the topology amplitude effects on the flow field by comparing cylinders with lower and higher topology amplitudes than the PADS application. In section 3.3, the effects of variation of the geometry along the span will be interrogated, and the cross-sections of the 3D geometry corresponding to the 2D cylinders will be discussed. In the final section of this chapter, observations pertinent to the galloping phenomenon will be presented by analyzing changes in the flow around the geometries with variation in the angle of attack.

3.1 Effect of the Cross-Sectional Geometry

In this section, the smooth cylinder, along with the 2Dp and 2Dv cylinders with $\varepsilon/d = 5\%$ at $\alpha = 0°$ will be discussed in the Reynolds number range of $Re_d = 800 - 2500$, to analyze the effect of the cross-sectional geometry on the flow behavior relevant to the application of the PADS.

A sample set of the boundary layer mean and rms velocity profiles from MTV is depicted in Figure 8. The boundary layer at the three most upstream measurement locations, up to just downstream of the round corner, appear to be attached. While not clearly visible from Figure 8, at the next downstream position, the boundary layer separates. This is determined from the presence of reversed flow near the wall. The cylinder surface glare during MTV imaging, plus the geometries' inherent curvature, does not allow accurate interrogation of a few (up to ten, depending on the specific location) pixels in the immediate vicinity of the wall. In addition, given the finite streamwise resolution of the measurements and the presence of a gap between the tagging lines, separation and reattachment locations can be better estimated from extrapolation of the separation zone boundary (to be discussed later), with an uncertainty equal to half the streamwise distance between the tagging lines which is about 4.5% of the baseline width ($\approx 0.045d$).

In addition to the separation of the boundary layer, the velocity profile also develops an inflection point, where the cross-stream velocity gradient is highest along the cross-stream direction. Above the reversed-flow region, this profile reflects the presence of a separated shear layer. From Figure 8-bottom, it can be seen that the unsteadiness grows in the shear layer as the rms velocity becomes more prominent with the downstream. The shear layer is characterized by comparing the spread of the region with the high rms velocity together with the strength of the u_{rms} peaks, and will be discussed later in this chapter. For a better visual presentation, color contour maps of these velocity data are plotted and compared for different cylinder geometries in later figures.

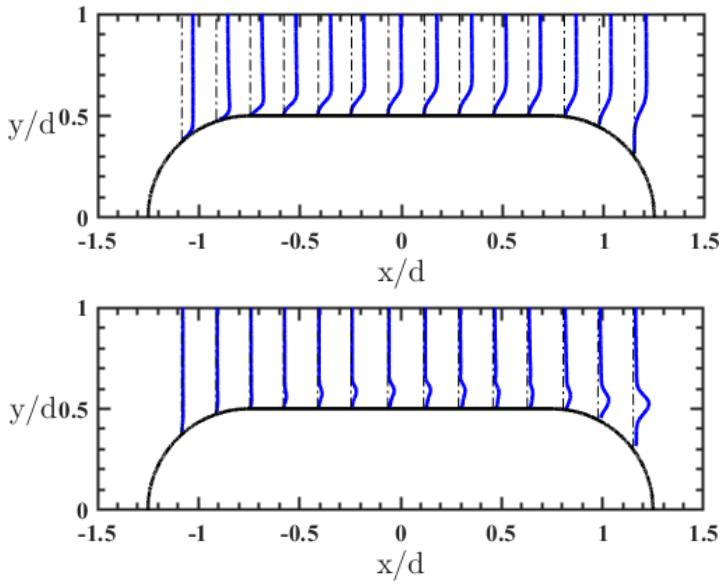

Figure 8. Boundary layer mean (top) and rms (bottom) velocity profiles on the smooth cylinder at $Re_d = 2500$. Flow is from left to right. Every other profile is shown to avoid clutter.

Figure 9 shows the normalized mean (left) and rms (right) velocity color contour maps for the smooth cylinder. In this figure, the separated flow is tracked by marking the region with reverse flow (negative velocity) in cold colors (cyan to pink spectrum).

With the current experimental resolution, the flow seems to remain fully attached at $Re_d = 1100$, but shows a minuscule closed separation bubble at $Re_d = 800$ and 1400, with the separation bubble's thickness not exceeding 2% of the baseline width d. Magnified view of these contour maps is depicted in Figure 10 to better show the separation bubbles near the surface. Increasing the Reynolds number to $Re_d = 1800$ is associated with a thin but open separation bubble, with the separation point located downstream of the leading-edge round corner. Further increase in the Reynolds number causes the flow to reattach to the surface before separating again farther downstream of the trailing edge round corner into the wake. Therefore, a non-monotonic relationship between the separation/reattachment of the boundary layer and Reynolds number is observed for the smooth cylinder in the Reynolds number range of interest. Specifically, increasing the Reynolds number first develops an open separation bubble then leads to reattached flow.

Overall, the flow follows the contour of the smooth geometry well and is not displaced significantly by the, generally thin, separation bubble from the cylinder's surface.

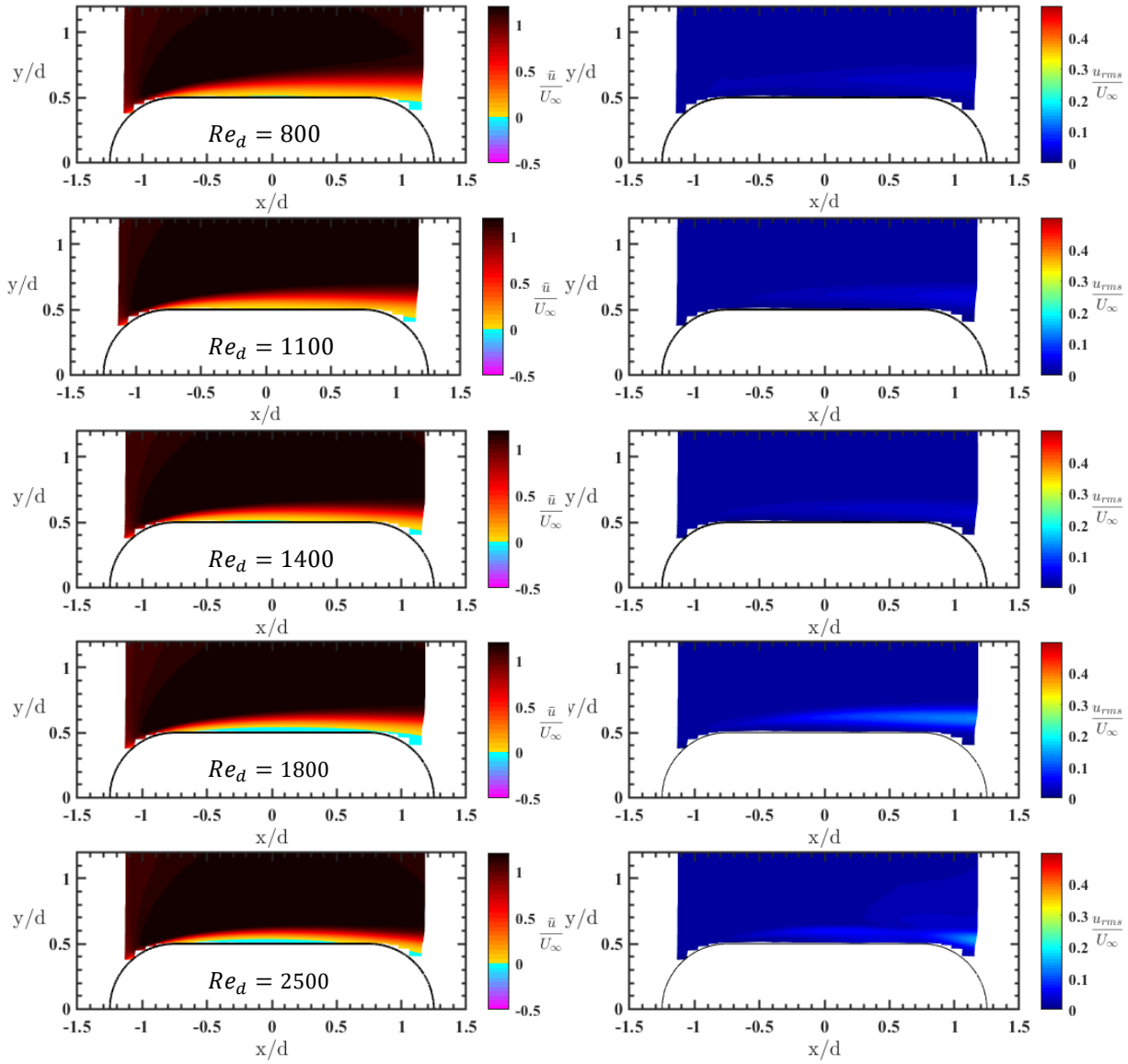

Figure 9. Smooth cylinder. Mean (left) and rms (right) velocity color contour maps normalized by the freestream velocity U_∞. Rows show different Reynolds numbers. Flow is from left to right.

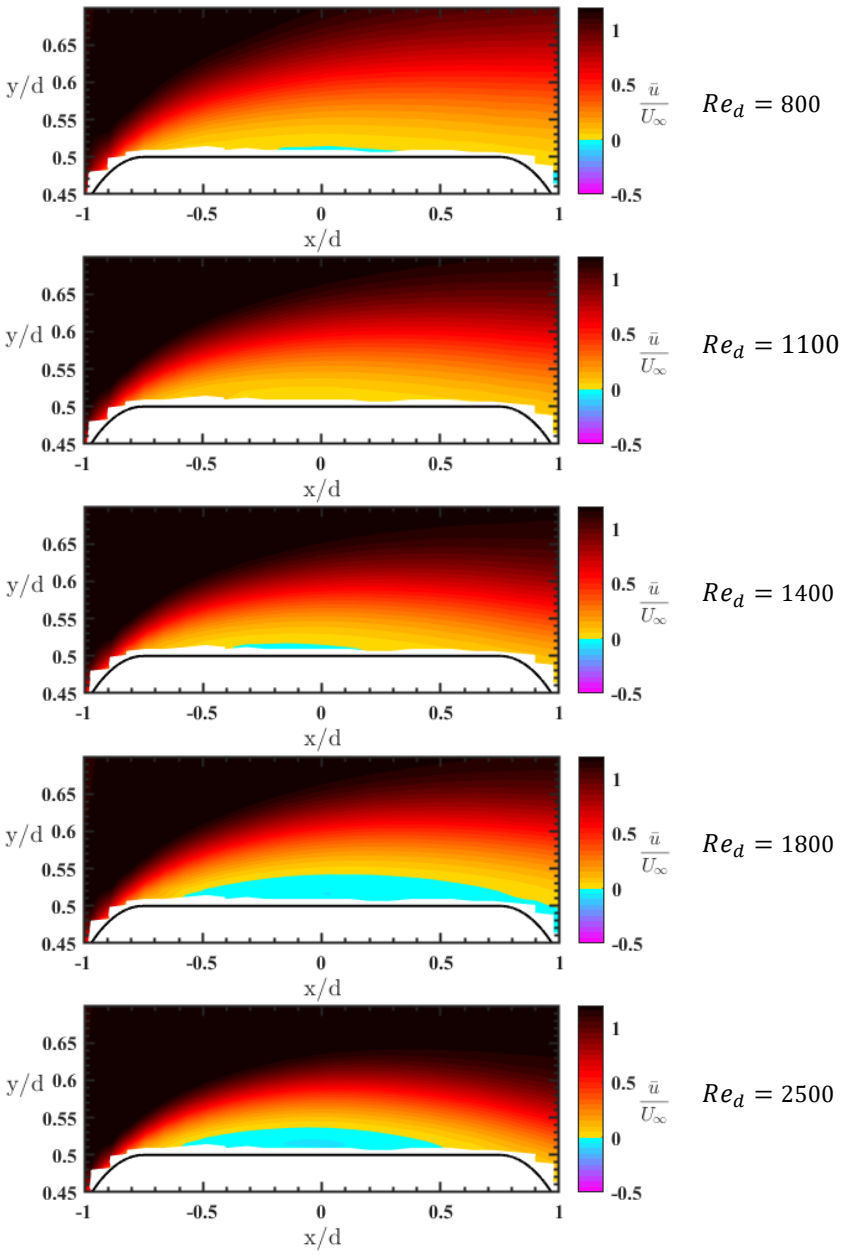

Figure 10. Smooth cylinder. Magnified view of the mean velocity color contour maps normalized by the freestream velocity U_∞. The vertical scale is stretched, distorting the view, to make the separation zone visible. Rows show different Reynolds numbers. Flow is from left to right.

As seen in Figure 9 (right), the boundary layer at $Re_d = 800 - 1400$ remains largely quiet with relatively low unsteadiness, with the maximum fluctuations being lower than 5% of the freestream velocity. Better details of the fluctuating velocity development in the streamwise direction may be observed in Figure 11. In this figure, the maximum rms velocity value across each profile is

extracted and plotted versus x/d at each Reynolds number. Figure 11 shows that fluctuations grow downstream for all Reynolds numbers. Excluding the regrowth of the fluctuation seen downstream of $x/d \approx 0.6$ at $Re_d = 2500$, the unsteadiness level at $Re_d = 1800$ is the highest in the shear layer with a faster growth rate with the downstream distance than all other cases. This coincides with the fact that an open separation is observed at this Reynolds number only. Figure 11 also shows that at $Re_d = 800 - 1800$, the $r_{rms,p}/U_\infty$ growth is monotonic. At $Re_d = 2500$, the maximum u_{rms} values reach a peak ("saturate") before a second growth stage develops downstream of saturation. The separated shear layer reattaches to the surface at this Reynolds number, and the first peak of the maximum u_{rms} values occurs slightly before the reattachment point. The second stage of growth is downstream of reattachment, where the shear layer from the reattached flow starts developing.

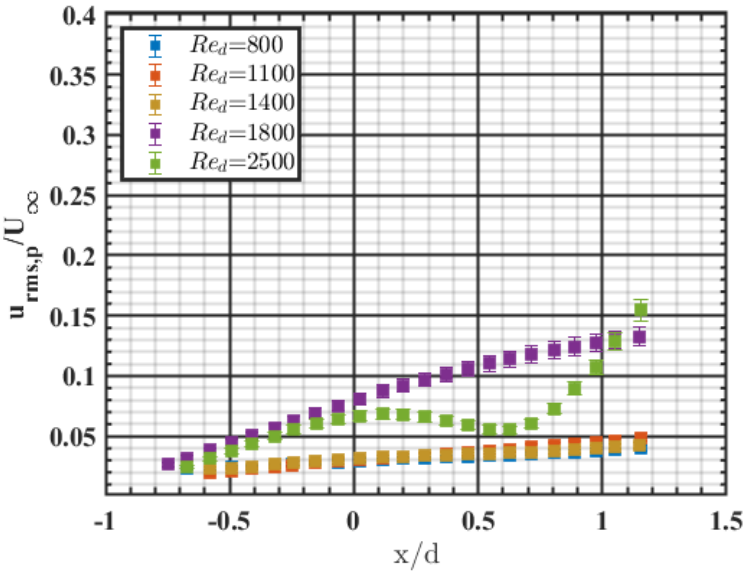

Figure 11. Comparison between maximum u_{rms}/U_∞ development along the surface of the smooth cylinder at different Reynolds numbers.

A similar analysis to the above is done for the 2Dp cylinder with $\varepsilon/d = 5\%$ using the results given in Figure 12. The effect of this geometry on promoting flow separation is evident. The flow separates downstream of the topology peak at the front corner with the separation point

predominantly insensitive to Reynolds number. The separation bubble remains open, and it probably reattaches only at the highest Reynolds number studied, $Re_d = 2500$. This trend with Reynolds number is expected, but given the current data resolution, the reattachment found at the highest Reynolds number is not certain. To be clear, Figure 13 displays a magnified view of the near-wall velocity profiles in the vicinity of the reattachment location. As seen from the figure, while a zero crossing is not observed in the velocity profile across the tagging line at x/d=0.96, the data point closest to the wall is about 5 pixels away from the surface, leaving a possibility of a zero-crossing closer to the wall. In either case, the separation zone boundary travels very close to the surface over the topology peak at the aft corner of the 2Dp cylinder at $Re_d = 2500$. Also noteworthy is that the inside of the topology valleys is filled with a "dead" cushion of fluid with very weak negative velocity, irrespective of the Reynolds number and separation bubble thickness.

Considering u_{rms}/U_∞ data, the separated shear layer at $Re_d = 1100$ shows a higher level of fluctuations compared to the lower and higher adjacent Reynolds numbers (Figure 12, right). Further increase of the Reynolds number to $Re_d = 1800$ exhibits widening over a short streamwise fetch of the region carrying high velocity fluctuations at around $x/d = 0.4$. Also, the highest level of fluctuations is observed at this Reynolds number. This widening of the high rms zone can be related to vortex formation from the shear layer roll-up, as will be seen from flow visualization results in Chapter 5 (Figure 65). Increasing the Reynolds number to $Re_d = 2500$ pushes the widening of the high rms region towards the upstream direction, and also brings this region closer to the surface. Therefore, it seems for this geometry at $Re_d = 1800$ and 2500, the separated shear layer rolls up and vortical structures start developing above the model surface. This vortex formation, and moving closer to the surface at $Re_d = 2500$, is associated with the *probable* closure of the separation bubble noted from the mean velocity data.

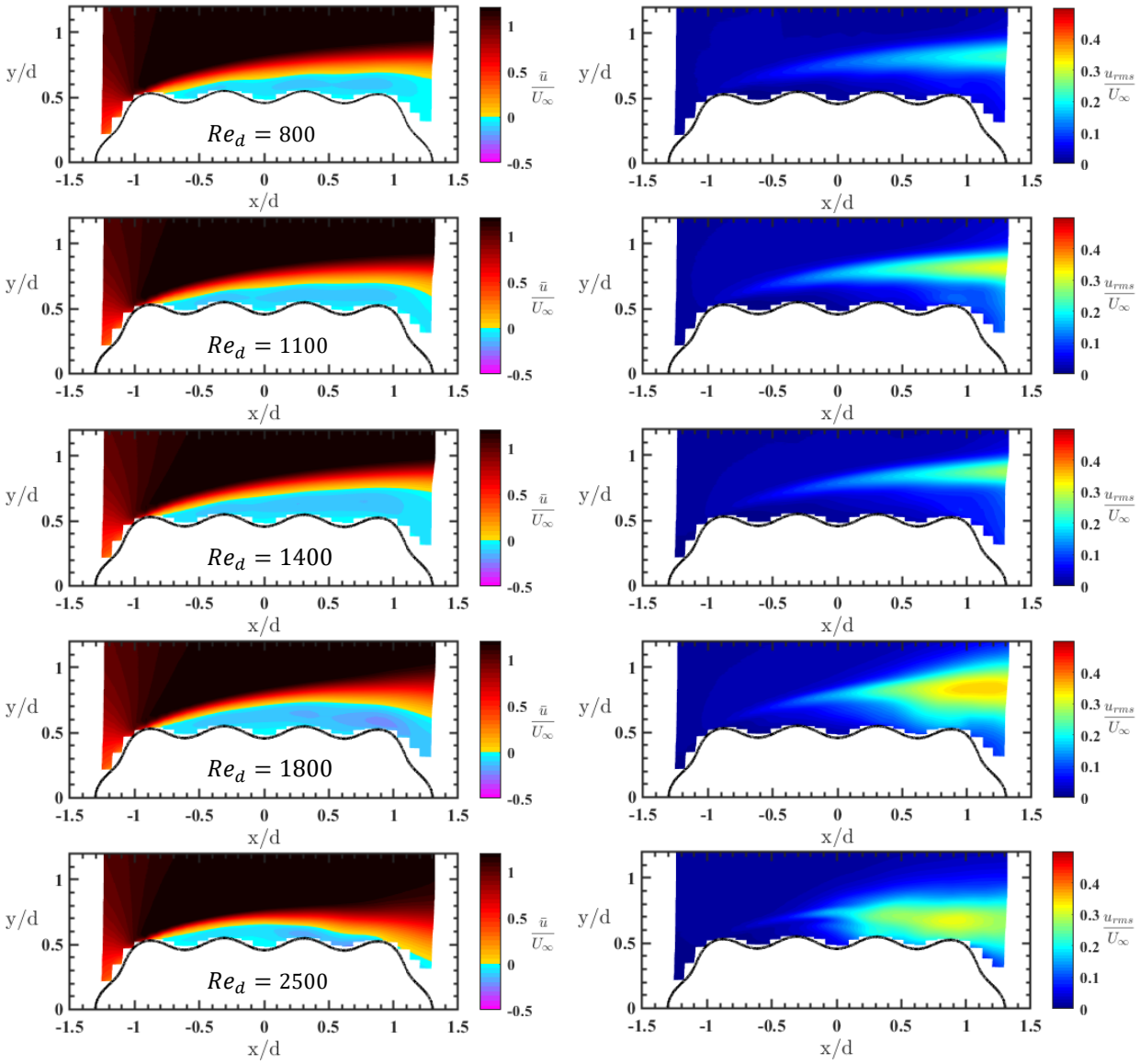

Figure 12. 2Dp-5% cylinder. Mean (left) and rms (right) velocity color contour maps normalized by the freestream velocity U_∞. Rows show different Reynolds numbers. Flow is from left to right.

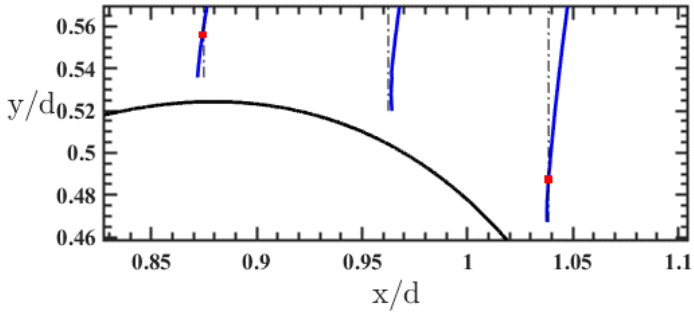

Figure 13. Magnified view of the Mean velocity profiles over the topology peak at the aft corner of the 2Dp cylinder at $Re_d = 2500$. Red points mark the zero-crossing of the velocity profile.

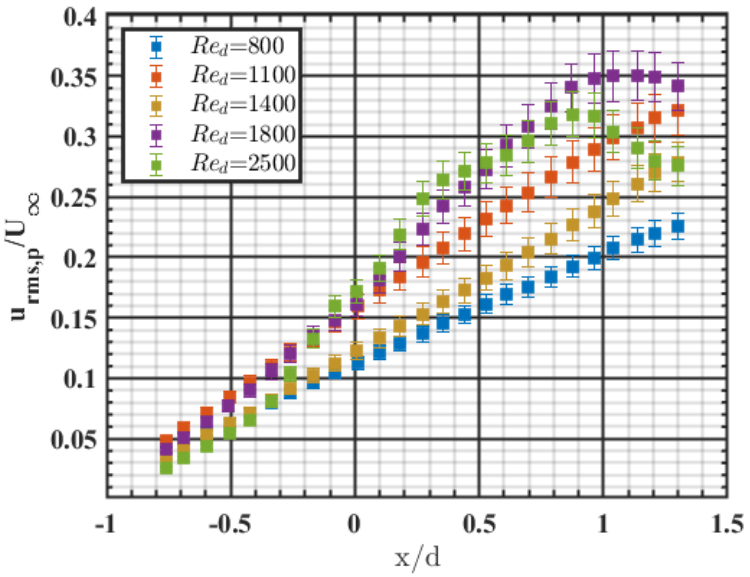

Figure 14. Comparison between maximum u_{rms}/U_∞ development along the surface of the 2Dp cylinder at different Reynolds numbers.

The maximum rms velocity value across each profile over the surface of the 2Dp cylinder is Examined in Figure 14. At $Re_d = 800 - 1400$ the maximum u_{rms} values increase monotonically with the downstream. This monotonic trend is disturbed at higher Reynolds numbers, when vortex formation from roll-up of the shear layer is observed (see Figure 65 in Chapter 5), and the fluctuation intensity reaches a peak. At $Re_d = 2500$, the peak in the maximum u_{rms} values is observed at $x/d = 0.9$, right before the point of possible reattachment. A decaying trend follows afterward, reinforcing the expectation that the flow does reattach to the surface. It is observed in previous studies that the maximum fluctuations in the shear layer over airfoils, back-step geometries, and bluff bodies plateau in the vicinity of the reattachment point and decay farther downstream; for example, see references [18-20].

The separation zone boundary for the 2Dp cylinder geometry at different Reynolds numbers is depicted in Figure 15. This boundary is obtained by identifying the zero-crossing location of each mean velocity profile at a given x location to delineate the border surrounding the reverse-flow region. A second-order polynomial fit is applied to these locations to capture the

shape of the separation zone boundary. This polynomial fits the data points very well for most cases. However, a second-order polynomial cannot fully follow a complex boundary with, for example, both concave and convex curvatures, such as seen at $Re_d = 2500$ (see the transition between orange and light blue colors between $x/d \approx 0.25$ and 1 in Figure 12 at this Reynolds number). Higher orders (up to sixth-order) polynomials are tested for this case, but did not show a considerable improvement over the second-order fit. Nonetheless, the second-order polynomial is sufficient to represent the separation zone boundary and therefore is used for the purpose of this study, unless otherwise noted.

The separation zone boundary for the 2Dp cylinder, shown in Figure 15, supports the earlier observation that at $Re_d = 2500$ the flow reattaches to the surface just upstream of the trailing edge. It also shows that the separation zone boundary is flatter and located farther from the surface at $Re_d = 1400$ compared to $Re_d = 1100$ and 1800, which shows a non-monotonic behavior. Figure 15 also shows more clearly that the separation point (the upstream end of the separation zone boundary) is similar for all Reynolds numbers.

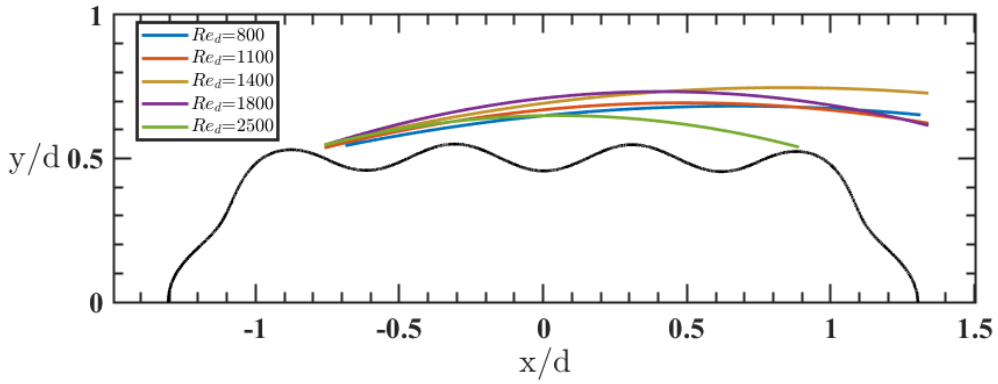

Figure 15. Comparison of the mean separation zone boundary for the 2Dp cylinder at different Reynolds numbers. Flow is from left to right.

Similar to the 2Dp geometry, flow over the 2Dv cylinder, shown in Figure 16, separates right downstream of a topology peak. However, separation occurs farther downstream compared to the 2Dp case, and the separated flow remains much closer to the geometry surface such that as

it passes over the next topology bump, it almost reattaches to the surface. At $Re_d = 800 - 1400$, the flow reattaches to the surface upstream of a topology bump at $x/d \approx 0.55$. Interestingly, this geometry shows low sensitivity to Reynolds numbers in the range of $Re_d = 800 - 1400$ in terms of the separation/reattachment behavior of the boundary layer. Increasing the Reynolds number further to $Re_d = 1800$ is associated with the opening up of the separation bubble, which thickens even further as the Reynolds number rises to $Re_d = 2500$. This is opposite to the 2Dp geometry behavior, but the smooth cylinder also developed an open separation bubble at $Re_d = 1800$. It is speculated that further increase in the Reynolds number would cause the separated flow to reattach to the 2Dv cylinder surface, similar to the other geometries. This can be a point of interest in future studies.

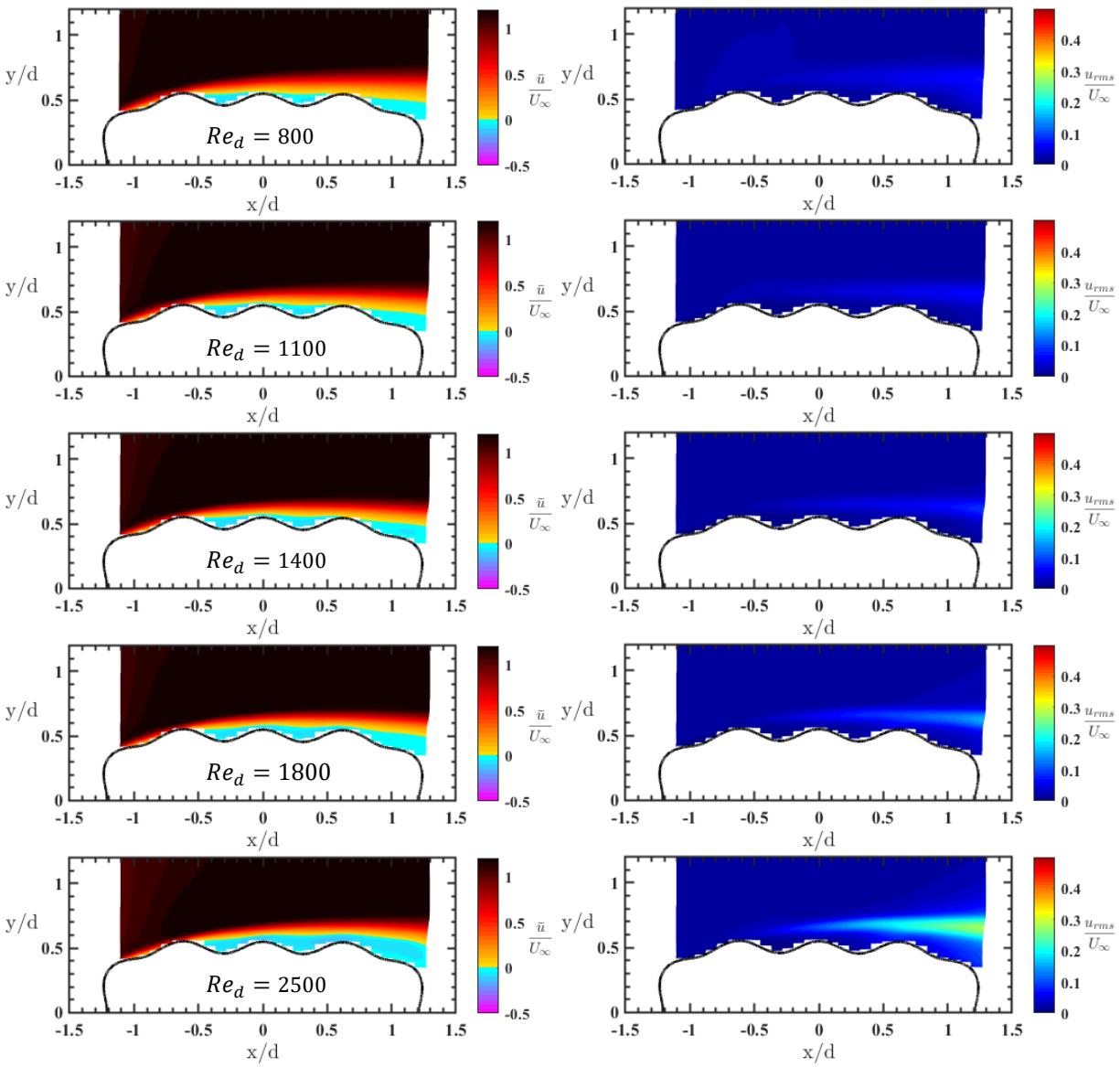

Figure 16. 2Dv-5% cylinder. Mean (left) and rms (right) velocity color contour maps normalized by the freestream velocity U_∞. Rows show different Reynolds numbers. Flow is from left to right.

Figure 17 shows the mean separation zone boundary for the 2Dv cylinder. It can be noted that, similar to the 2Dp case, the separation point is similar over the studied range of Reynolds numbers. It is also evident how the separation zone boundary grows in lateral thickness at higher Reynolds numbers. However, the variation caused by the Reynolds number change is much more limited compared to the 2Dp geometry.

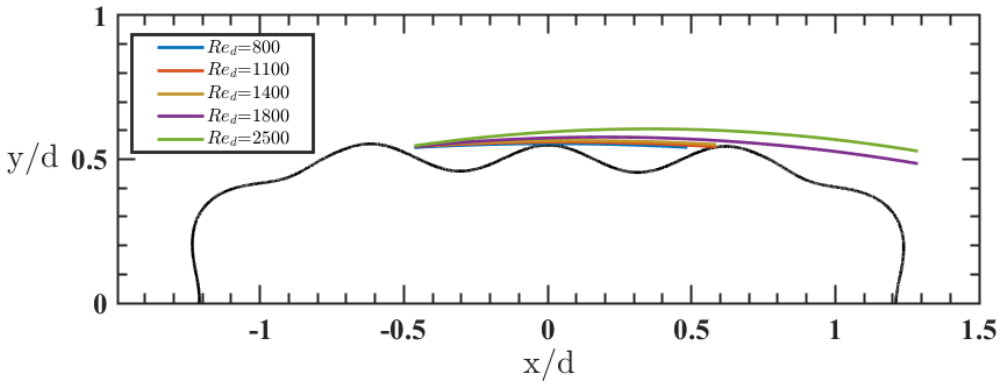

Figure 17. Comparison of the mean separation zone boundary for the 2Dv cylinder at different Reynolds numbers. Flow is from left to right.

Analysis of the maximum u_{rms} velocity for the 2Dv cylinder in Figure 18 shows that the fluctuation level in the shear layer increases monotonically with the downstream at all Reynolds numbers. The rate of this increase (i.e. the slope of the line), however, starts growing at $Re_d = 1800$ as the separation bubble opens up and the separation zone boundary starts thickening. The highest fluctuation level is observed at $Re_d = 2500$ which shows the thickest separation zone boundary.

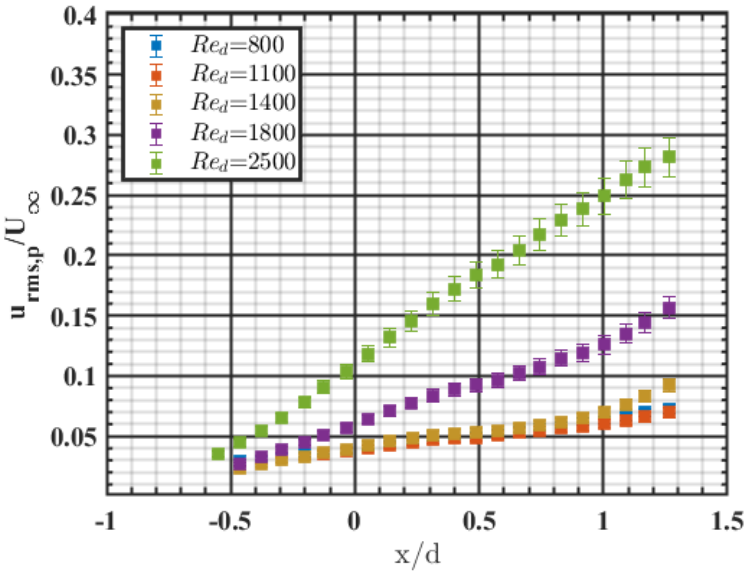

Figure 18. Comparison between maximum u_{rms}/U_∞ development along the surface of the 2Dv cylinder at different Reynolds numbers.

Overall, for the 2Dv cylinder, it appears that the separated flow merely fills the topology valleys and the effective body shape becomes close to that of the smooth cylinder. Depicted in

Figure 19, the maximum u_{rms} values in the shear layer for the 2Dv cylinder are also very close to those from the smooth cylinder at $Re_d = 800 - 1800$, which suggests that the presence of a 2D topology with a valley at the leading edge does not alter the flow substantially from that over the baseline smooth geometry, especially when compared to the effect of the 2Dp geometry. It is at $Re_d = 2500$ where the u_{rms} values deviate between the smooth and 2Dv cylinders, when the flow reattaches to the surface of the smooth cylinder but remains separated over the 2Dv cylinder's surface. Moreover, the fluctuations are lower in the shear layer of the 2Dv cylinder than the 2Dp cylinder at all Reynolds numbers. This is consistent with the earlier observation that, excluding the 2Dp cylinder at $Re_d = 2500$, the maximum $u_{rms,p}$ level shows a direct relation with the thickness of the separation zone boundary. Figure 21 also shows that the fluctuations in the shear layer are amplified by the presence of the topology with a peak at the LE, compared to the baseline geometry.

The domain of the shear layer containing the high rms fluctuations is highlighted for the smooth, 2Dp, and 2Dv cases in Figure 20. The loci of the maximum rms velocity are marked by circle markers, and the highlighted domain surrounds the rms fluctuations higher than 50% of the value of the $u_{rms,p}$ at each streamwise location. The color codes remain consistent with the plots shown so far, where the black, red, and green points and shaded regions are allotted to the smooth, 2Dp, and 2Dv cases, respectively.

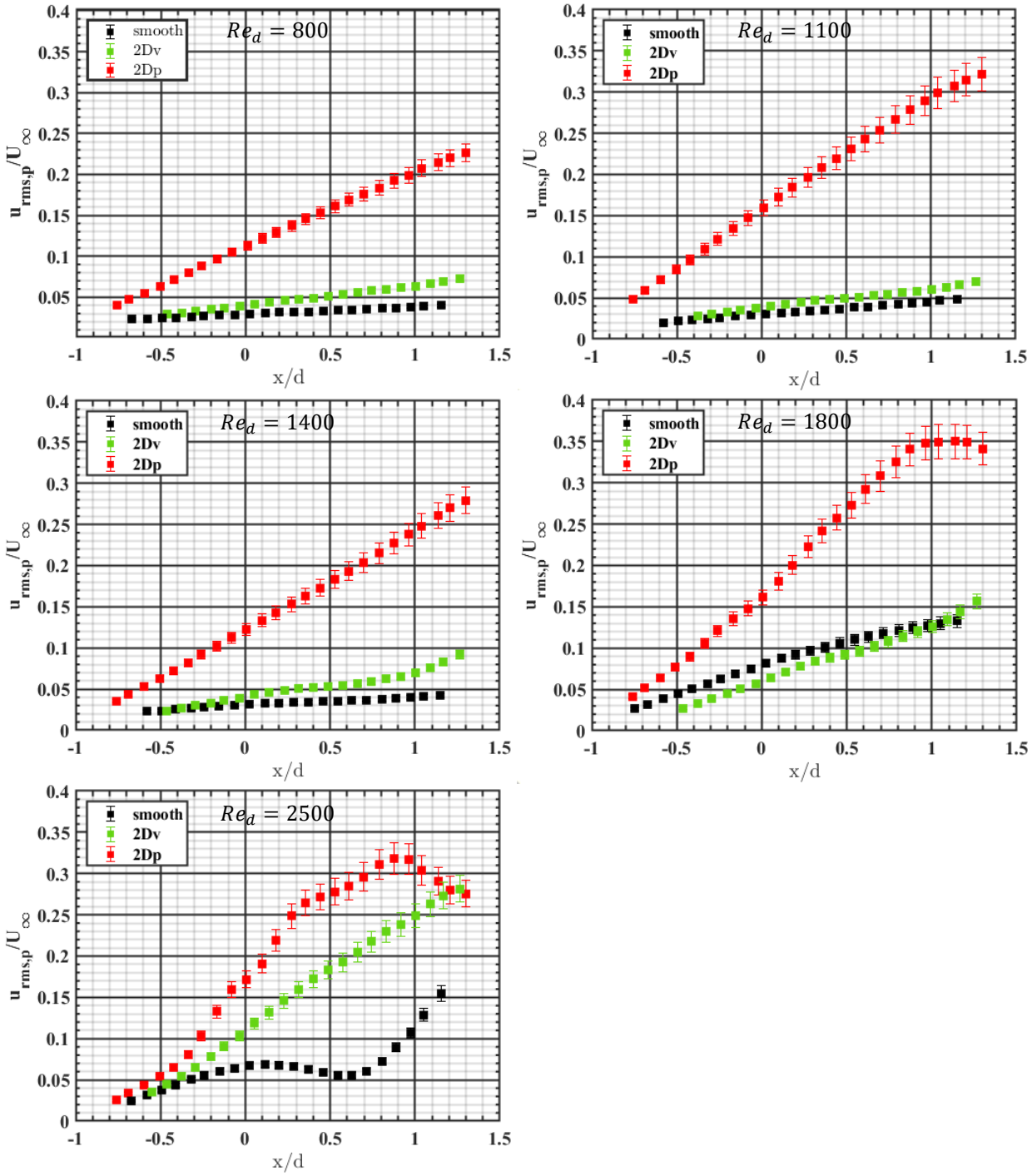

Figure 19. Comparison between maximum u_{rms}/U_∞ development along the surface of the smooth (black), 2Dp (red), and 2Dv (green) cylinders, at different Reynolds numbers.

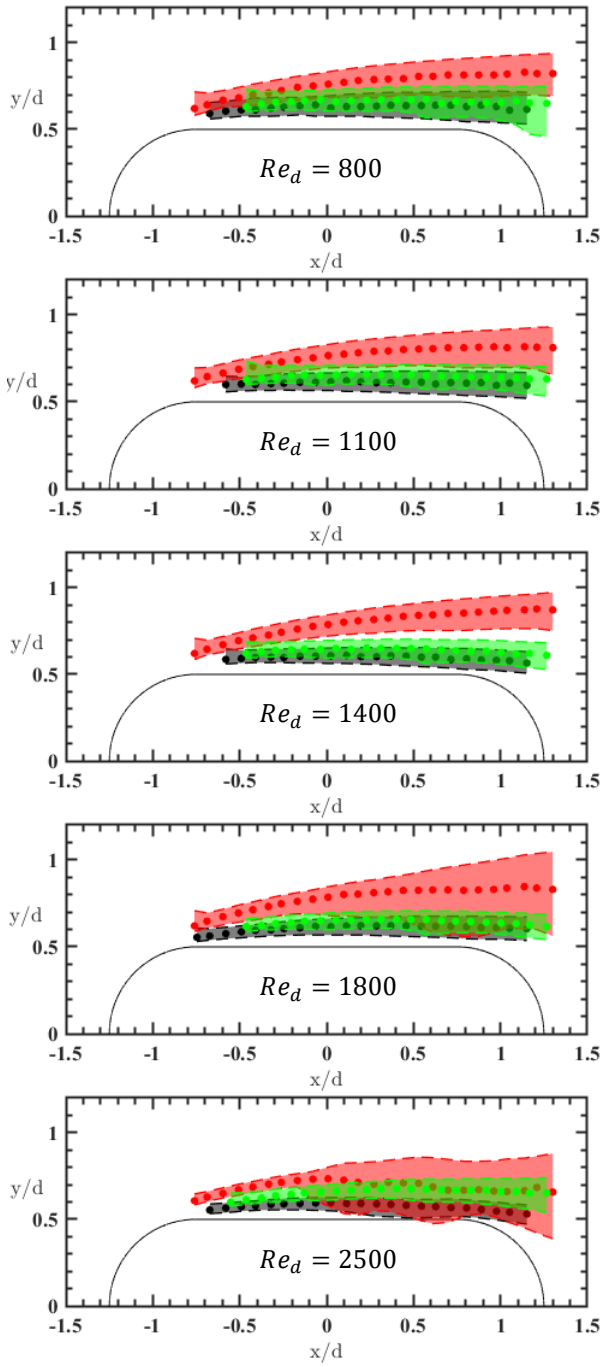

Figure 20. Domain of high rms velocity fluctuations, covering the region with rms velocity higher than 50% of the maximum rms velocity at each x/d location. Results for the smooth, 2Dp, and 2Dv cases shown in black, red, and green respectively. Only the cross-section of the baseline geometry is shown for simplicity. Flow is from left to right.

This domain is thickest for the 2Dp geometry at all Reynolds numbers, but remains comparable between the smooth and the 2Dv cases. In addition, for the two cases of the 2Dp cylinder at $Re_d = 1800$ and 2500, vortex formation from shear layer roll-up is observed on top

of the cylinder surface which is associated with the rapid widening of the high rms domain (see Figure 65 in Chapter 5).

3.2 Effect of the Surface Topology Amplitude

Mean and rms velocity color contour maps for the 2Dp cylinder with lower ($\varepsilon/d = 2.5\%$) and higher ($\varepsilon/d = 10\%$) topology amplitudes compared to the cases considered so far are shown in Figure 21 and Figure 22, respectively, to examine the effect of the topology amplitude. From Figure 21 it can be seen that, similar to the 5% topology amplitude, the presence of a topology peak at the upstream corner of the cylinder causes an early separation of the flow, downstream of a topology peak at $x/d \approx -0.78$, even at such small topology amplitude. In addition to this similarity with the 2Dp-5% results, previously shown in Figure 12, the separation bubble remains open up to $Re_d = 1800$, and becomes very close to reattachment at $Re_d = 2500$. However, as before, reattachment cannot be ascertained with the current data resolution. Non-monotonic behavior in the separation zone boundary with Reynolds number is also seen for this case, where first, increasing Reynolds number to $Re_d = 1100$ makes the separation bubble thinner, but further increase up to $Re_d = 1800$ is associated with thickening of the separation bubble.

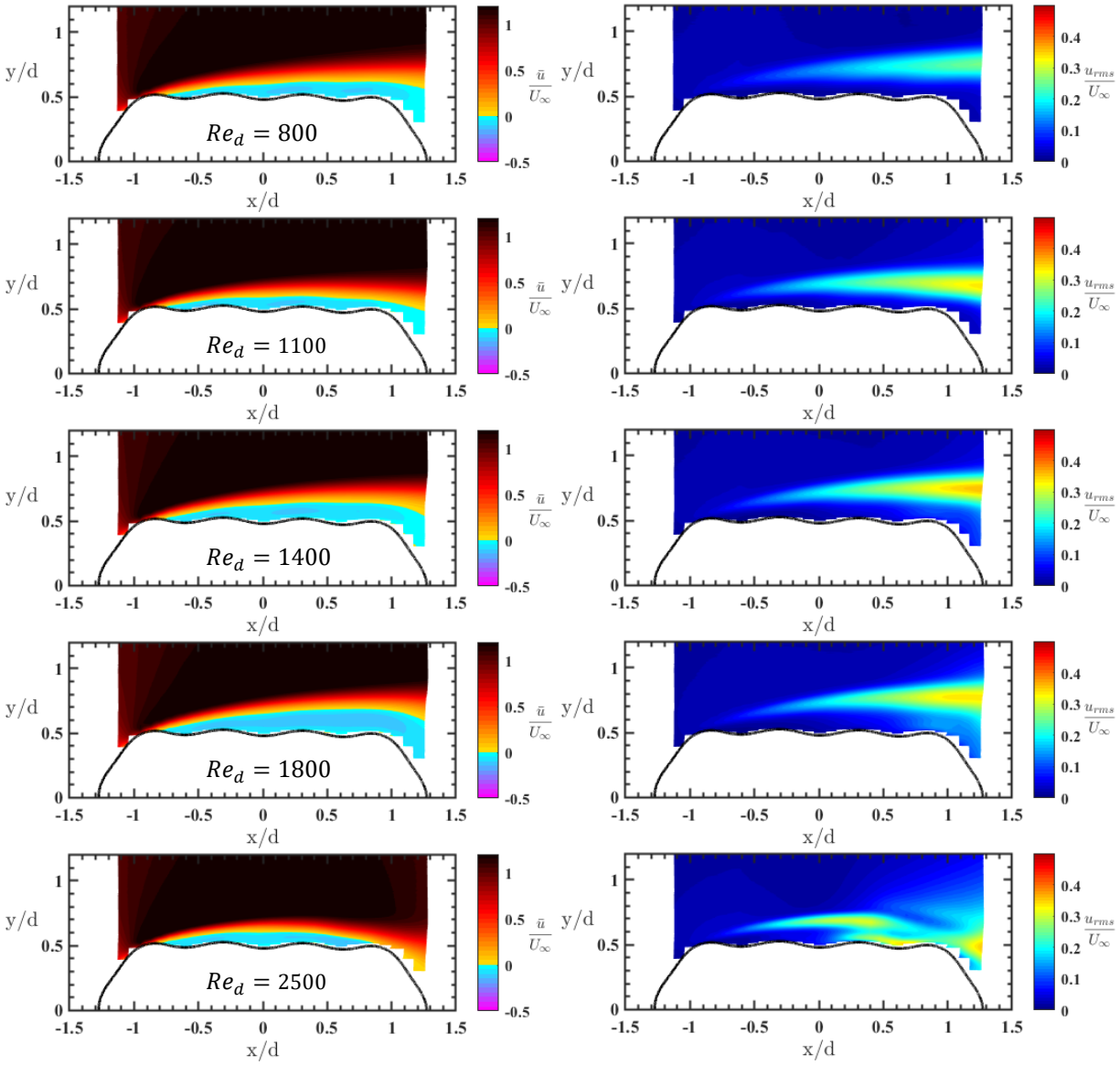

Figure 21. 2Dp-2.5% cylinder. Mean (left) and rms (right) velocity color contour maps normalized by the freestream velocity U_∞. Rows show different Reynolds numbers. Flow is from left to right.

At the Reynolds number range $Re_d = 800 - 1800$, where open separation is observed, shear layer unsteadiness grows in strength downstream, similar to the case of 2Dp-5%. However, for the current case, the rapid expansion of the high unsteadiness region, which is found to be coincident with the shear layer roll-up, is not seen at $Re_d = 1800$ and is delayed to the higher Reynolds number of 2500. The shear layer is seen to roll up to form vortical structures at $Re_d =$

2500, which is believed to be the reason for the separation bubble approaching the surface and the possibly reattaching.

For the higher amplitude of $\varepsilon/d = 10\%$, shown in Figure 22, $Re = 2500$ remains the turning point for boundary layer separation/reattachment. As before for the same 2Dp geometry, below this Reynolds number, the separation bubble remains open.

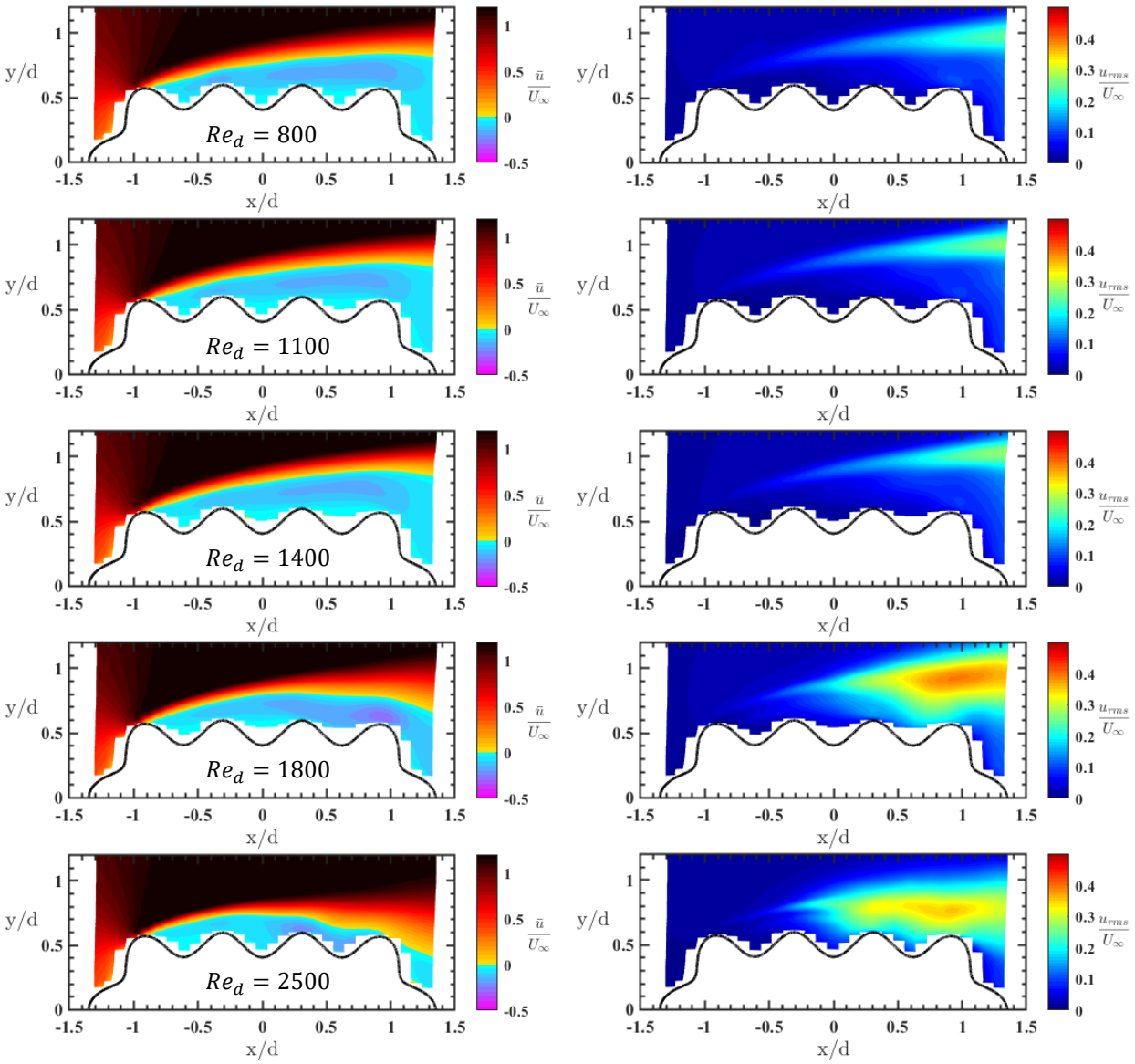

Figure 22. 2Dp-10% cylinder. Mean (left) and rms (right) velocity color contour maps normalized by the freestream velocity U_∞. Rows show different Reynolds numbers. Flow is from left to right.

Similar to the other amplitudes of the 2Dp geometry, for the 10% amplitude, there $might$ be a late reattachment of the boundary layer at $Re_d = 2500$ that cannot be ascertained with the given resolution of the current data. The separation also occurs downstream of the topology peak at the front corner of the cylinder, with the separation point showing negligible sensitivity to Reynolds number. The separation bubble's size does not vary significantly at $Re_d = 800 - 1400$, but starts thinning down at higher Reynolds numbers. Unsteadiness in the shear layer grows with downstream distance at $Re_d = 800 - 1400$ in the same manner, as other 2Dp geometries, before the signature of the vortex roll-up in widening the high u_{rms} zone starts emerging at $Re_d = 1800$ and develop further at $Re_d = 2500$.

The maximum rms velocity evolution in the streamwise direction is compared for all the 2Dp geometries in Figure 23. In $Re_d = 800 - 1400$ range, the maximum rms velocity increases monotonically for all 2Dp geometries. The results for the 5% and 10% amplitude cases match within the error bars at $Re_d = 800$ and 1400. The 2.5% amplitude case shows the highest u_{rms} peak values in this Reynolds number range, with the difference compared to the other 2Dp cases becoming more significant as the Reynolds number increases. The results for all 2Dp cases are very close up to the mid-chord of the cylinders at $Re_d = 1800$, but farther downstream and at $0 < x/d < 1$, the 10% amplitude case shows higher values than the other two cases. Downstream of $x/d = 1$, the results for all 2Dp cases plateau, which coincides with the rapid widening of the domain of high velocity fluctuations for the 5% and 10% amplitude cases. However, such rapid widening of the high velocity fluctuations domain is interestingly not seen for the 2.5% amplitude case at this Reynolds number. At $Re_d = 2500$, the results for all 2Dp cases plateau over the surface and decrease with further increase in x/d, which happens earlier for the 2.5% amplitude case compared to the other 2Dp cylinders. Rapid widening of the high velocity fluctuations domain is

seen and shear layer reattachment is expected for all 2Dp cylinders at this Reynolds number. It should be noted that the results for the 2.5% amplitude case are truncated at $x/d = 0.75$, since the $u_{rms,p}$ results are extracted at the location of the first rms velocity peak developing over the surface. At this streamwise location, the peaks do not exist over the trajectory of the first rms velocity peak anymore, and the rms velocity peak starting to develop near the surface at $x/d \approx 0.2$ becomes the only prominent peak in the rms velocity profiles.

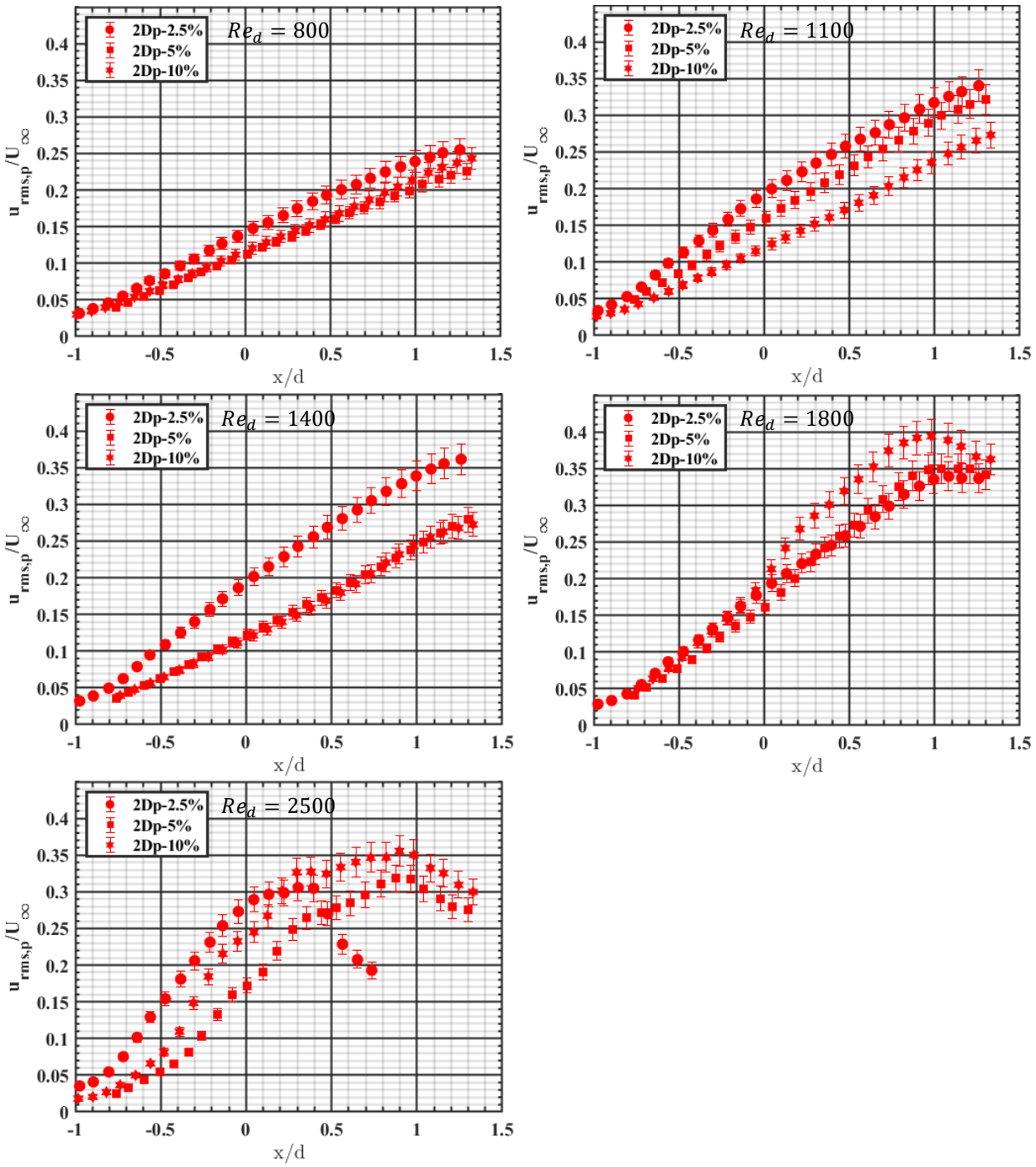

Figure 23. Comparison between maximum u_{rms}/U_∞ values along the surface of cylinders with 2Dp geometry and different topology amplitudes at different Reynolds numbers.

The effect of topology amplitude on the flow over the 2Dv geometry is analyzed in Figure 24 and Figure 26. In Figure 24, mean and rms velocity color contour maps are shown for the 2Dv-2.5% case. This geometry shows the least sensitivity to Reynolds number among the other studied

geometries. There are two isolated closed separation bubbles in the valleys of the topology at $Re_d = 800 - 1400$. At higher Reynolds numbers, these two bubbles connect to form a single separation bubble. These details can be better seen in Figure 25, where a magnified view of the mean velocity profiles over the valleys on the surface of this cylinder are shown and the points of zero-crossing velocity are marked. Nevertheless, the flow separation does not considerably affect the overall flow over the surface, and the separation bubbles act only as a "cushion" to fill the topology dips. The minimal effect of this geometry on the flow is further seen by monitoring the small unsteadiness levels in the shear layer throughout the studied range of Reynolds numbers. Moreover, the shear layer remains very close to the surface.

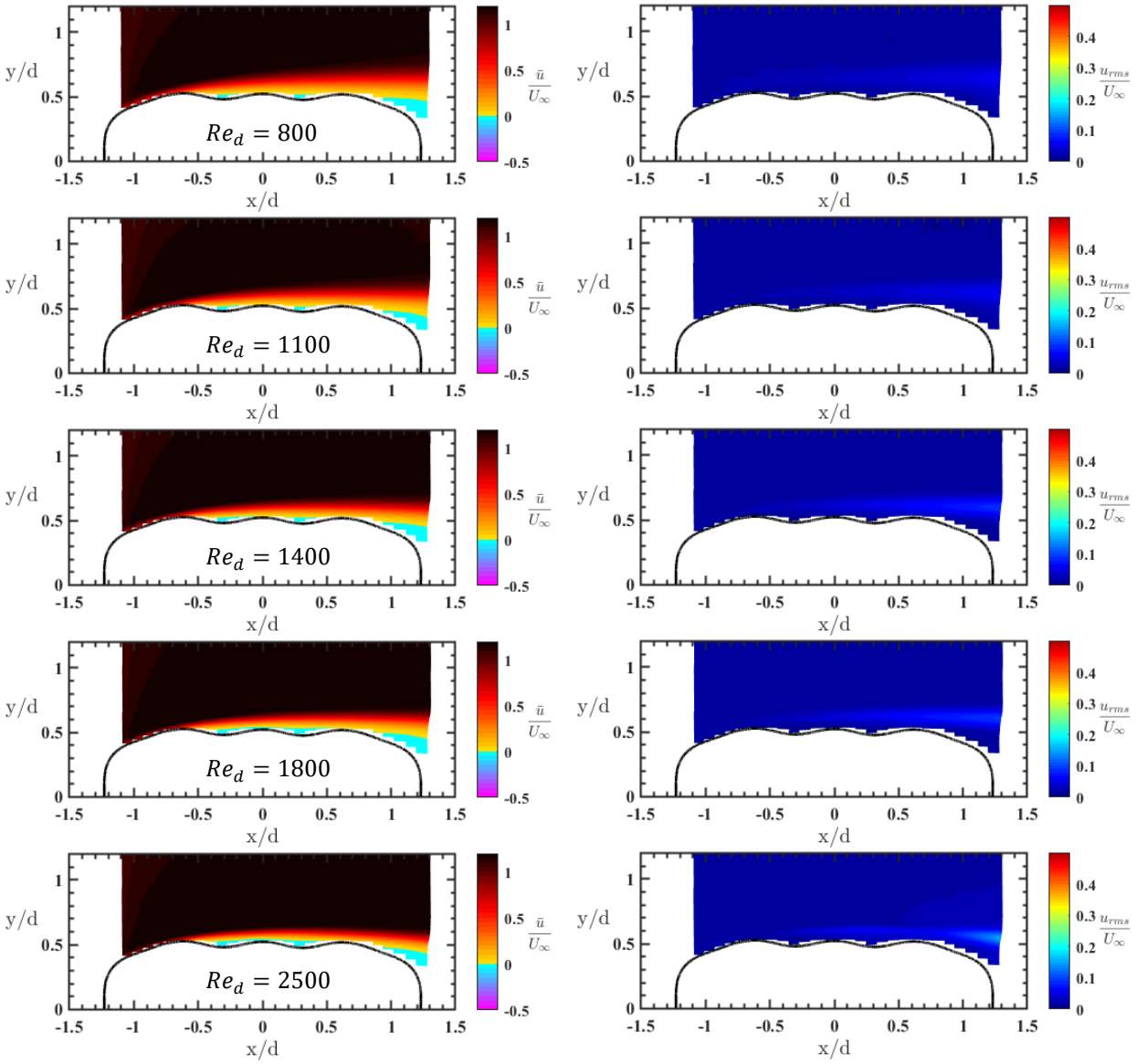

Figure 24. 2Dv-2.5% cylinder. Mean (left) and rms (right) velocity color contour maps normalized by the freestream velocity U_∞. Rows show different Reynolds numbers. Flow is from left to right.

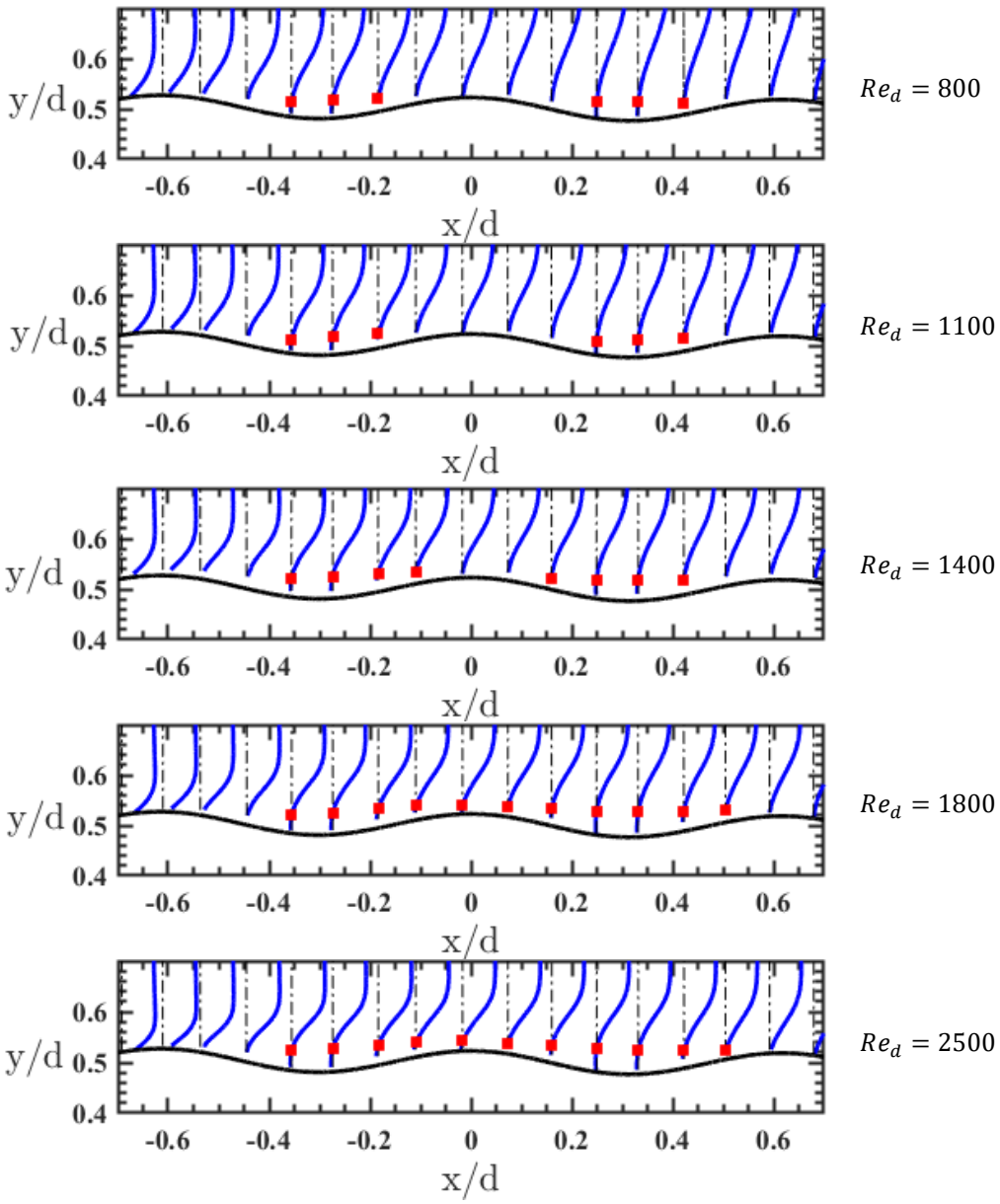

Figure 25. Magnified view of the Mean velocity profiles over the valleys on the surface of the 2Dv cylinder at different Reynolds numbers. Red points mark the zero-crossing of the velocity profile.

The case with a higher amplitude of $\varepsilon/d = 10\%$ is displayed in Figure 26. This is the only case where changing the topology amplitude is seen to affect the separation point. Here, separation occurs earlier than the 2Dv cylinders with 2.5% and 5% topology amplitudes, right downstream of the topology peak at the front corner. Nonetheless, flow reattaches quickly, and the closed separation bubble remains local within the first valley before the flow separates again downstream

of the next topology peak. The latter separation point is comparable to that seen for the other amplitudes. Another effect of this higher topology amplitude is that, downstream of the second separation point, the flow remains separated over the remainder of the surface at all Reynolds numbers.

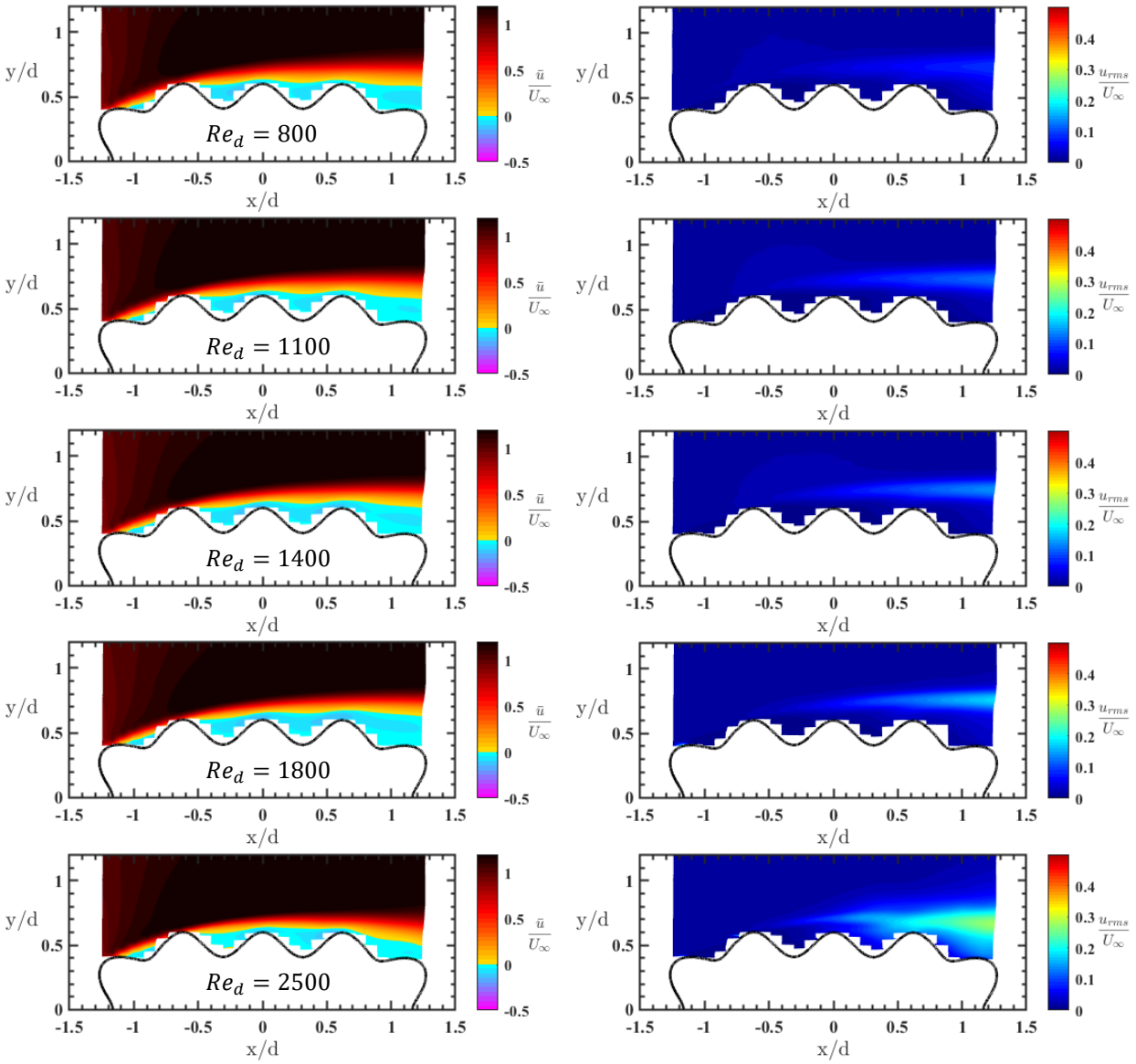

Figure 26. 2Dv-10% cylinder. Mean (left) and rms (right) velocity color contour maps normalized by the freestream velocity U_∞. Rows show different Reynolds numbers. Flow is from left to right.

From the rms velocity color contour maps in the right column of Figure 26, it can be seen that the unsteadiness grows in the shear layer with the downstream and Reynolds number. A rapid

widening of the high rms region is not observed for any 2Dv case at any Reynolds number, suggesting that the shear layer roll-up does not occur above the cylinder surface for this geometry in the studied range of Reynolds numbers. This observation correlates with the shear layer being very close to the surface.

The maximum rms velocity at each streamwise location is extracted and compared for all the 2Dv geometries in addition to the smooth cylinder in Figure 27. The first streamwise location for this analysis is where a noticeable peak in the rms velocity profile is observed due to the shear layer development. In the Reynolds number range of $Re_d = 800 - 1800$, the growth in the maximum rms velocity is monotonic. The 2.5% amplitude at $Re_d = 2500$ is the only case where the rms values reach a peak at around $x/d = 0.25$ before increasing again farther downstream. Overall, the lowest and highest topology amplitudes exhibit the lowest and the highest levels of shear layer velocity fluctuations, respectively. The 5% topology shows a close behavior to that of the 2.5% geometry in the range of $Re_d = 800 - 1400$. In this Reynolds number range, both of these cylinders show a closed separation bubble on the cylinders' surface. At $Re_d = 1800$, reattachment does not occur for the 5% geometry anymore, which is similar to the case of 10% but opposite to the geometry with 2.5% amplitude. This is associated with a deviation in the level of fluctuations in the shear layer of the 5% geometry from that of the 2.5% geometry and shifts the 5% amplitude results towards the level of fluctuations seen in the 10% geometry, and they eventually collapse at $Re_d = 2500$. At the Reynolds number range $Re_d = 800 - 1400$ the values seem to approach those from the smooth cylinder with decreasing the topology amplitude. The smooth cylinder shows comparable $u_{rms,p}$ values to those from the 2Dv cylinders with 5% and 10% amplitude at $Re_d = 1800$, but higher compared to the 2Dv-2.5% case. It was observed that the former cases show an open separation, whereas the latter case shows a thin closed separation

bubble over the surface. At $Re_d = 2500$, the results are very close for the smooth and the 2Dv-2.5% cylinder, especially in that both show a non-monotonic behavior. These two cases, unlike the 2Dv-5% and 10% cases, show a closed separation bubble over the surface.

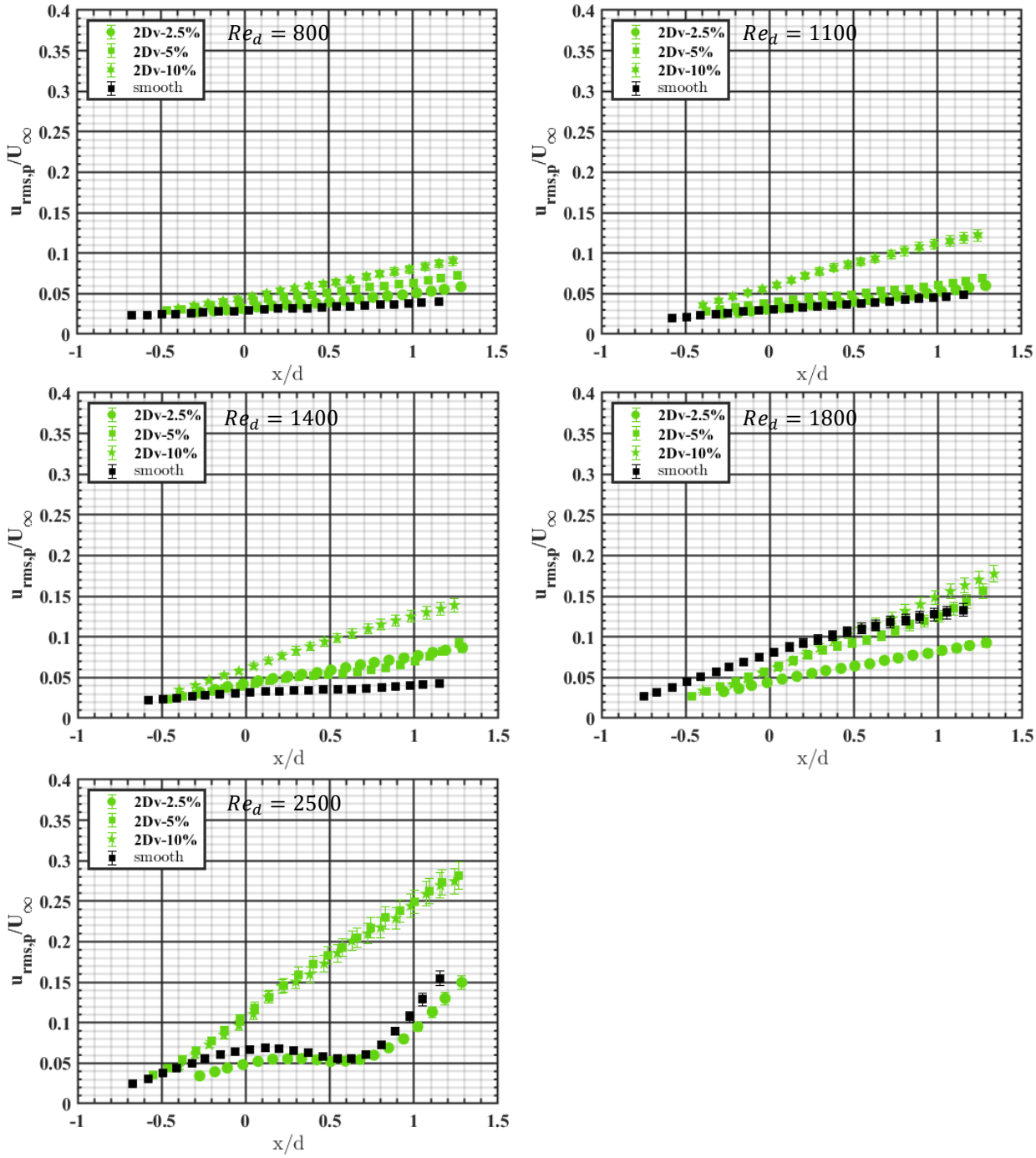

Figure 27. Comparison between maximum u_{rms}/U_∞ values along the surface of cylinders with 2Dv geometry and different topology amplitudes at different Reynolds numbers. Results are also compared against the smooth cylinder.

3.3 Effect of Surface Topology Variation Along the Span

The effect of adding surface topology variation along the span on the velocity field over the cross-sectional geometries with a peak at the leading edge is examined using Figure 28. From the mean velocity color contour maps in the left column of this figure, it can be seen that the presence of three-dimensionality of the topology significantly alters the separation/reattachment behavior relative to the flow over the surface of the cylinders with 2Dp cross-sectional geometry. Overall, the separation bubble remains very thin for the 3Dp case and predominantly fills the valleys of the topology over the surface; although the bubble gains lateral thickness with increasing the Reynolds number.

Further information regarding the mean boundary layer behavior may be extracted by characterizing the separation zone, as done in Figure 29. This helps estimate the separation and the reattachment location and characterize the overall shape of the separation zone. Figure 29 compares results from the 2Dp and 3Dp configurations. The separation point for the 3Dp case remains the same as that observed for the 2Dp cylinder. More specifically, the flow separates after the leading edge, downstream of a surface topology peak at the front corner of the cylinder.

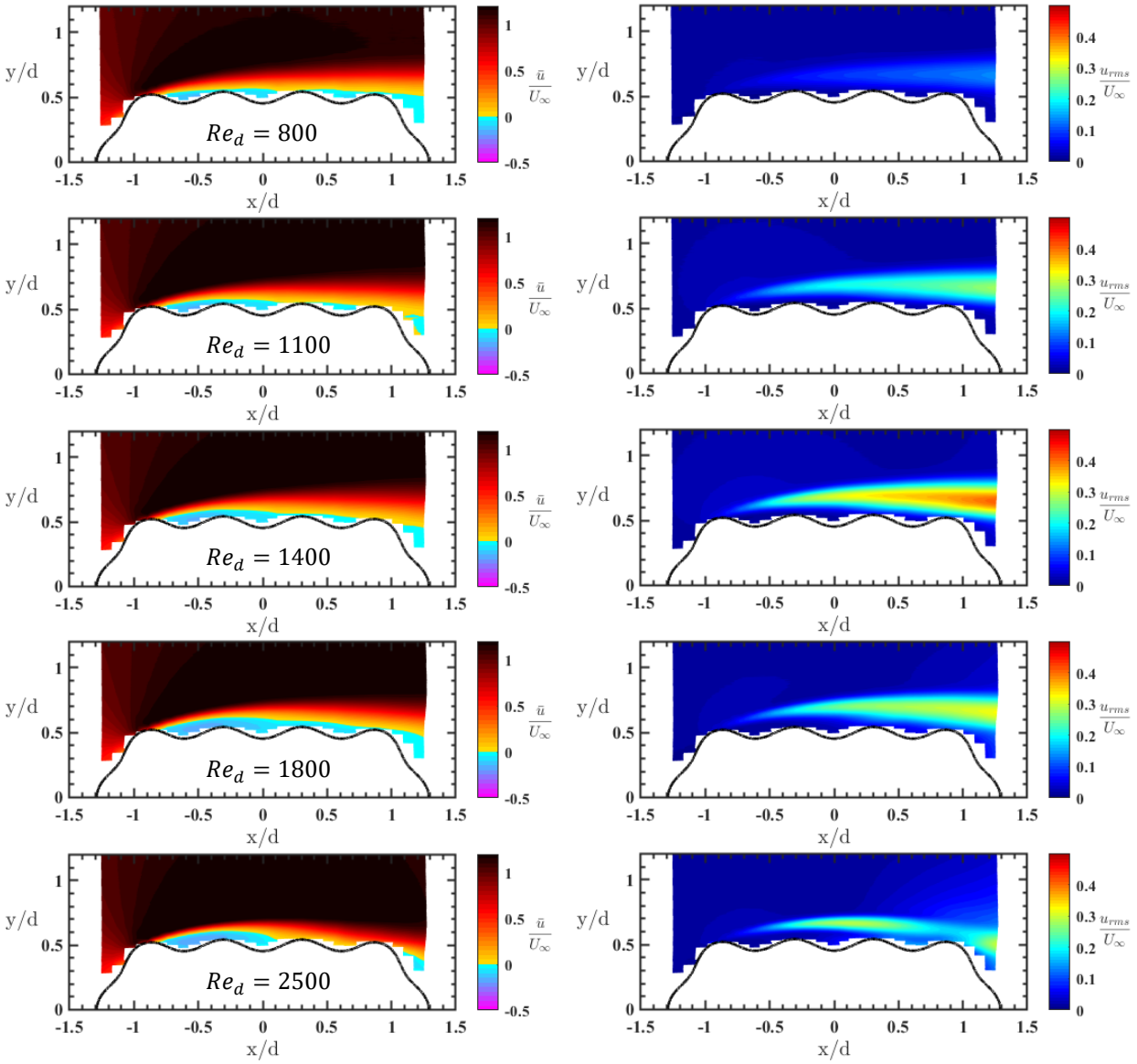

Figure 28. 3Dp-5% cylinder. Mean (left) and rms (right) velocity color contour maps normalized by the freestream velocity U_∞. Rows show different Reynolds numbers. Flow is from left to right.

The separation bubble for the 3Dp geometry remains open over the surface at $Re_d = 800$, although it is located very close to the surface and becomes extremely close to reattaching at the topology peaks. As the Reynolds number increases to $Re_d = 1100$ and 1400, the flow reattaches to the surface upstream of a topology peak and ahead of the trailing edge. Further increase of Reynolds number to $Re_d = 1800$ is seen to again move the separation bubble towards opening, although it remains thin and very close to the surface. The overall behavior at this Reynolds

number range of $Re_d = 800 - 1800$ is more comparable to that seen from the 2Dv case and deviates visibly from that of the 2Dp cylinder (as seen from Figure 29). The separated flow reattaches to the surface at $Re_d = 2500$ slightly after the mid-chord of the cylinder, upstream of a topology peak. The flow does not separate again until the topology peak at the aft corner of the cylinder. This is a considerable alteration of the reattachment behavior of the separated flow in comparison to the 2Dp geometry. More specifically, the reattachment point advances towards the leading edge compared to the 2Dp counterpart, the separation zone of which is shown in red in Figure 29. Overall, the presence of topology three-dimensionality makes the separation bubble thinner and more likely to reattach at all Reynolds numbers.

From the rms velocity shown in the right column of Figure 28, it can be seen that, except at $Re_d = 2500$, the unsteadiness levels keep growing with downstream distance. Also, the region with high rms velocity values remains close to the surface. The trend of fluctuations intensity does not show a monotonic behavior with respect to Reynolds number, where the shear layer remains fairly quiet at $Re_d = 800$, gains fluctuation intensity at higher Reynolds numbers up to $Re_d = 1400$, and again loses fluctuation intensity as the Reynolds number increases to $Re_d = 2500$. To further characterize the shear layer, the domain of high rms fluctuations is depicted in Figure 30. Comparing the 3Dp case with its 2D counterpart, it can be seen that the presence of three-dimensionality in the topology pulls this domain closer to the surface and keeps it laterally more compact.

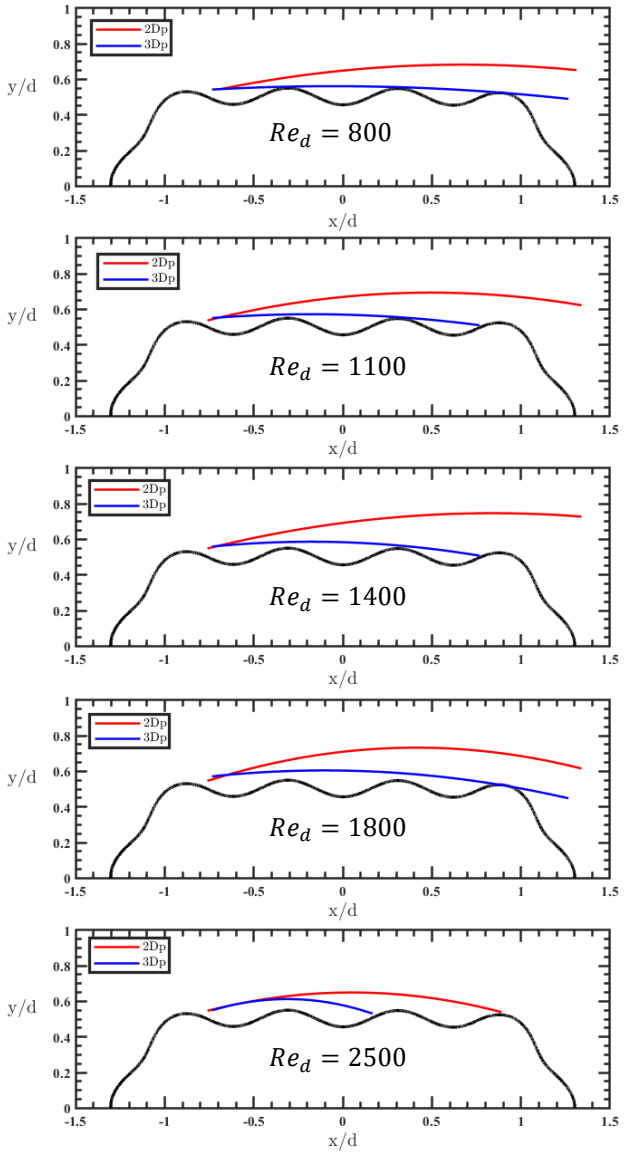

Figure 29. Comparison of the mean separation zone boundary for the 2Dp and 3Dp cylinders, shown in red and blue lines, respectively. Rows show different Reynolds numbers. Flow is from left to right.

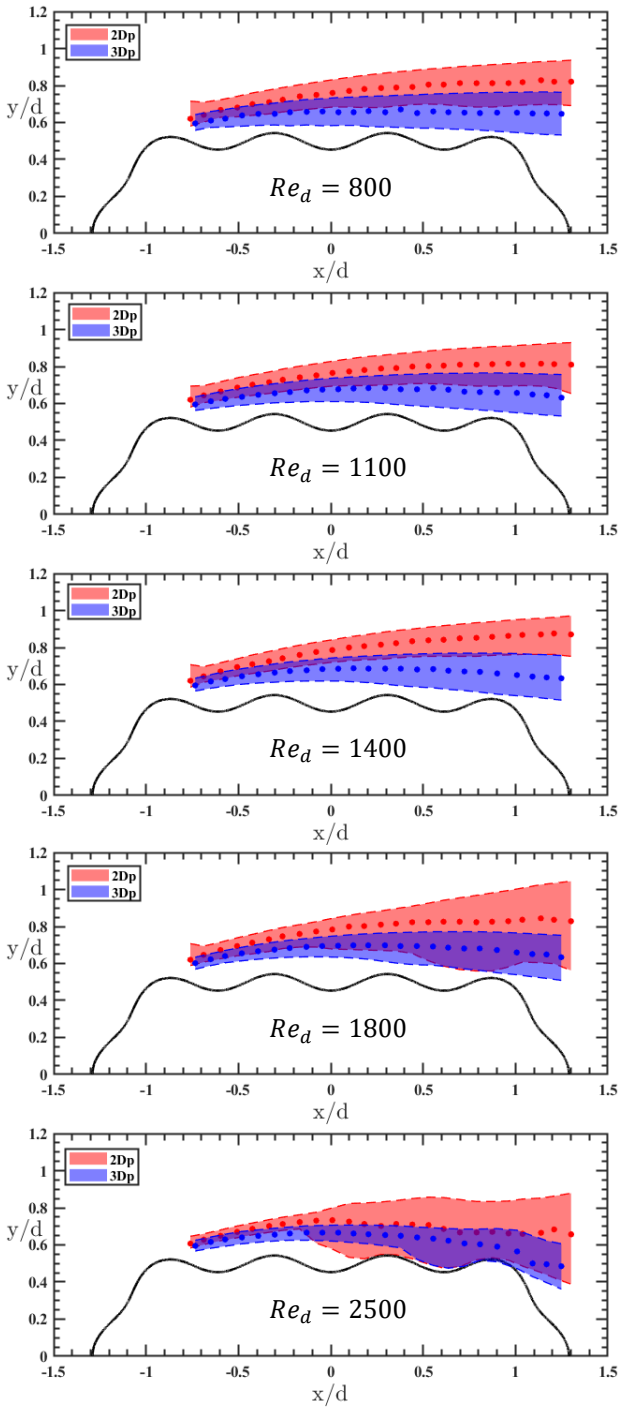

Figure 30. Domain of high rms velocity fluctuations, covering the region with rms velocity higher than 50% of the maximum rms velocity at each x/d location. 2Dp and 3Dp cases shown in red and blue, respectively. Flow is from left to right.

The spreading behavior of the high u_{rms} zone remains close between the 2Dp and 3Dp cylinders at the lower Reynolds number range of $Re_d = 800 - 1400$, where both cylinders show

a trend consistent with the gradual growth of mixing layers. It is only at $Re_d = 2500$ where the 3Dp geometry shows a rapid expansion of the highly unsteady domain around $x/d = 0.4$, where the fluctuations penetrate a topology valley, rather than merely sweeping above the peaks. This observation suggests the development of vortical structures downstream of $x/d = 0.4$, which is farther downstream compared to the 2D counterpart.

The maximum rms velocity value across each profile is extracted and plotted versus x/d at each Reynolds number, as seen in Figure 31. Unlike in the 2Dp case where $u_{rms,p}$ growth rate does not change much with x, the 3Dp case shows significant dependence with the growth rate generally decaying with x. The fluctuations in the shear layer increase more rapidly over the surface of the 3Dp case up to about the mid-chord compared to the 2Dp cylinder. However, farther downstream, the 2D counterpart shows a faster unsteadiness growth. At some Reynolds numbers (i.e. $Re_d = 1100, 1800, 2500$) the maximum u_{rms} values for the 2Dp case surpass those of the 3Dp case after the mid-chord. At $Re_d = 800$ and 1,400, the unsteadiness level is dominantly higher for the 2Dp and 3Dp, respectively. One interesting case is the 3Dp at $Re_d = 2500$, where the fluctuations even drop after the mid-chord and reach a minimum at $x/d \approx 0.9$. For this case, the decreasing trend starts very close to where the flow reattaches to the surface and lingers in the reattached flow up to the whereabouts of the next separation point at the topology peak at the aft corner of the cylinder.

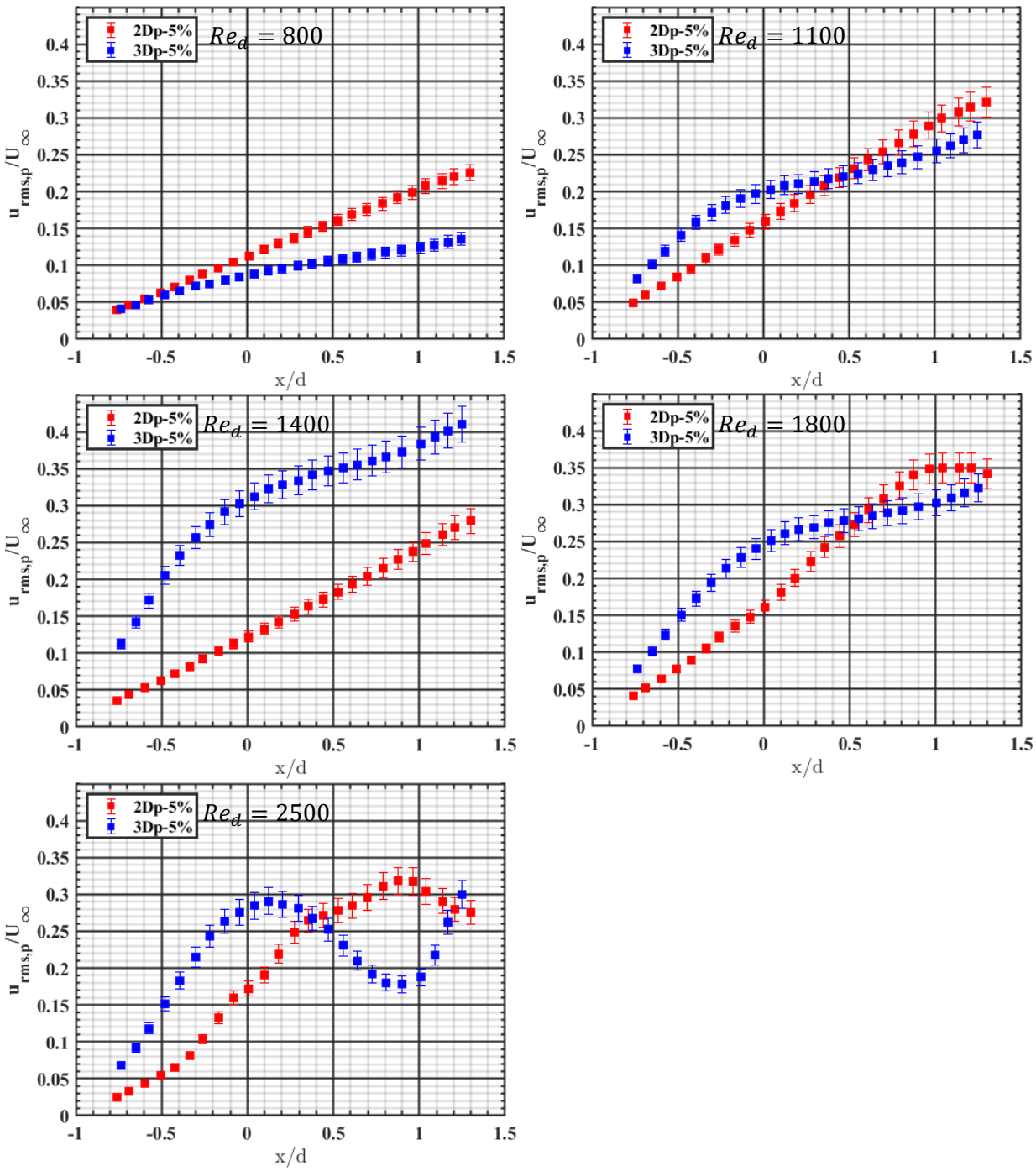

Figure 31. Comparison between maximum u_{rms}/U_∞ values along the surface of the 2Dp (red), and 3Dp (blue) cylinders, at different Reynolds numbers.

The effect of adding surface topology variation along the span on the velocity field over the cross-sectional geometries with a valley at the leading edge is examined using Figure 32. From the mean velocity color contour maps on the left of this figure, it can be seen that the presence of

the surface topology variation along the span has a small effect on the separation/reattachment behavior of the flow over the surface compared to the counterpart 2Dv cylinder.

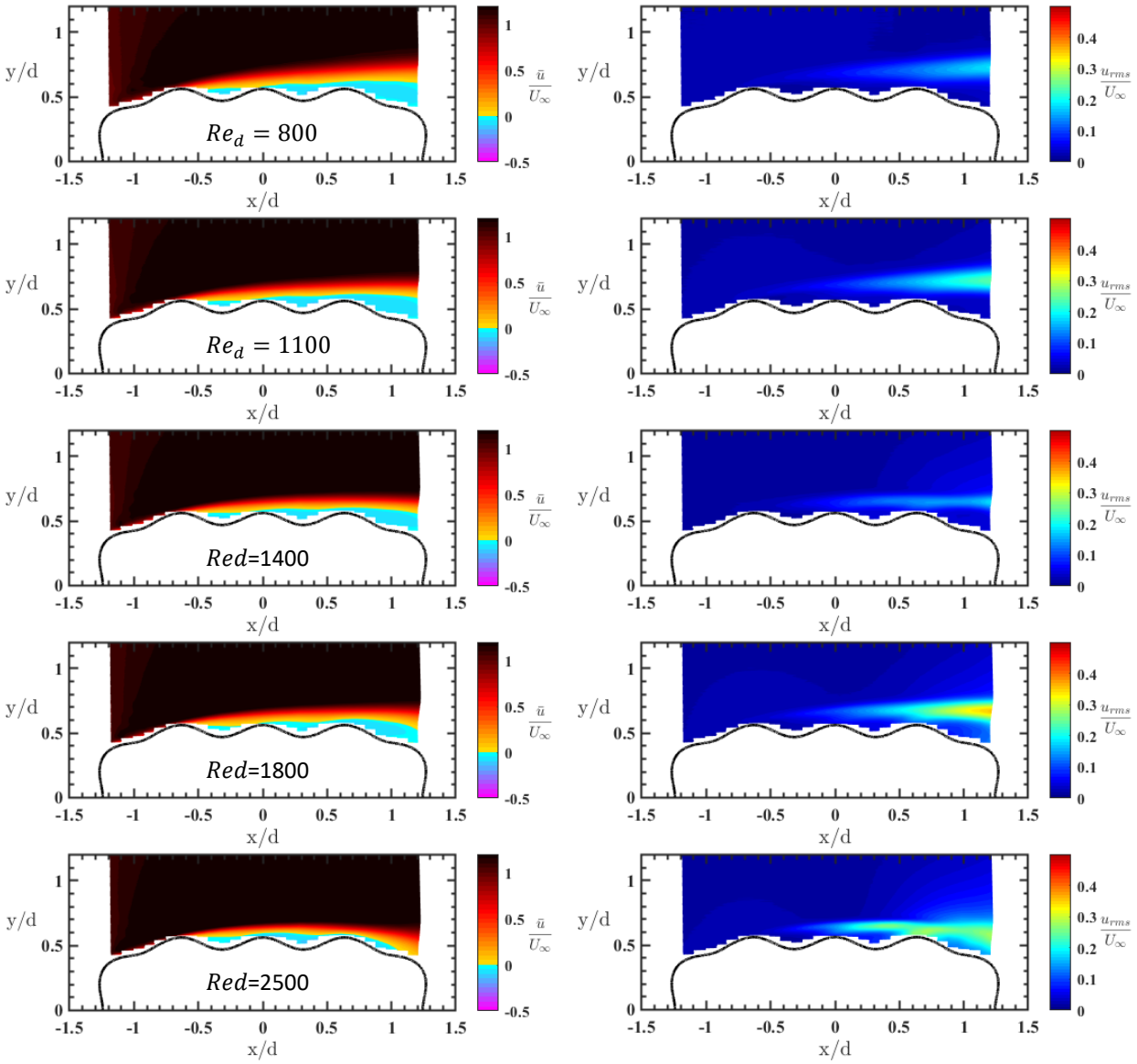

Figure 32. 3Dv-5% cylinder. Mean (left) and rms (right) velocity color contour maps normalized by the freestream velocity U_∞. Rows show different Reynolds numbers. Flow is from left to right.

Overall, the separated flow remains fairly close to the surface, predominantly filling the topology valleys and becoming close to reattachment at the topology peaks. The reverse flow region seems to gain lateral thickness downstream, which is the opposite of the behavior observed in Figure 28 for the other cross-section of this 3D cylinder with a peak at the leading edge.

Furthermore, the reverse flow region seems to be quite insensitive to Reynolds number in the studied range.

The separation zone boundary for the 3Dv case is characterized in Figure 33 to extract further information regarding the mean boundary layer behavior. The separation point remains close to that of the 2D counterpart, located downstream of a topology peak at $x/d \approx -0.5$ and not affected by Reynolds number. Flow does not reattach at any Reynolds number, although the separation zone boundary remains close to the surface and becomes very close to the topology peaks. Increasing the Reynolds number increases the curvature of the mean separation boundary and brings it closer to the surface farther downstream. Overall, the presence of the three-dimensionality for this cross-sectional geometry seems to make the reattachment more difficult and the separation bubble laterally thicker at $Re_d = 800 - 1800$. It is only at a high enough Reynolds number $Re_d = 2500$ that the separation zone boundary becomes more curved and approaches the surface sooner for the 3Dv compared to 2Dv. The second-order polynomial fit does not accurately represent the separation zone boundary for 3Dv at $Re_d = 2500$. Although the fit suggests an open separation for this case, the color map gives signs of possible reattachment to the surface upstream of the topology peak at the aft corner of the cylinder.

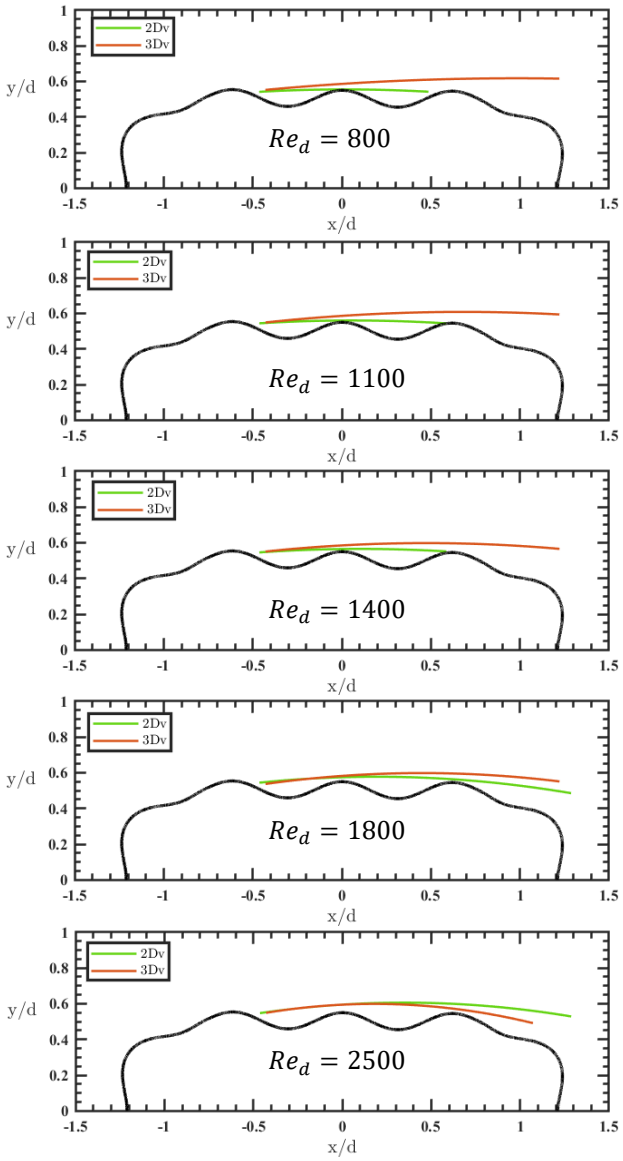

Figure 33. Comparison of the mean separation zone boundary for the 2Dv and 3Dv cylinders, shown in green and brown lines, respectively. Rows show different Reynolds numbers. Flow is from left to right.

Investigating the rms velocity shown in the right column of Figure 32, it can be seen that the overall unsteadiness level keeps growing with the downstream distance. Similar to most of the cases studied so far, the unsteadiness level does not show a monotonic behavior with Reynolds number. What is consistent is that the rms velocity values remain reasonably low over most of the surface and the high unsteadiness intensities show up only late above the downstream half of the surface. One peculiar and interesting observation is that at $Re_d = 1400$, the unsteadiness level for

the 3Dv case is very low and limited to a narrow band, while the other cross-section of this cylinder with a peak at the leading edge (3Dp) shows its highest fluctuation rates at this Reynolds number.

To further characterize the shear layer for the 3Dv cylinder, the domain of high rms fluctuations is depicted in Figure 34, where it is compared with the 2D counterpart. At lower Reynolds numbers of $Re_d = 800 - 1400$, this domain remains thinner but farther from the surface for the 3Dv case. As the Reynolds number increases, the domain for the 3Dv case grows laterally to become thicker than that of the 2D counterpart at $Re_d = 2500$, where it also moves closer to the surface than the domain for 2Dv case. At this Reynolds number, a rapid expansion of the domain is seen at around $x/d = 0.65$, downstream of a topology peak, which is believed to be an indication of the spanwise vortical structures' formation and development.

The maximum rms velocity value across each profile is extracted and plotted versus x/d at each Reynolds number, as seen in Figure 35. Throughout the studied Reynolds number range, the maximum rms velocity values are significantly higher above the 3Dv surface compared against the 2D counterpart. The $u_{rms,p}$ growth rate does not change much with x for the geometries with a valley at the leading edge, apart from $Re_d = 1400$ and 2500 where some "saturation" is observed in the growth.

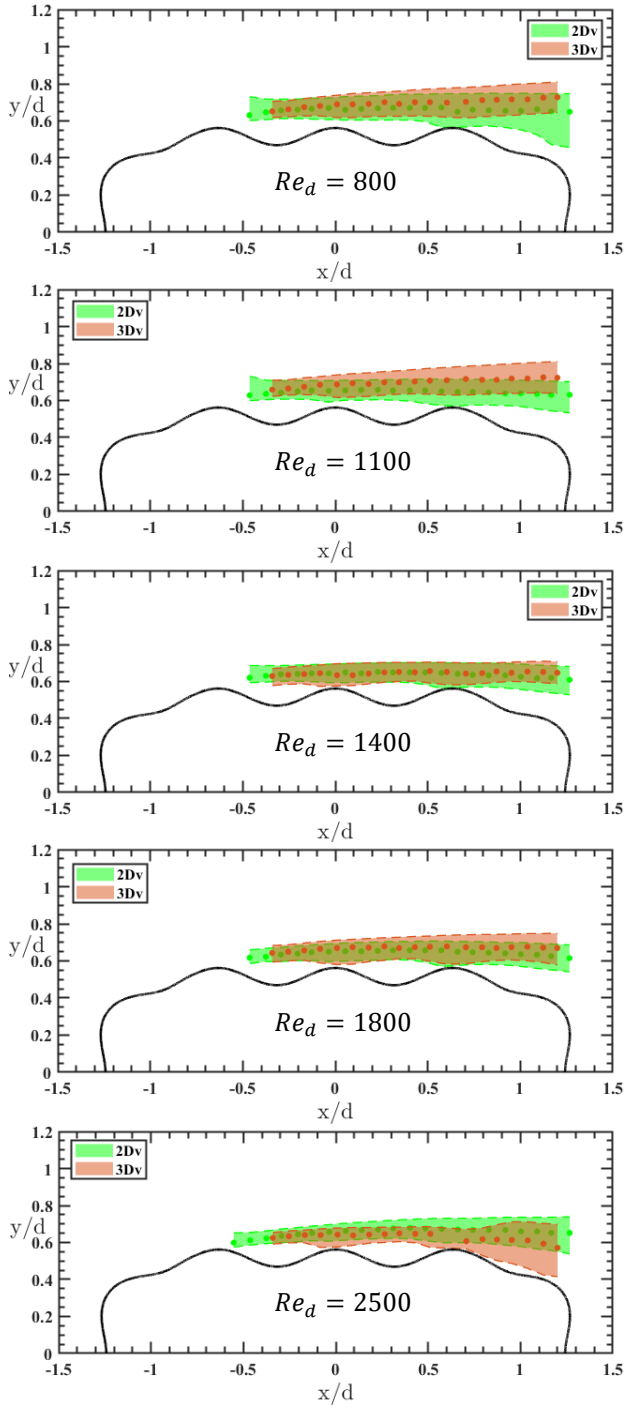

Figure 34. Domain of high rms velocity fluctuations, covering the region with rms velocity larger than 50% of the maximum rms velocity at each x/d location. 2Dv and 3Dv cases shown in green and brown, respectively. Flow is from left to right.

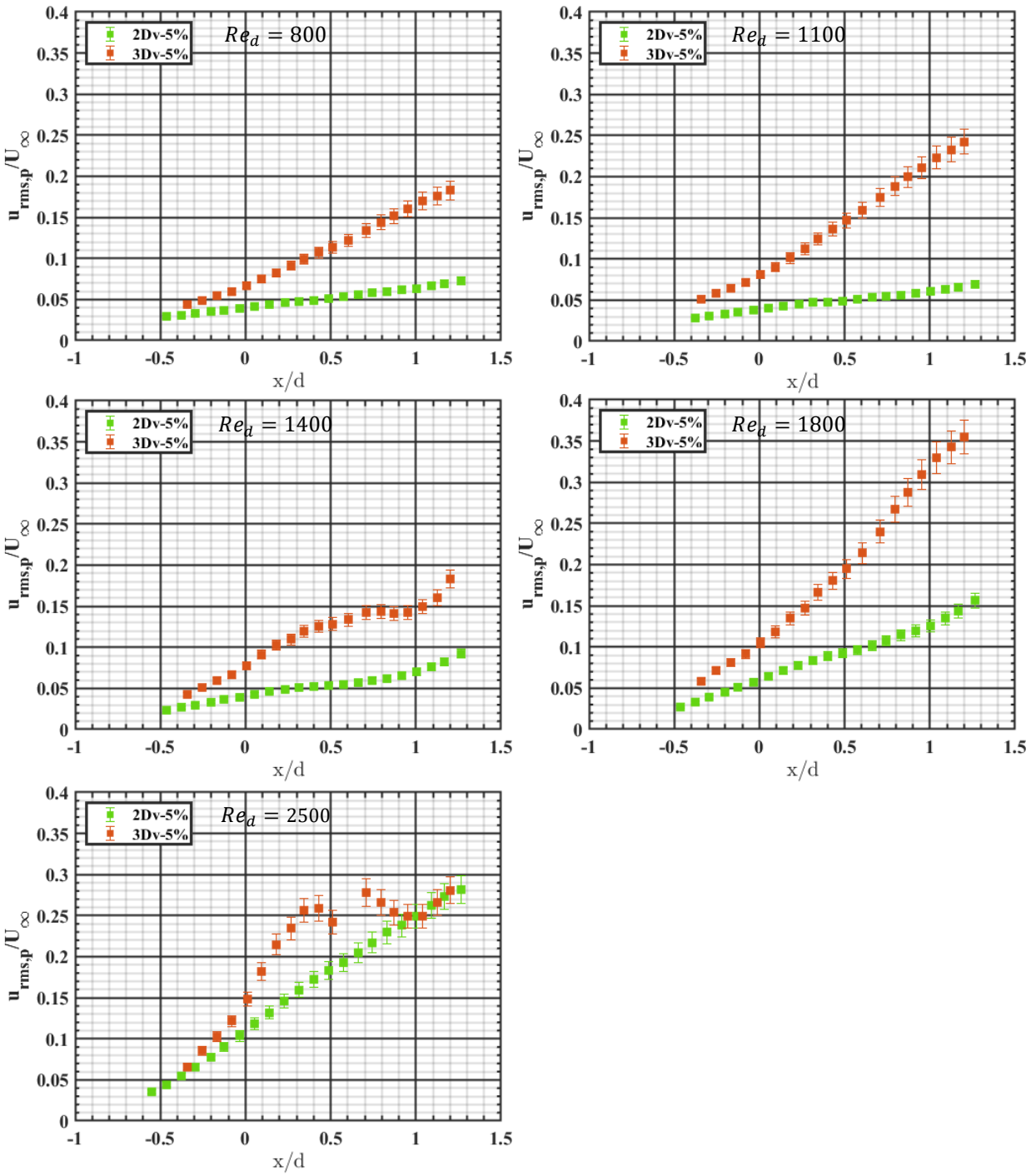

Figure 35. Comparison between maximum u_{rms}/U_∞ values along the surface of the 2Dv (green) and 3Dv (brown) cylinders, at different Reynolds numbers.

3.4 On Galloping

When studying galloping oscillations of the rectangular cylinders in the conditions valid for quasi-steady assumption, the classic understanding of the phenomenon is that, as the angle of attack increases, the separated shear layer on the bottom curves more towards the surface, hence generating higher suction than that from the top shear layer (see Figure 36). This increasing pressure difference between the top and bottom lateral surfaces produces an increasing downward (positive, per axis definition in Figure 1) force F_y that causes the cylinder to become unstable to galloping.

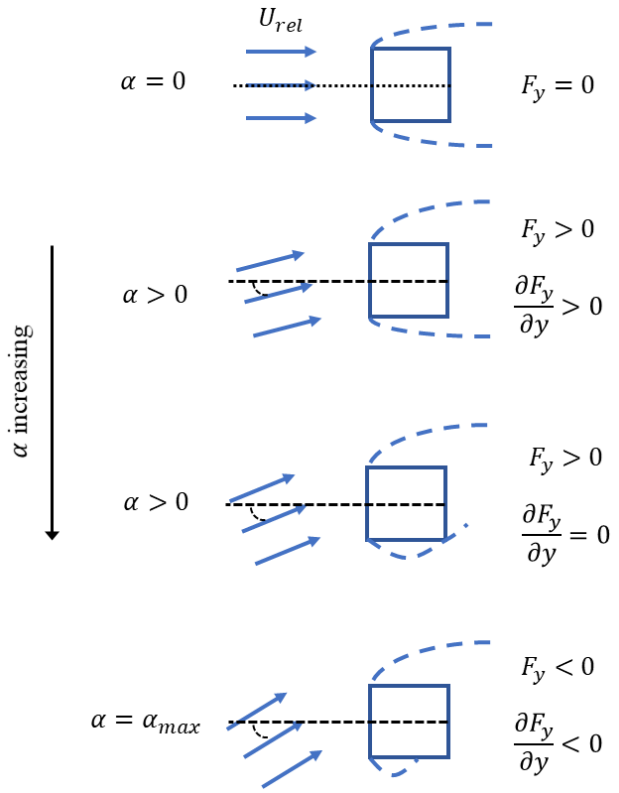

Figure 36. Classic understanding of the galloping phenomenon, connecting the boundary layer separation behavior to pressure generation on the side surfaces and, hence, transverse galloping force (sketch is done following Naudascher & Rockwell [21]).

The bottom shear layer reattaches to the surface at a high enough angle of attack, resulting in increasing suction on the bottom and reduction in F_y with further increase of the angle of attack,

flipping the instability-promoting trend of F_y with α. This reversed trend is related to the upstream movement of the reattachment point on the bottom surface with increasing angle of attack post reattachment of the shear layer. In other words, the literature indicates that a rectangular cylinder is unstable to galloping when the shear layer on its bottom is separated and stable when it reattaches. Given Equation 1 (see Chapter 1) $F_L \approx -F_y$ at small angles of attack and the galloping behavior can be predicted using the lift coefficient, when the quasi-steady assumption holds. Therefore, the galloping behavior of the bluff bodies can be contrasted against that of the streamline objects, such as a symmetric airfoil, by considering the $C_L - \alpha$ curve. It is well stablished that for such bodies, the lift coefficient increases with increasing the angle of attack up to the critical angle of the stall. Up to stall, the flow on top of the airfoil either follows the surface closely (at high Reynolds number) or a closed separation bubble is formed (at low Reynolds number) and an attached flow is present on the bottom surface. Therefore, there is a net suction on the top and positive pressure on the bottom, resulting in a positive slope of the $C_L - \alpha$ curve up to stall. Hence, the *transverse* galloping phenomenon is primarily a bluff, rather than a streamline body problem.

New studies [7-9], however, suggest that, at sufficiently low Reynolds number, there are factors other than separation/reattachment on the bottom surface that contribute to galloping instability. Surface pressure measurements from Feero et. al [9] on a sharp-cornered cylinder with $c/d = 3$ at $Re_d = 1100$ show that despite the reattachment of the shear layer to the bottom surface at $\alpha = 0°$, the cylinder is unstable to galloping. They relate this observation, which is contradictory to the classic understanding described above, to two factors. First, they find that the separation-zone pressure on the top surface rises with increasing the angle of attack to cause a net overall increase in the average pressure on the surface, promoting an increase in F_y with α (which is a

destabilizing effect). This net pressure increase with AoA is opposite to that observed at higher Reynolds numbers of $Re_d = 5000$ and 10000. The second factor contributing to the unexpected instability to galloping of the cylinder, is the observation that unlike at $Re_d = 5000$ and 10000, at $Re_d = 1100$, the reattachment point on the bottom surface does not move upstream with increasing the angle of attack. Based on the discussion in the previous paragraph, the reattachment point not shifting upstream suggests that the pressure on the bottom surface does not increase with angle of attack, and therefore there is no mechanism for F_y to decrease with α to stabilize the geometry. Although surface pressure data are not available for the current cases of study, this chapter is focused on analyzing the galloping behavior of the cylinders based on the links understood in literature between the shear layer separation/reattachment change with AoA and galloping instability.

The separation zone boundary of the smooth cylinder at three Reynolds numbers, $Re_d = 800$, 1400, and 2500, and five different angles of attack is shown in Figure 37. At $\alpha = 0°$, there is a very thin closed-separation bubble at all the Reynolds numbers. At higher angles of attack, separation occurs on the top side of the cylinder at all Reynolds numbers downstream of the leading-edge round-corner. The separated shear layer at $Re_d = 800$ stays reattached to the top surface as the angle of attack is increased to $\alpha = 1°$, but becomes open at higher angles of attack. As the Reynolds number increases to $Re_d = 1400$, the separation bubble remains closed up to a lower angle $\alpha = 0.5°$. Further increase in the Reynolds number shows a closed separation bubble on the top surface only at $\alpha = 0°$. Therefore, it is observed that increasing the Reynolds number in this range makes the separation bubble on the top surface of the smooth cylinder prone to becoming open at a lower angle of attack.

On the bottom side of the cylinder, the flow remains attached at $Re_d = 800$ and 1400 as α increases, but shows a very thin closed separation bubble at $Re_d = 2500$ which shrinks as α increases. This behavior of the bottom shear layer should lead to an increase of the pressure on the bottom side with increasing AoA. Thus, the bottom surface is expected to contribute to increasing lift with AoA. A similar contribution to lift is possible from the top surface prior to opening of the separation bubble, with the latter reversing the trend. Moreover, given the tendency of the separation bubble on the top side of the cylinder to become open with increasing Re_d, the top surface contribution to positive lift is anticipated to decrease with Re_d.

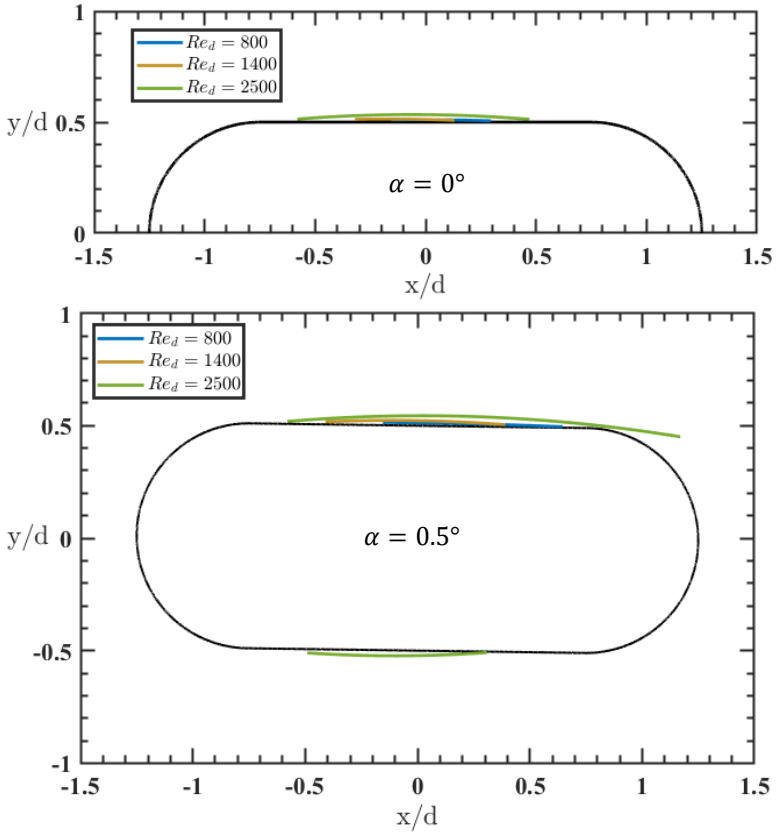

Figure 37. Comparison of the mean separation zone boundary for the smooth cylinder at different angles of attack (different rows) and Reynolds numbers.

Figure 37 (cont'd)

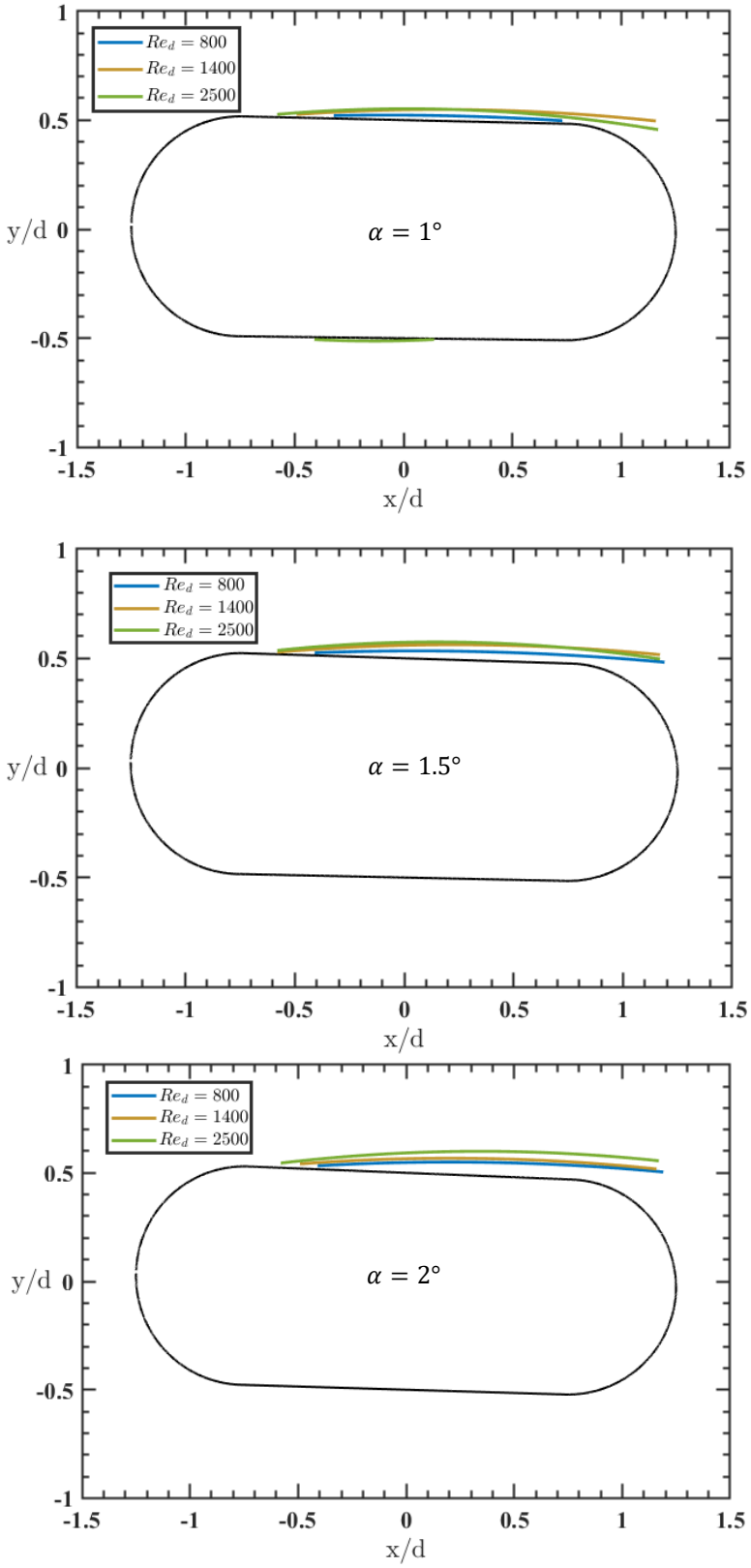

Noting that $C_L \approx -C_y$ for small α, the above inferences are consistent with the $C_y - \alpha$ curves of the same cylinder geometry from Feero et al. [7, 8] (see Figure 2-left). Specifically, all curves exhibit a decrease of C_y with angle of attack for small α values (i.e increasing C_L with α), which indicates stability to galloping.

The separation zone boundary for the 2Dp cylinder is depicted in Figure 38. Focusing on the results at $\alpha = 0°$ at the lower $Re_d = 800$ and 1400, the boundary layer separates downstream of the first bump located along the LE corner of the baseline geometry. Reynolds number seems to have a very small influence on the separation location. On the other hand, while the separated shear layer remains open at the low Reynolds numbers, the shear layer probably reattaches upstream of the last lateral topology bump at $Re_d = 2500$.

The observations in the previous paragraph were discussed earlier in Section 3.1. To connect the features of boundary layer separation/reattachment to galloping instability, it is important to examine how these features change with increasing the angle of attack. Referring to Figure 38, the separation remains open on the top and the bottom of the 2Dp cylinder at $Re_d = 800$ and 1400 as α is increased up to 1.5°. This behavior is reminiscent of that of the sharp-corner rectangular cylinders that are unstable to galloping (Parkinson [4]), and hence one may expect instability to galloping for this cylinder at $Re_d = 800$ and 1400. As the angle of attack is increased further to 2° (Figure 38-bottom), the shear layer reattaches on the bottom side, upstream of the topology peak at the aft corner of the cylinder, at $Re_d = 800$, suggesting pressure recovery on the bottom side and a switch of the $C_y - \alpha$ slope sign at $\alpha \approx 2°$. However, no reattachment is observed at $Re_d = 1400$, suggesting that the cylinder remains unstable to galloping over the examined range of AoA at this Reynolds number.

Increasing Reynolds number to 2500 causes the separated shear layer to remain very close to reattaching to the top surface of the 2Dp cylinder up to $\alpha = 1°$, somewhere over the topology peak at the aft corner of the cylinder. Further increase to $\alpha = 1.5°$, leads to opening of the separation bubble. In contrast, on the bottom side of the 2Dp case, the flow separates downstream of the topology peak at the front corner, and reattaches upstream of the topology peak at the aft corner at all measured angles of attack. The separation bubble on the bottom side is not shrinking significantly with α, which as stated earlier, is found in [9] to be important for the stability to galloping. On the other hand, considering the shear layer on the top side being close to reattachment to the cylinder, a stronger suction pressure (and hence higher lift) might be developing with increasing AoA, which is a stabilizing effect. It is not known which of these two effects would be stronger, and hence is it uncertain if the 2Dp cylinder is stable or unstable at $Re = 2{,}500$.

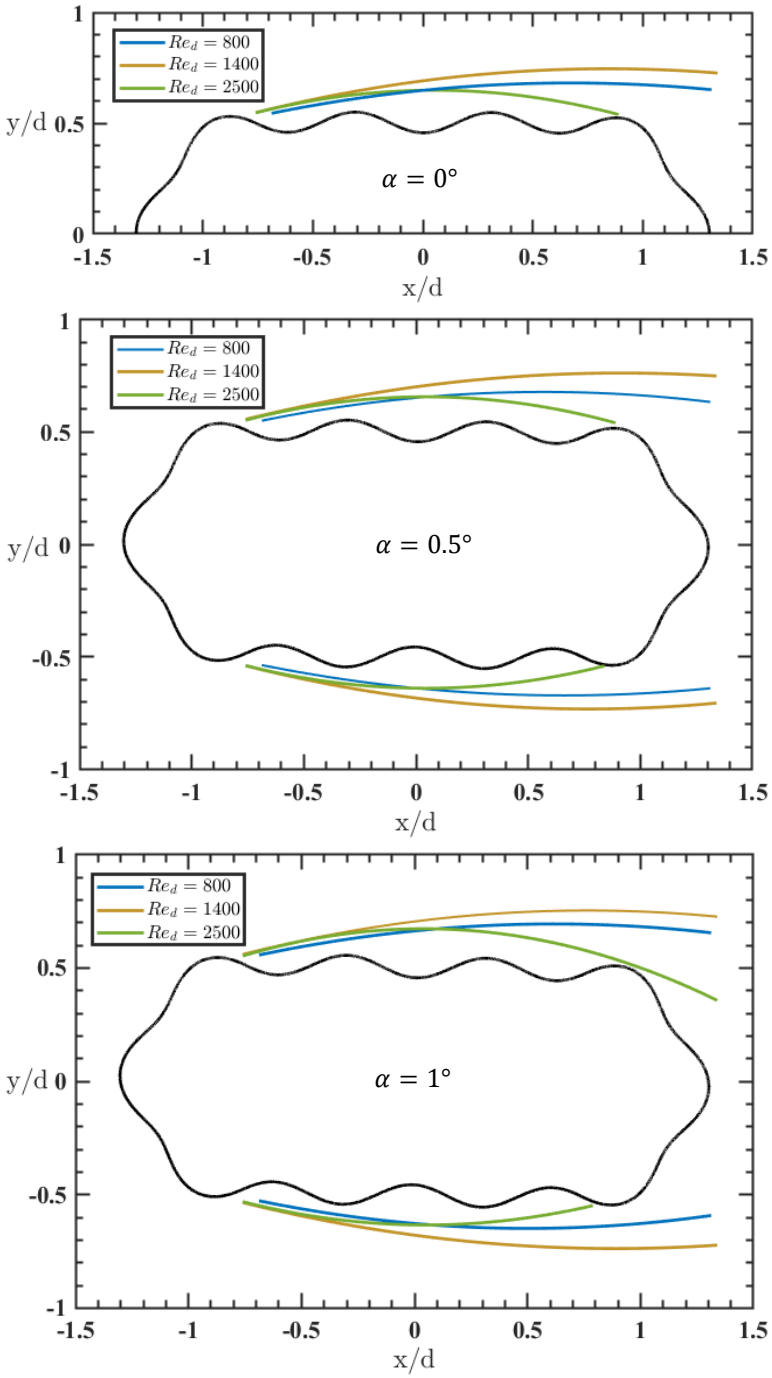

Figure 38. Comparison of the mean separation zone boundary for the 2Dp-5% cylinder at different angles of attack (different rows) and Reynolds numbers.

Figure 38 (cont'd)

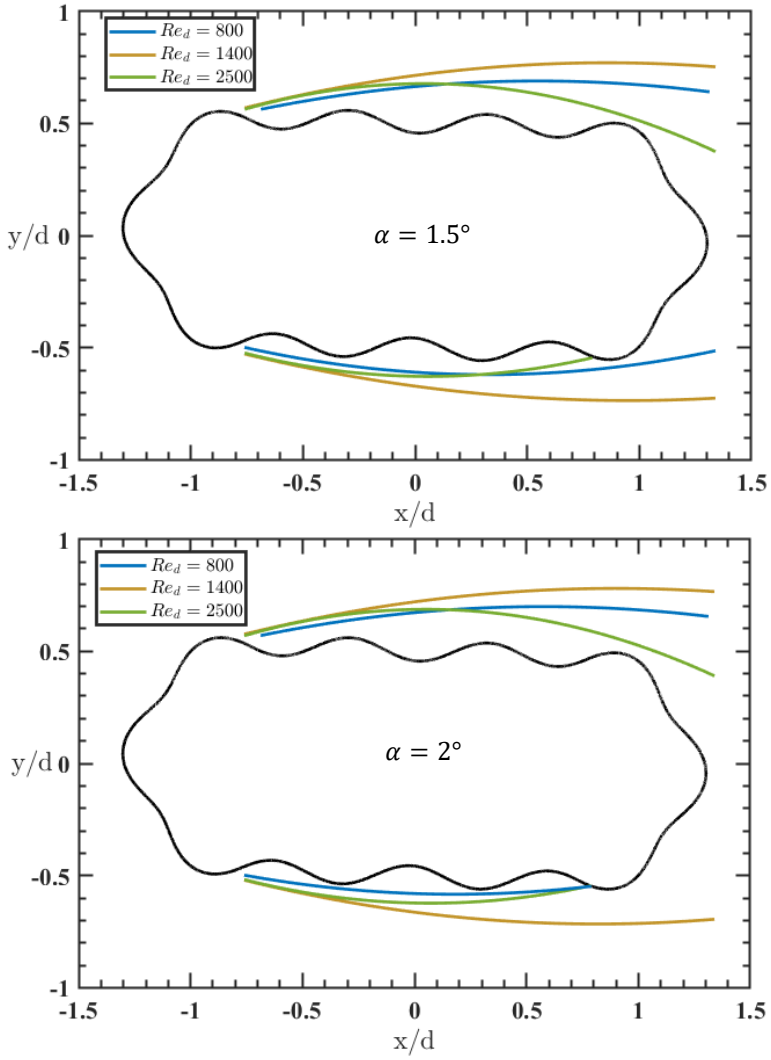

Results for the 2Dv are shown in Figure 39, where the separation zone boundary is not depicted for any localized separation bubbles within the valleys of the topology. The separation bubble remains closed over the top surface at $Re_d = 800$ as the angle of attack increases to $\alpha = 0.5°$. With further increasing the angle of attack, the separation bubble becomes open, but remains very thin. The shear layer on the bottom surface forms two isolated separation bubbles, filling the topology valleys, with increasing the angle of attack (not plotted). Similar trend is observed at $Re_d = 1400$, but opening of the separation bubble on the top is promoted and is observed at $\alpha = 0.5°$. In addition, the separation bubble on the bottom is observed at higher angles of attack and

the isolated bubbles in the dips are seen as late as $\alpha = 1°$. At $Re_d = 2500$, the separated shear layer does not reattach to the top surface and moves farther from the surface with increasing α. Reattachment of the separated shear layer is observed to the bottom surface, upstream of last topology peak on the surface at $\alpha = 2°$.

For the lower Reynolds numbers $Re_d = 800$ and 1400, the separation zone boundary on the bottom is generally very thin and the shear layer is reattached. Thus, the flow generally follows the baseline shape of the cylinder on the bottom side, which would likely lead to increased bottom surface pressure with AoA, contributing to stability to galloping. The reattachment of the top shear layer at $Re_d = 800$ and small angles of attack is expected to improve the stability to galloping (increasing C_L) for this geometry. It is difficult to judge the pressure variation on the top surface at $Re_d = 1400$, since the curvature of the top separation bubble only minimally changes at $\alpha > 0$. With the top shear layer failing to reattach as the Reynolds number increases to $Re_d = 2500$, the geometry behaves similar to a sharp corner rectangular cylinder which is prone to galloping. Therefore, increasing the Reynolds number in the studied range is expected to make the 2Dv cylinder more unstable.

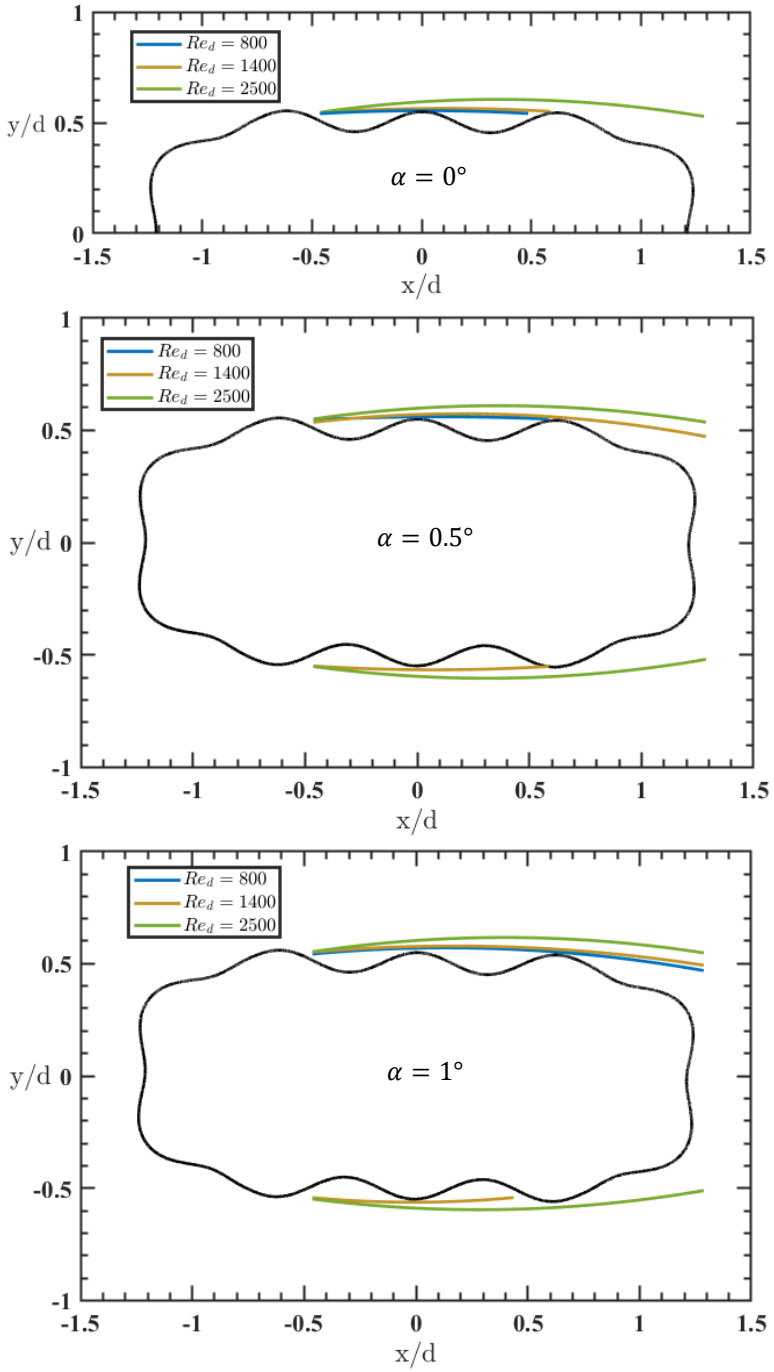

Figure 39. Comparison of the mean separation zone boundary for the 2Dv-5% cylinder at different angles of attack (different rows) and Reynolds numbers.

Figure 39 (cont'd)

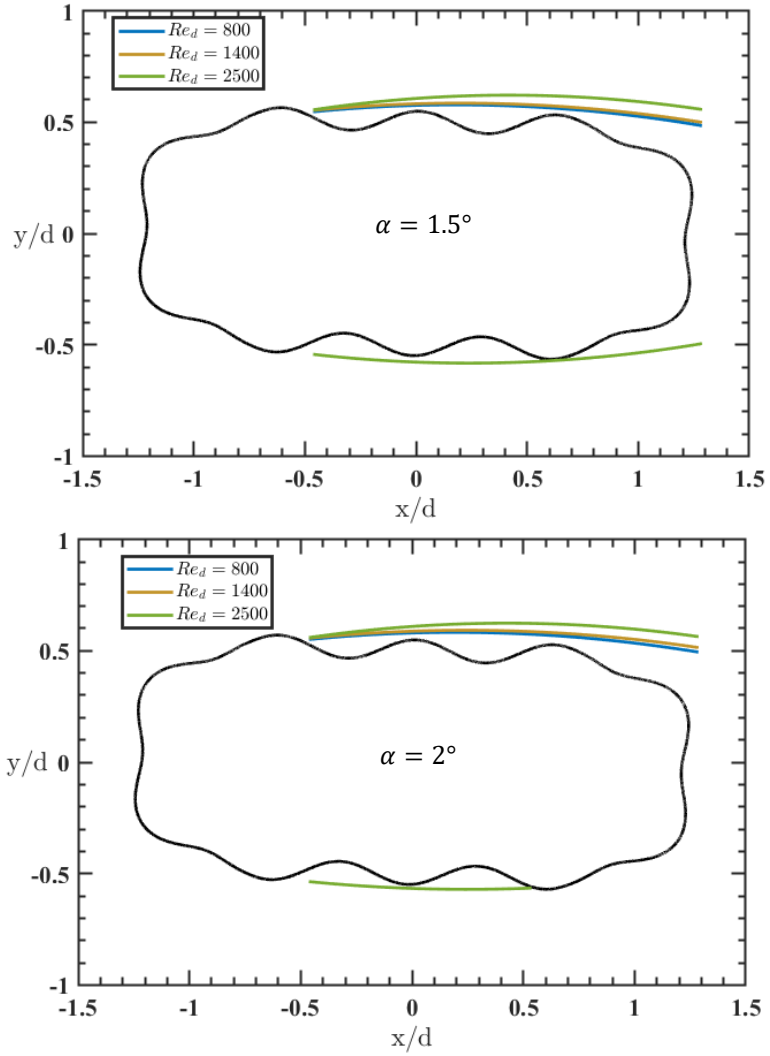

Proceeding to consider the 3D geometry, Figure 40 shows that for all angles of attack, the presence of topology variation along the span leads the separated shear layer on both sides of the 3Dp cylinder to move closer to the surface compared to the 2Dp case (seen in Figure 38). The separation bubble on the top surface becomes very close to reattachment over the topology peak at the aft corner of the cylinder at $\alpha = 0°$ and $Re_d = 800$, but reattachment cannot be ascertained. With a slight increase in the angle of attack to $\alpha = 0.5°$, the separation bubble becomes clearly open and the separation zone boundary moves farther from the surface and has lower curvature with further increase of the angle of attack. This is expected to contribute to lower suction pressure

on the top, hence lower lift at higher α. On the bottom surface, the bottom shear layer reattaches to the surface at $\alpha = 0.5°$, upstream of the topology peak at the aft corner of the cylinder. With further increasing the angle of attack, three isolated separation bubbles form inside the topology valleys on the bottom surface. The bottom shear layer generally behaves more like an attached flow, following the overall shape of the body, and is therefore expected to contribute to stability against galloping. Overall, the 3Dp case at $Re_d = 800$ behaves like a rectangular cylinder with sharp corners at high Reynolds numbers, where the bottom shear layer is reattached and moves upstream with increasing the angle of attack, but the top shear layer remains fully separated. This is a classic galloping problem studied in the literature [4] and is expected to be stable to galloping. At the higher Reynolds numbers $Re_d = 1400$ and 2500, the top shear layer remains reattached to the surface as the angle of attack increases to $\alpha = 1°$ and $1.5°$, respectively. Therefore, the top shear layer is expected to impose higher suction pressure on the surface and contribute to higher lift, up to these angles of attack. Beyond $\alpha = 1.5°$ at $Re_d = 1400$, and $\alpha = 2°$ at $Re_d = 2500$, the top separated shear layer fails to reattach, and the suction pressure on the top surface is expected to drop. The separation bubble on the bottom is closed at these Reynolds numbers and the flow generally follows the baseline shape of the cylinder on the bottom side. The contribution of the bottom shear layer, therefore, is likely to increase the pressure recovery with angle of attack and stability to galloping. Without surface pressure measurements, it is difficult to determine whether the stabilizing behavior of the bottom shear layer will overcome the destabilizing effect of the top shear layer.

The effect of Reynolds number is noted to be enhancing the reattachment of the separated shear layer on the top surface, hence, improving the stability to galloping. Overall, due to the associated higher curvature of the shear layer on the top surface, higher suction pressure relative

to the 2Dp case is expected; i.e. promoting an increase in lift and stability to galloping. On the bottom side, the shear layer reattachment is expedited and a higher pressure recovery is expected for the 3Dp case. This behavior is anticipated to contribute further to the increase in lift and stability to galloping for the 3Dp case compared to its 2D counterpart. It should be noted, however, that the behavior of the 3D cylinder as a whole cannot be solely determined by looking at the single cross-section corresponding to the 2Dp shape, since the cylinder cross-section varies along the span.

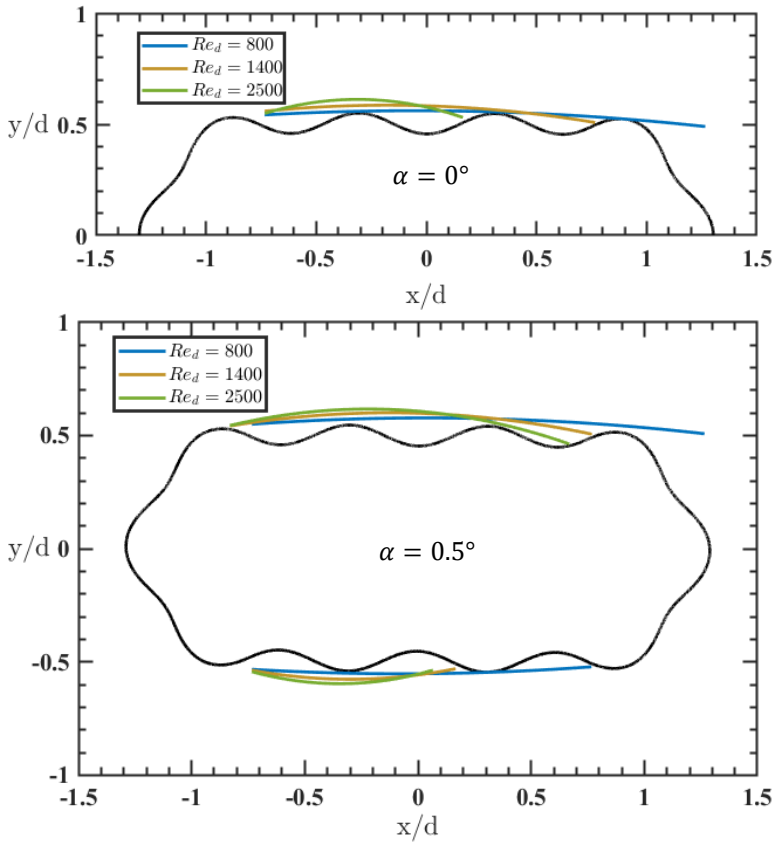

Figure 40. Comparison of the mean separation zone boundary for the 3Dp-5% cylinder at different angles of attack (different rows) and Reynolds numbers.

Figure 40 (cont'd)

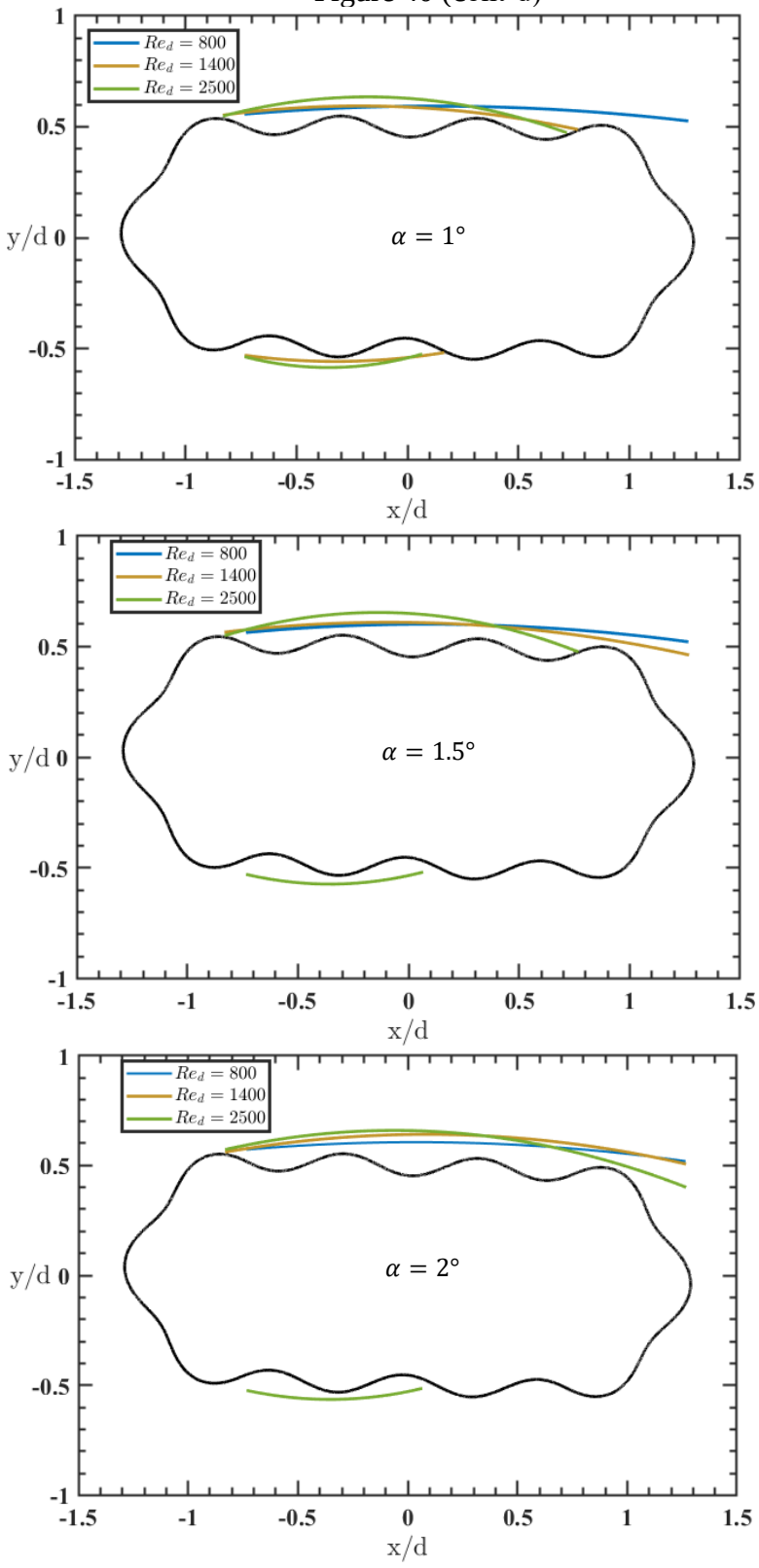

Results from MTV measurement on the cross section of the 3D cylinder with a valley at the leading edge are presented in Figure 41. The top shear layer separates downstream of a topology peak and does not reattach at the lower Reynolds numbers $Re_d = 800$ and 1400. The separation point on the bottom surface seems to be similar to that on the top, being downstream of a topology peak. As the angle of attack increases, the separated shear layer on the bottom moves closer to the surface and becomes very close to reattachment at $\alpha = 1°$ at the mentioned Reynolds numbers, but full reattachment is not certain until $\alpha = 1.5°$, which happens over the last topology peak on the surface. At $\alpha = 2°$, two isolated closed separation bubbles are observed at $Re_d = 800$, which are not shown in Figure 41. Although the stability of this cylinder to galloping cannot be ascertained by only examining one cross-section, the 3Dv case at $Re_d = 800$ and 1400 seems to behave similar to the rectangular cylinder with sharp corner which is unstable to galloping.

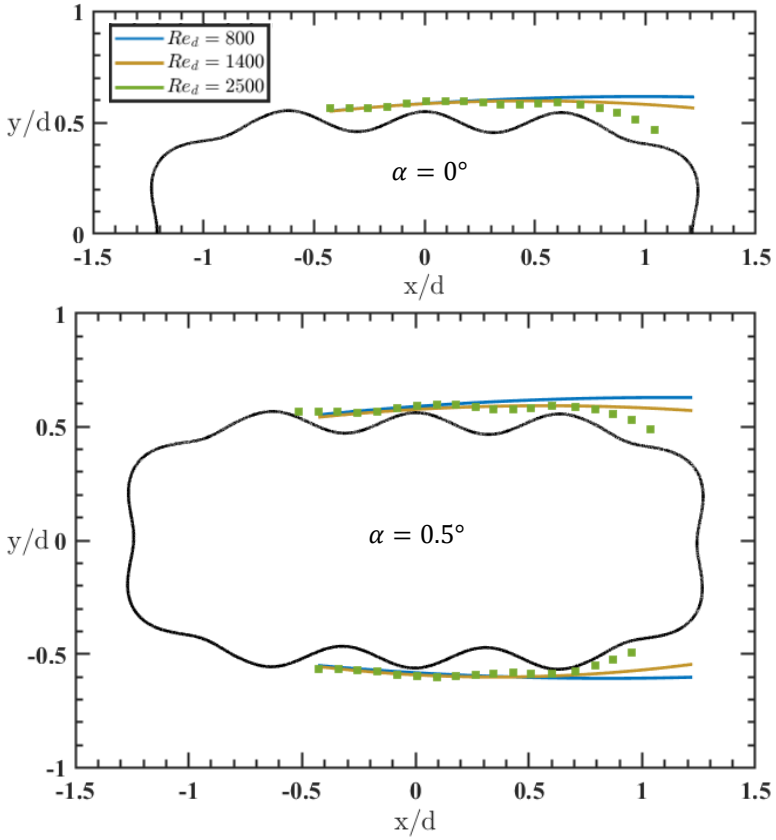

Figure 41. Comparison of the mean separation zone boundary for the 3Dv-5% cylinder at different angles of attack (different rows) and Reynolds numbers.

Figure 41 (cont'd)

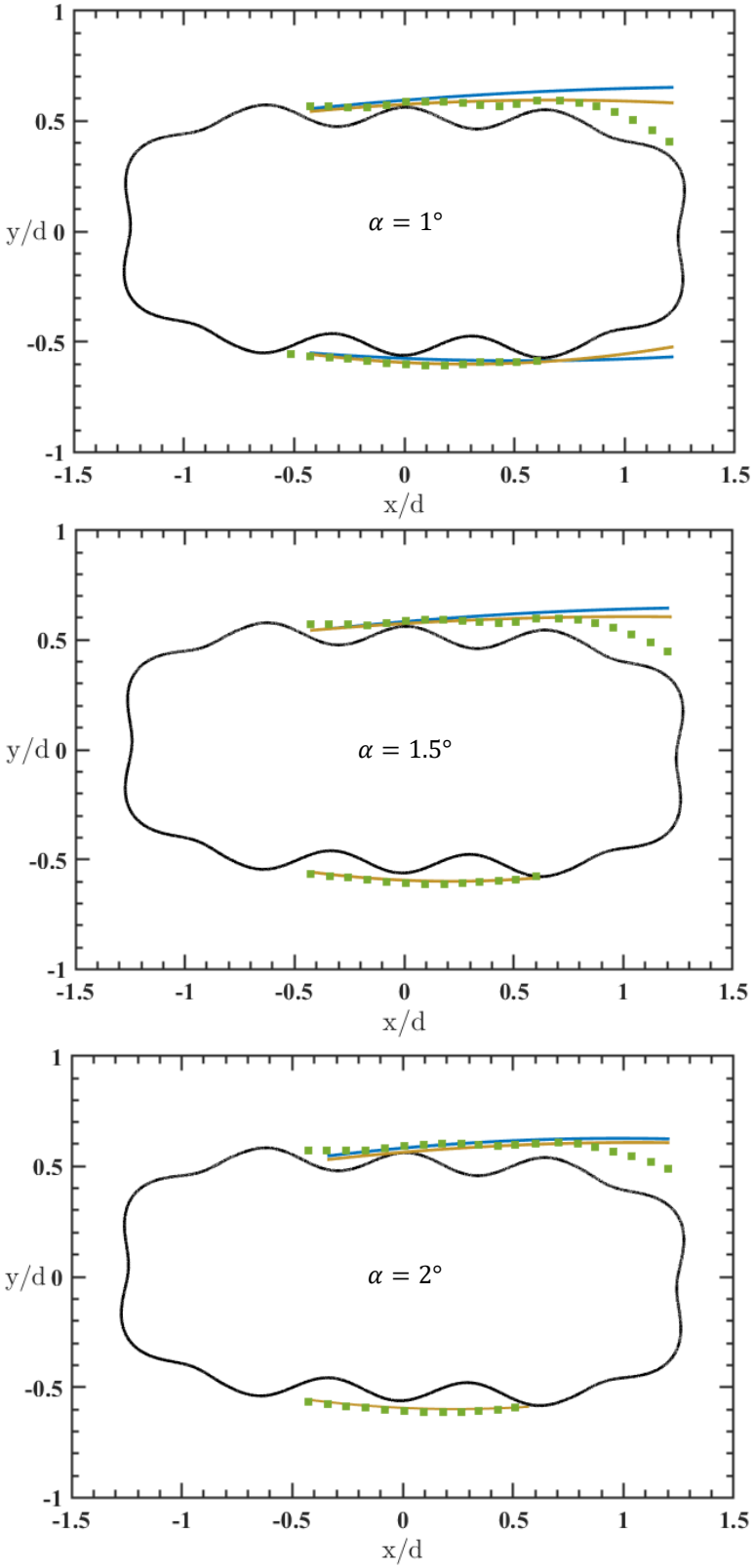

The separation zone boundary for $Re_d = 2500$ is shown using the zero-crossing data points in Figure 41, since the second order polynomial fit does not do an adequate job for this case. In fact, at $Re_d = 2500$, the separation bubble on the top surface is closed, with reattachment occurring upstream of the topology peak at the aft corner of the cylinder. Reattachment persists as the angle of attack increases to $\alpha = 1°$ with the curvature of the separation zone boundary being higher compared to the lower Reynolds numbers. This is expected to contribute to stability to galloping. In addition, reattachment to the bottom surface is promoted to a lower angle of attack $\alpha = 1°$, compared to the lower Reynolds numbers. The separation zone boundary on the bottom is generally very thin and the flow generally follows the baseline shape of the cylinder on the bottom side, which would likely lead to increased bottom surface pressure with AoA, contributing to stability to galloping. Therefore, it is expected that unlike the 2Dv geometry, increasing the Reynold number enhances the stability to galloping for the 3Dv case in the examined Reynolds number range.

To summarize, it is expected from MTV measurement on the surface of the 3Dp case, i.e. the cross-section of the 3D cylinder with a peak at the leading edge, that this case is slightly stable towards galloping at the lowest Reynolds number studied, but becomes more stable as the Reynolds number increases. For the other cross-section with a valley at the leading edge (3Dv), a positive contribution to stability to galloping is expected only at the highest Reynolds number studied. Similar trend was observed from force measurements on this cylinder in wind [7, 8] and water [11] tunnels, where the cylinder was unstable at a low enough Reynolds number, but increasing the Reynolds number was observed to improve the stability to galloping.

Although the Reynolds numbers studied here have some commonality with those studied in the wind tunnel force measurements by Feero et al. [7, 8], it is important to note that the flow

and the force characteristics in two different test facilities may be different notwithstanding matching of Re_d. Such differences may be caused by discrepancies in freestream turbulence intensity, cylinder aspect ratio, model end conditions, and test section blockage. For this reason, complementary force measurements were done by a collaborator [11] on the same cylinder models and experimental setup employed in the present study, and the results are reported in Figure 3. As seen from the figure, these results convey similar conclusion to those discussed above from characterization of the separation/reattachment characteristics of the boundary layer. Namely, the stability to galloping of the 3D cylinder improves with increasing Reynolds number.

Chapter 4. Characteristics of the Wake Flow

Whole-field 1c-MTV is carried out in the wake of the cylinders to study the effect of surface topology on the wake development and characteristics. Studying the wake is of interest for understanding the connections between the wake structures and the surface topology and, more importantly, finding the connection to the boundary layer characteristics. Secondly, for the particular application of interest for this study, the suspension cables of PADS are likely to experience interactions with the wakes of other lines based on their configuration. Therefore, studying the wake features of an isolated cylinder could help provide boundary conditions for future studies of the instability of the whole system. Furthermore, knowledge of the vortex shedding frequency in the wake of the cylinders gives insight into whether the cylinders are also susceptible to vortex-induced vibrations and the applicability of the quasi-steady analysis of galloping.

In the current study, the discussion of measurements in the wake of the cylinders at a range of Reynolds numbers, $Re_d = 800, 1100, 1400, 1800,$ and 2500, is limited to the angle of attack $\alpha = 0°$.

4.1 Mean and rms Velocity Characteristics

4.1.1 Smooth Cylinder

Color contour maps of the wake mean and rms streamwise velocity for the smooth cylinder are shown in Figure 42. The effect of Reynolds number on the recovery of the wake is evident. The mean velocity contour map on the left column suggests that at $Re_d = 800$, a small reverse flow region forms over the round corners at the cylinder aft, but does not exceed the immediate wake. Moreover, there is a forward mean flow in the near wake before a secondary reverse flow region forms farther downstream. As the Reynolds number increases, the reverse flow region at

the base extends farther downstream. The secondary reverse flow region moves upstream and extends in size, so much that at $Re_d = 1400$, the two reverse flow regions join. Further increase in Reynolds number shows a non-monotonic trend, where the reverse flow region in the wake extends both in lateral and downstream direction at $Re_d = 1800$ but shrinks distinctly at $Re_d = 2500$.

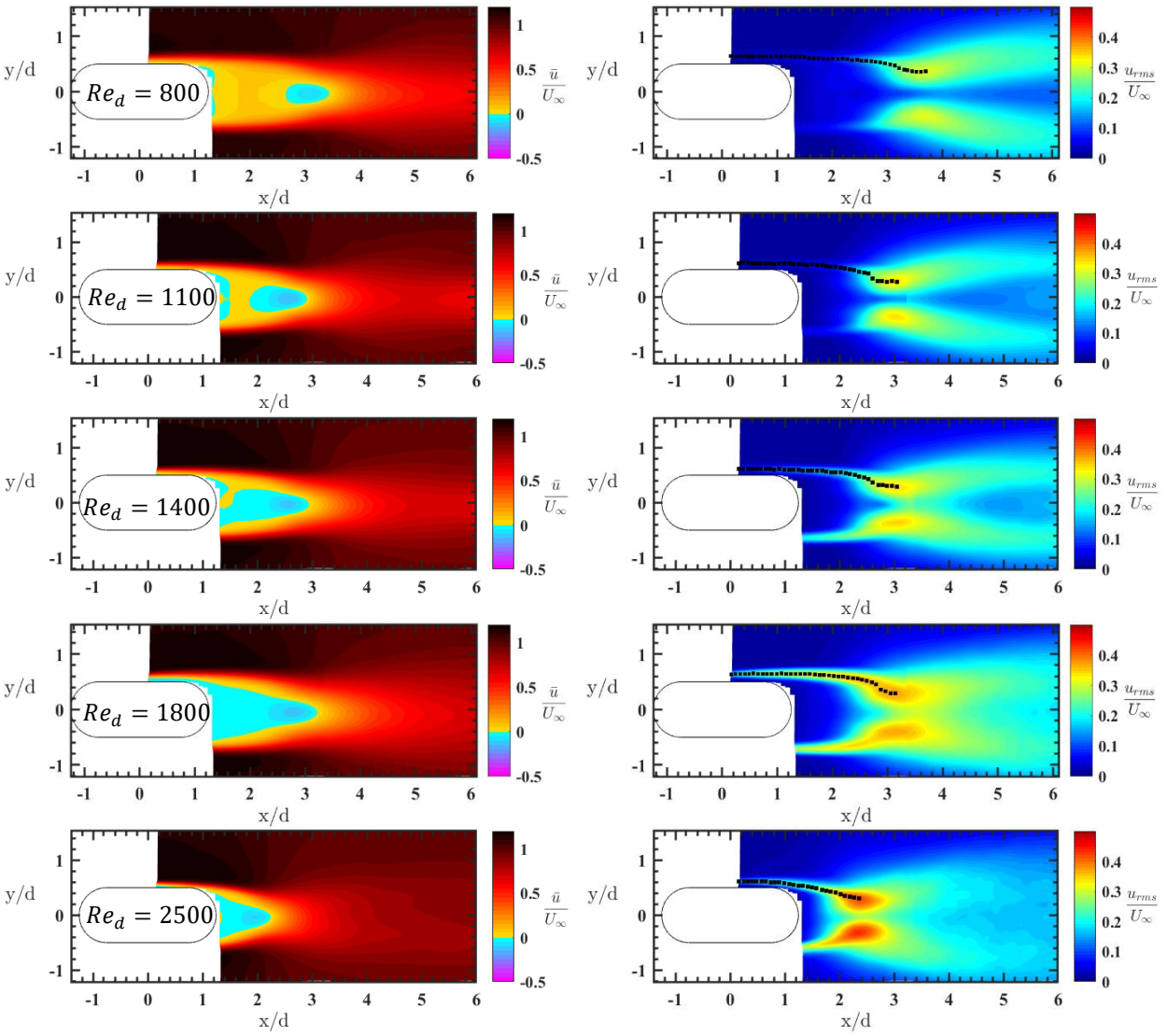

Figure 42. Color contour maps of the mean (left) and rms (right) streamwise velocity normalized by the freestream velocity ($\bar{u}/U_\infty$ and u_{rms}/U_∞, respectively) in the wake of the smooth cylinder in the Reynolds number range $Re_d = 800$-2500 in different rows. The trajectory of the peak u_{rms} in the top shear layer is marked, up to the vortex formation location (maximum u_{rms} in the wake). Flow direction is from left to right.

Although cross-stream component of the velocity is not available in the current measurements and a direct vorticity analysis cannot be accomplished, the trend observed in the current study bears some analogy to the wake flow regimes for a circular cylinder [22]. von Karman vortex street is observed at the Reynolds number range $40 < Re_d < 60 - 100$ for circular cylinders, where two flow regions with reverse flow exist: one attached to the cylinder aft surface, and the other located farther downstream in the wake where alternate vortex formation and shedding take place (Figure 43-top). As the Reynolds number increases to $60 - 100 < Re_d < 200$, the two reverse flow regions merge into one region that is attached to the aft surface. Similar behavior is observed in the current study for the smooth rectangular cylinder, where two distinct reverse flow regions are observed at $Re_d = 800 - 1100$ which, with increasing the Reynolds number to $Re_d \geq 1400$, merge into one.

The rms color maps show that the high fluctuations are generally concentrated and contained inside small regions in the immediate wake of the smooth cylinder. As the Reynolds number increases, the shear layers become more unsteady and the fluctuations in the wake intensify. The region where the maximum rms is found in the wake, which is associated with the vortex formation[23-25], moves upstream with increasing the Reynolds number from 800 to 1100, but remains relatively stationary at higher Reynolds numbers up to $Re_d = 1800$. Further increase to $Re_d = 2500$ shifts the region of highest unsteadiness farther upstream again, closer to the base of the cylinder. It is important to note here that the wake development is initiated from initial boundary layers that have steady and unsteady characteristics that could vary significantly between case. The steady boundary layer characteristics were discussed in Chapter 3, and the unsteady characteristics will be examined in Chapter 5, where it will be discussed that $Re_d \leq 1400$ exhibits wake formation from a reattached, "almost steady" boundary layer. $Re_d = 1800$

shows an unsteady transition between fully separated/reattached flow, although showing an open mean separation bubble, and reattachment of the boundary layer occurs again at $Re_d = 2500$. Although the unsteady behavior will be discussed in Chapter 5 in detail, these observations underline the complexity of the initial condition for the development of the wake and provide some context into why a non-monotonic trend is not surprising.

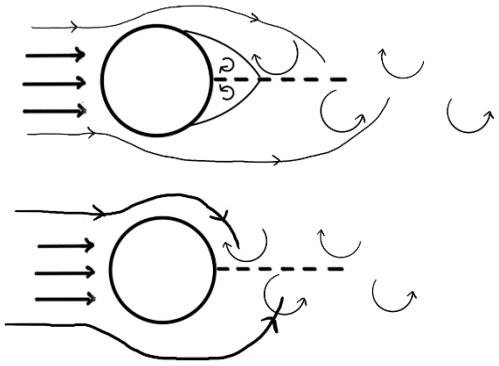

Figure 43. von Karman vortex street (top) and alternative shedding (bottom) regimes in the wake of circular cylinders, following the discussion of Panton [22].

In the near-wake, $x/d < 5$, several features may be examined: the location and the strength of the reverse flow, the wake closure length l_c (i.e., the location where $\bar{u}_c/U_\infty = 0$. See Figure 44 (top) for definition), and the "wake recovery" (the rate of increase in $\bar{u}_c/U_\infty$ downstream of the closure length). The vortex formation length definition can be seen in Figure 44 (bottom) and it is the distance between the cylinder trailing edge and the location of the peak u_{rms} in the wake. The wake mean velocity field is first characterized by examining l_c. This is accomplished by considering the streamwise evolution of the mean centerline velocity $\bar{u}_c$.

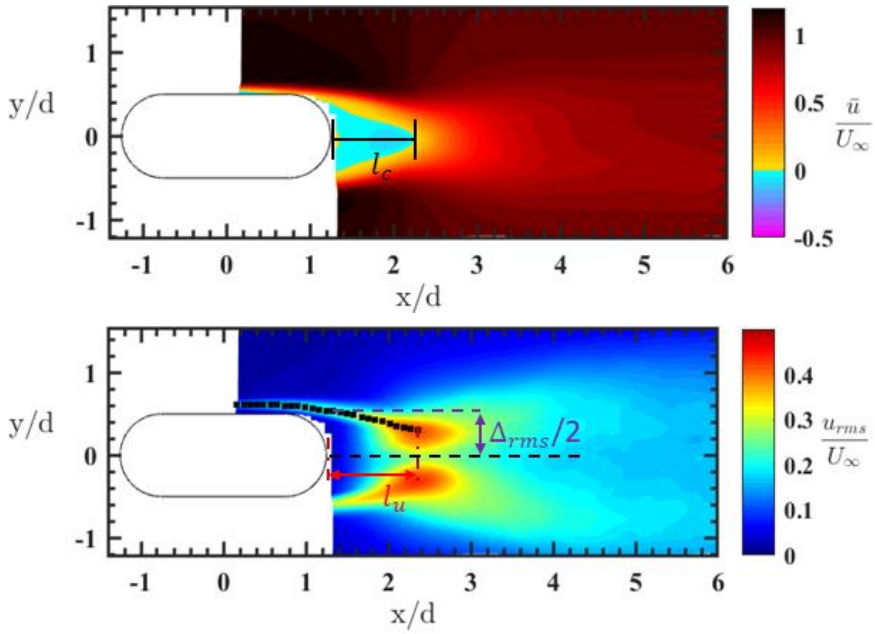

Figure 44. Definition of the closure length l_c on the mean velocity color contour map (top) as well as vortex formation length l_u and wake width Δ_{rms} on the rms velocity color contour map (bottom).

The mean centerline velocity results for the smooth cylinder are shown in Figure 45 at different Reynolds numbers. From this figure it can be seen that as the Reynolds number increases from $Re_d = 800$ to 1100, the closure length becomes shorter as the vortex formation occurs closer to the aft of the body (see Table 2 for numerical values). Further increase of the Reynolds number to $Re_d = 1400$ does not alter the closure length, but at $Re_d = 1800$ the closure length increases again. As discussed before in Chapter 3, an open boundary layer separation is observed at this Reynolds number. Therefore, it takes longer for the shear layers from the two sides of the cylinder to interact and form vortices, hence the higher l_c. At $Re_d = 2500$ reattachment of the boundary layer occurs on the surface and the closure length decreases to its lowest value. The vortex formation length is also shortest at this Reynolds number, judged by the peak u_{rms} location shown in Figure 42 (right).

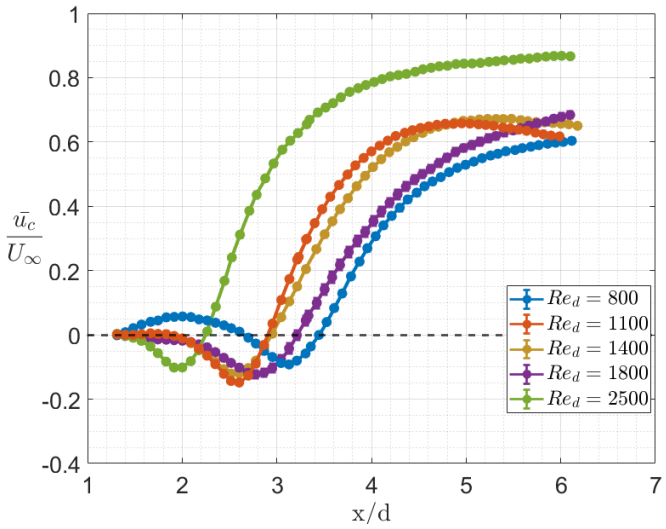

Figure 45. Comparison between the streamwise evolution of the mean centerline velocity in the wake of the smooth cylinder in the Reynolds number range $Re_d = 800 - 2500$. The error bars for most cases are smaller than the marker size.

Table 2. Summary of various wake parameters. The cases with open separation are highlighted in red, and if reattachment occurs at a higher Reynolds number, the case is highlighted in teal.

		l_c/d	l_u/d	Δ_{rms}/d	Δ_{shear}/d	St_d	$St_{\Delta_{\mathrm{rms}}}$	$St_{\Delta_{\mathrm{shear}}}$
Smooth	$Re_d = 800$	2.20	2.45	1.27	1.24	0.23	0.29	0.29
	$Re_d = 1100$	1.66	1.80	1.20	1.21	0.25	0.30	0.30
	$Re_d = 1400$	1.70	1.81	1.19	1.18	0.27	0.32	0.32
	$Re_d = 1800$	1.96	1.12	1.29	1.22	0.22	0.28	0.27
	$Re_d = 2500$	1.00	1.11	1.09	1.18	0.22	0.24	0.26
2Dp-5%	$Re_d = 800$	2.23	1.58	1.65	1.63	0.18	0.29	0.29
	$Re_d = 1100$	1.76	1.50	1.64	1.63	0.17	0.27	0.28
	$Re_d = 1400$	2.64	2.22	1.79	1.74	0.16	0.29	0.28
	$Re_d = 1800$	2.59	2.2	1.70	1.69	0.15	0.25	0.25
	$Re_d = 2500$	1.26	1.50	1.28	1.45	0.18	0.23	0.26
2Dv-5%	$Re_d = 800$	2.05	2.20	1.36	1.32	0.22	0.30	0.29
	$Re_d = 1100$	1.57	1.68	1.31	1.29	0.23	0.30	0.30
	$Re_d = 1400$	1.20	1.25	1.26	1.28	0.24	0.30	0.31
	$Re_d = 1800$	1.10	1.16	1.24	1.31	0.23	0.28	0.30
	$Re_d = 2500$	1.17	0.99	1.33	1.35	0.21	0.28	0.28
3Dp-5%	$Re_d = 800$	2.23	2.28	1.38	1.31	0.20	0.28	0.26
	$Re_d = 1100$	1.37	1.43	1.35	1.32	0.22	0.29	0.29
	$Re_d = 1400$	1.94	1.63	1.41	1.36	0.20	0.28	0.27
	$Re_d = 1800$	1.02	0.82	1.26	1.40	0.20	0.25	0.28
	$Re_d = 2500$	0.59	0.57	0.98	1.31	0.20	0.20	0.26
3Dv-5%	$Re_d = 800$	2.81	2.84	1.55	1.45	0.21	0.32	0.30

Table 2 (cont'd)

3Dv-5%	$Re_d = 1100$	1.15	1.38	1.34	1.37	0.22	0.29	0.30
	$Re_d = 1400$	0.80	0.95	1.27	1.34	0.22	0.28	0.29
	$Re_d = 1800$	0.76	0.68	1.22	1.35	0.20	0.25	0.27
	$Re_d = 2500$	0.66	0.60	1.14	1.30	0.21	0.24	0.27

Considering the reverse-flow magnitude, the maximum negative velocity slightly increases when the Reynolds number is increased from $Re_d = 800$ to 1100. Further increase to $Re_d = 1400$ causes a slight decrease in the maximum negative velocity value which remains the same at the higher Reynolds number of $Re_d = 1800$. At $Re_d = 2500$, this value slightly decreases again. Therefore, there is not an obvious trend of the maximum negative velocity with respect to Reynolds number in the examined range. The streamwise location where the maximum reverse flow velocity takes place however, follows a more familiar trend. It shifts more upstream when Reynolds number increases from $Re_d = 800$ to 1100, remains similar at $Re_d = 1400$, before moving downstream again at $Re_d = 1800$, where an open boundary layer separation is observed on the cylinder's surface. Finally, with the reattachment of the shear layer to the surface at $Re_d = 2500$, the maximum reverse flow velocity occurs more upstream and closest to the cylinder trailing edge. This trend is similar to the trend of the closure length versus Reynolds number discussed before.

Finally, the rate of centerline velocity recovery in the far wake at $Re_d = 2500$ indicates a wake closer to the asymptotic state $\bar{u}_c/U_\infty \rightarrow 1$ than the lower Reynolds numbers. It is unclear to what extent the far-field evolution might be affected by the blockage effects of the test section. This can be more extensively studied in future work.

4.1.2 2Dp-5% Cylinder

Figure 46 demonstrates the mean and rms velocity contour maps of the wake flow for the 2Dp geometry. It is evident that the reverse flow region is considerably larger compared to the smooth geometry. The size of the reverse flow region does not follow a monotonic trend against

the Reynolds number. This region shrinks when the Reynolds number increases from $Re_d = 800$ to 1100, but expands again at $Re_d = 1400$ and 1800. Increasing the Reynolds number further to $Re_d = 2500$ shows a considerable reduction in the size of the reverse flow region, so much that it is the smallest amongst the studied range of Reynolds numbers. As it was seen in Chapter 3, the separated shear layer reattaches to the surface of this cylinder *only* at $Re_d = 2500$.

The rms velocity contour maps depicted in the right column of Figure 46 show that the region containing the high fluctuations occupies a region that is elongated more in the streamwise direction compared to the smooth cylinder. This elongation in the streamwise direction is more pronounced as the Reynolds number increases. The rms contour maps also suggest a non-monotonic behavior of the unsteadiness intensity with respect to Reynolds number. The unsteadiness in the wake intensifies as the Reynolds number increases from $Re_d = 800$ before the trend reverses at $Re_d = 1800$. In fact, the lowest maximum normalized fluctuations are observed at $Re_d = 2500$. This case involves formation of vortex structures from instability of the separated shear layer above the cylinder side surface, which will be later discussed in Chapter 5 (see Figure 65).

The mean wake flow field of the 2Dp cylinder differs from the smooth cases as it does not exhibit two separated reverse flow regions. It is possible that this occurs at a lower Reynolds number, but the current study does not provide sufficient data for a conclusive determination.

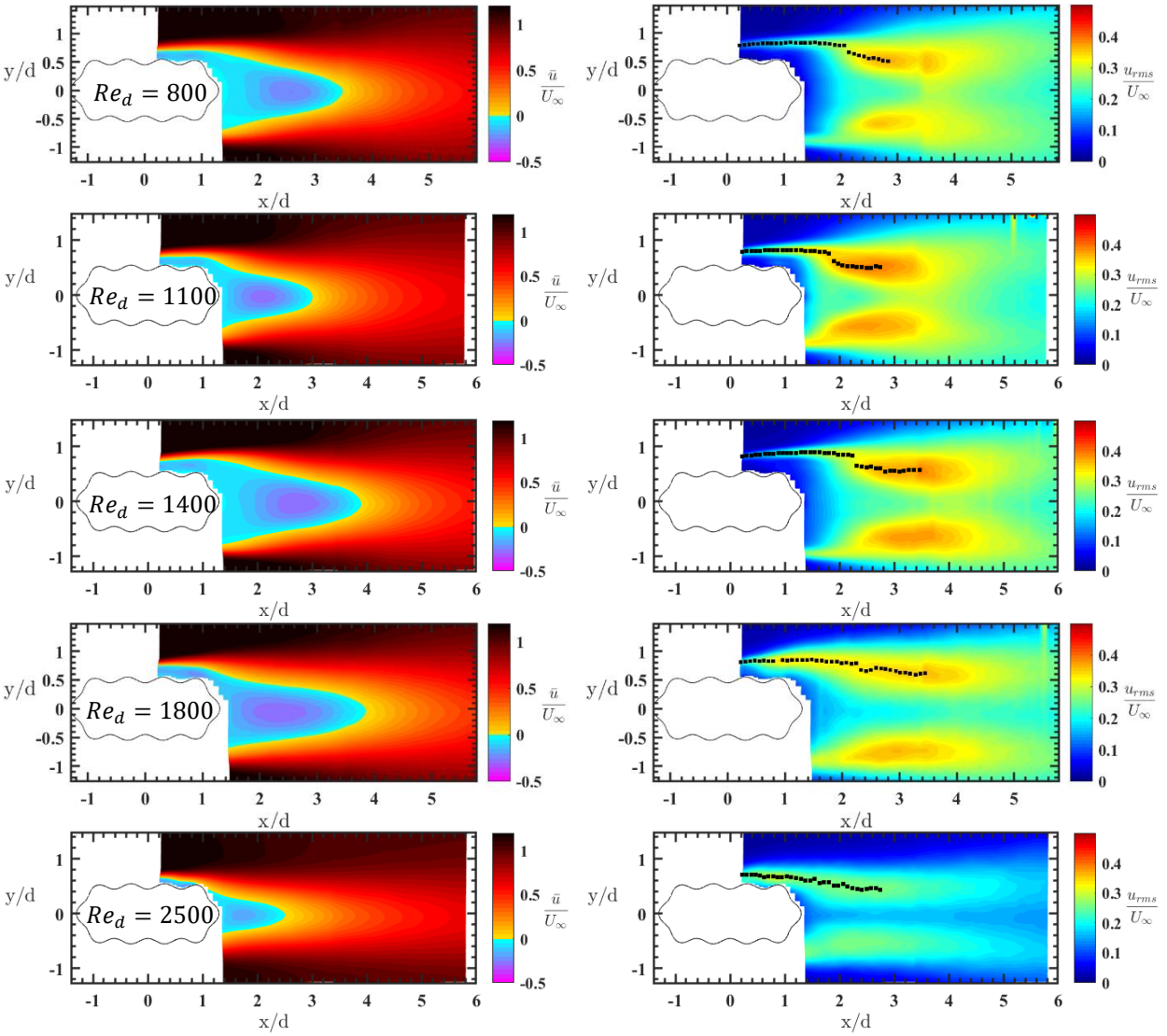

Figure 46. Color contour maps of the mean (left) and rms (right) streamwise velocity normalized by the freestream velocity ($\bar{u}/U_\infty$ and u_{rms}/U_∞, respectively) in the wake of the 2Dp-5% cylinder in the Reynolds number range $Re_d = 800$-2500 in different rows. The trajectory of the peak u_{rms} in the top shear layer is marked, up to the vortex formation length. Flow direction is from left to right.

Figure 47 presents the mean centerline velocity in the wake of the 2Dp cylinder at different Reynolds numbers. The closure length decreases with increasing the Reynolds number from $Re_d = 800$ to 1100, but reverts trend and increases at $Re_d = 1400$. It remains very similar at $Re_d = 1800$, but shrinks considerably as the separated shear layer reattaches to the surface at

$Re_d = 2500$. This non-monotonic trend of l_c versus Reynolds number is similar to the smooth cylinder case (see Table 2 for numerical values).

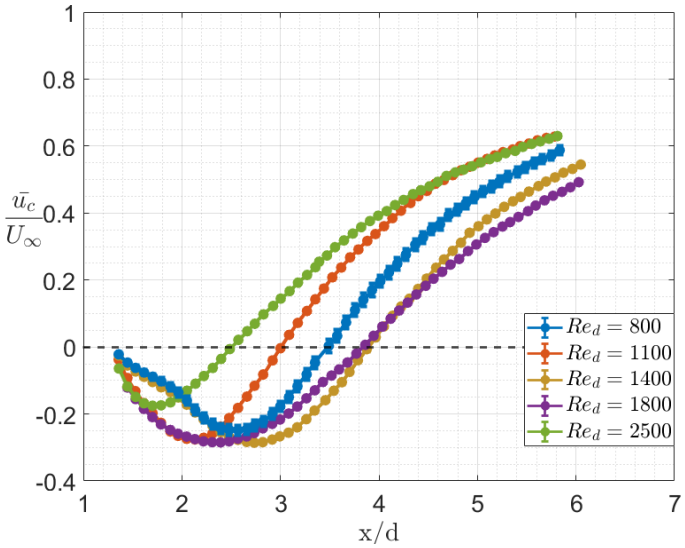

Figure 47. Comparison between the streamwise evolution of the mean centerline velocity in the wake of the 2Dp cylinder in the Reynolds number range $Re_d = 800 - 2500$. The error bars for most cases are smaller than the marker size.

The maximum reverse flow velocity slightly increases from $Re_d = 800$ to 1100, but remains fairly similar with further increasing the Reynolds number, before a distinct decrease occurs at $Re_d = 2500$. This decrease can be associated with the reattachment of the separated shear layer to the surface of the cylinder at $Re_d = 2500$, unlike all the other studied Reynolds numbers. The location of the maximum reverse flow velocity follows a more similar trend to the closure length versus Reynolds number. It first moves upstream up to $Re_d = 1100$, reverts direction and moves away from the cylinder towards downstream at $Re_d = 1400$, and reverts direction for a second time to move closer to the cylinder with further increasing the Reynolds number.

The rate of centerline velocity recovery in the far wake of this cylinder shows a similar trend at all Reynolds numbers which is considerably deviated from an asymptotic state $\bar{u}_c/U_\infty \rightarrow 1$. In fact, unlike the case of the smooth cylinder, reattachment of the separated shear layer to the

surface at $Re_d = 2500$ does not improve the wake recovery towards the asymptotic state. The results also show that for this cylinder the wake recovery is noticeably slower than the smooth cylinder.

4.1.3 2Dv-5% Cylinder

The mean and rms velocity color contour maps in the wake of the 2Dv cylinder are shown in Figure 48. Overall, this cylinder has a closer behavior to the smooth cylinder. At $Re_d = 1100$, the mean velocity colormap suggests that there are two separate reverse flow regions in the near wake, and that the vortex formation region is farther downstream and not yet merged with the reverse flow region over the trailing edge. At $Re_d = 800$, the same observation holds true, with the exception that the reverse flow region connected to the surface is not observed. This absence is attributed to the measurement limitations in close proximity to the aft surface and inside the respective topology valley. Vortex formation region keeps moving closer to the trailing edge as the Reynolds number increases to $Re_d = 1800$, and is merged with the near trailing edge reverse flow region starting at $Re_d = 1400$. At $Re_d = 2500$, the reverse flow region grows compared to the lower Reynolds numbers, which is the opposite trend observed at the lower Reynolds numbers. It is noteworthy to recall from Chapter 3 that an open separation bubble is observed over the surface of this cylinder only at $Re_d = 1800$ and 2500, where the separation zone boundary remains very close to the surface at the former Reynolds number and moves farther from the surface at the latter. Therefore, a systematic trend is seen in the size of the reverse flow region, until the full opening up of the separation bubble.

The rms contour maps on the right column of Figure 48 reveal that the flow in the immediate wake is quiet at $Re_d = 800$. In other words, the rapid expansion of the region with high unsteadiness, which is associated with the vortex roll-up, takes place after about 1.5 diameters

downstream of the trailing edge. As the Reynolds number increases, the high unsteadiness region moves closer to the cylinder's base, which agrees with the postulation that the vortex formation region merges with the reverse flow region at the trailing surface starting at $Re_d = 1400$.

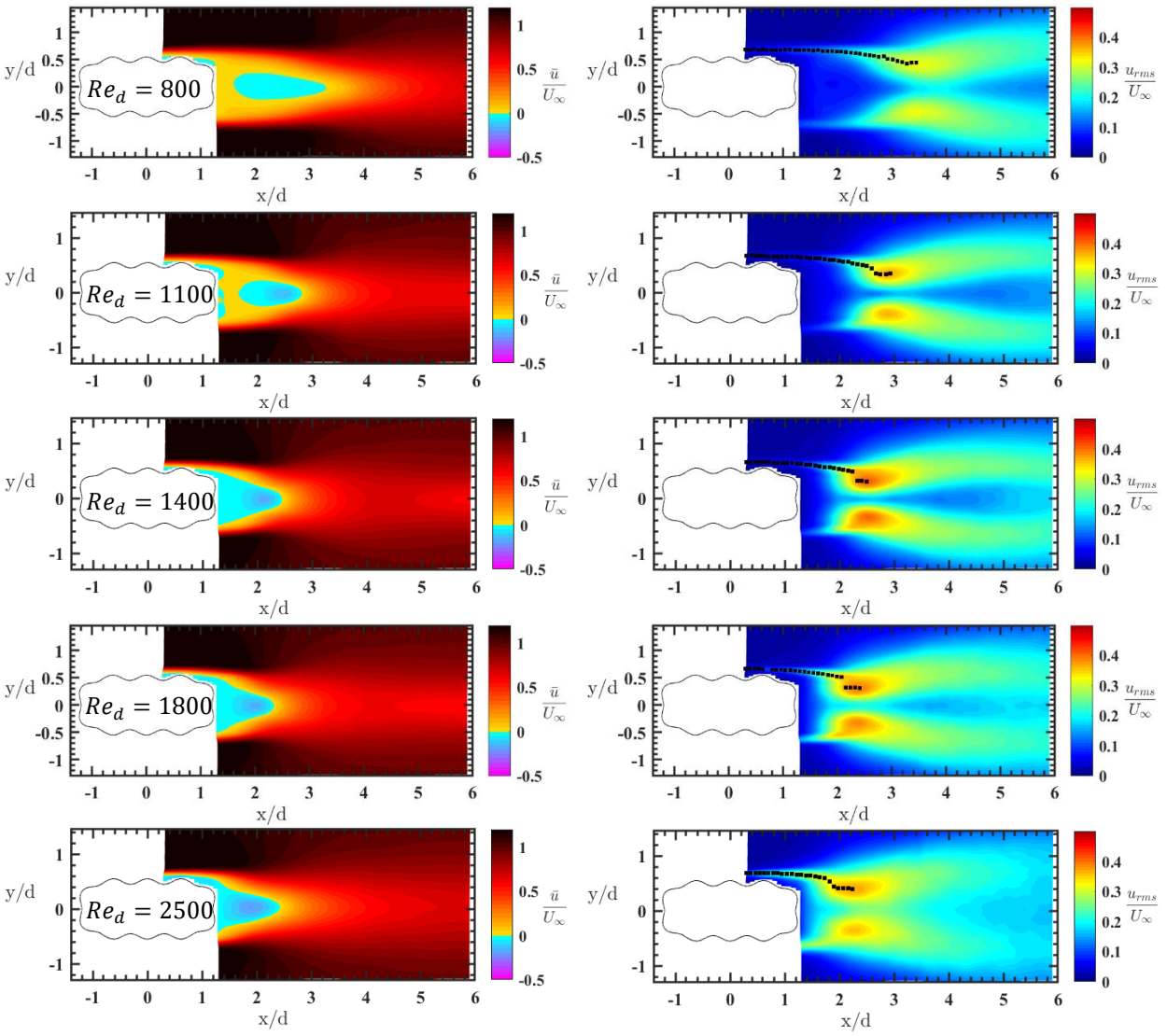

Figure 48. Color contour maps of the mean (left) and rms (right) streamwise velocity normalized by the freestream velocity ($\bar{u}/U_\infty$ and u_{rms}/U_∞, respectively) in the wake of the 2Dv-5% cylinder in the Reynolds number range $Re_d = 800$-2500 in different rows. The trajectory of the peak u_{rms} in the top shear layer is marked, up to the vortex formation length. Flow direction is from left to right.

The highly unsteady region is confined in its streamwise extent, similar to the smooth cylinder, and the unsteadiness intensifies with the Reynolds number up to $Re_d = 1400$. Increasing the

Reynolds number further is linked with a reverse trend, where the maximum unsteadiness level decays in the wake.

Mean centerline velocity in the wake of the 2Dv cylinder is plotted in Figure 49. The vortex closure length keeps decreasing when Reynolds number increases from $Re_d = 800$ to 1800, but slightly increases again at $Re_d = 2500$. From Chapter 3, the separated shear layer reattaches to the surface at lower Reynolds numbers and becomes fully open at $Re_d = 2500$, which explains the change of trend for the l_c versus Re_d (see Table 2 for numerical values). The maximum reverse flow velocity keeps monotonically increasing with Reynolds number which is a different behavior seen from smooth and 2Dp cylinders. The location of the maximum reverse flow velocity shows a similar trend and monotonically moves upstream and closer to the cylinder with increasing Reynolds number.

The rate of centerline velocity recovery in the far wake of this cylinder shows a good deviation from an asymptotic state $\bar{u}_c/U_\infty \to 1$, where the recovery does not exceed about 70%. In this case, opening of the separation bubble on the surface at $Re_d = 2500$ does not deteriorate the wake condition away from an asymptotic state. Although not shown here directly, the rate of wake recovery for this case at all Reynolds numbers except $Re_d = 2500$ is comparable to the smooth cylinder. At $Re_d = 2500$, the recovery of the wake is slower for the 2Dv cylinder compared to the smooth cylinder.

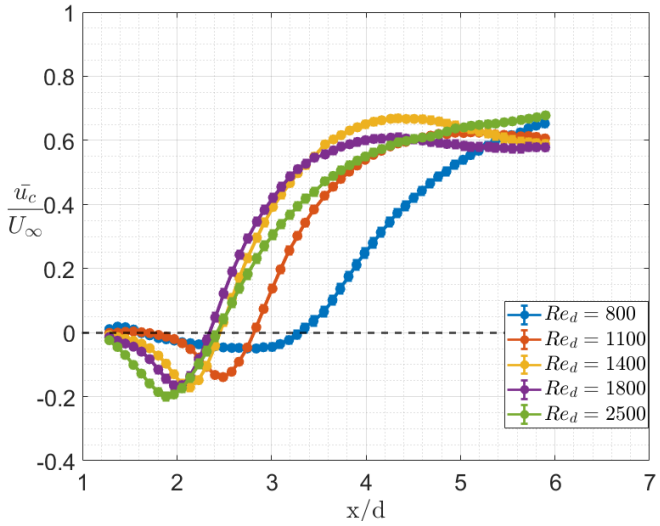

Figure 49. Comparison between the streamwise evolution of the mean centerline velocity in the wake of the 2Dv cylinder at the Reynolds number range $Re_d = 800 - 2500$. The error bars for most cases are smaller than the marker size.

4.1.4 3Dp-5% Cylinder

Mean and rms velocity color contour maps are presented in Figure 50 for the wake of the cylinder with the three-dimensional geometry and in the plane of the cross-section with a peak at the leading edge (3Dp). At the lowest Reynolds number $Re_d = 800$, the mean contour map suggests that there is a confined and isolated reverse flow region in the wake which is not attached to the trailing end of the cylinder, and that vortex formation region is separated from the reverse flow region at the aft of the body. Interestingly, this behavior is very different than the 2D counterpart, where the latter had an open separation bubble over the surface, translating into a large reverse flow region in the wake. As the Reynolds number increases to $Re_d = 1100$, the secondary reverse flow region merges with the reverse flow zone at the aft of the body to form a single reverse flow region. The size of this region peaks at $Re_d = 1400$, before starting to shrink again at higher Reynolds numbers.

The rms velocity contour maps for $Re_d = 800$ on the right column of Figure 50 show the shear layers with higher unsteadiness level start rolling up (expansion of the high rms region) at

about $x/d \approx 2.75$, and that vortex formation takes place relatively far from the tailing base of the cylinder. As the Reynolds number increases, the widening of the region with high rms velocity progresses towards upstream and closer to the cylinder's base. Compared to the 2D counterpart, this case shows the high unsteady region is more confined, especially at $Re_d = 2500$.

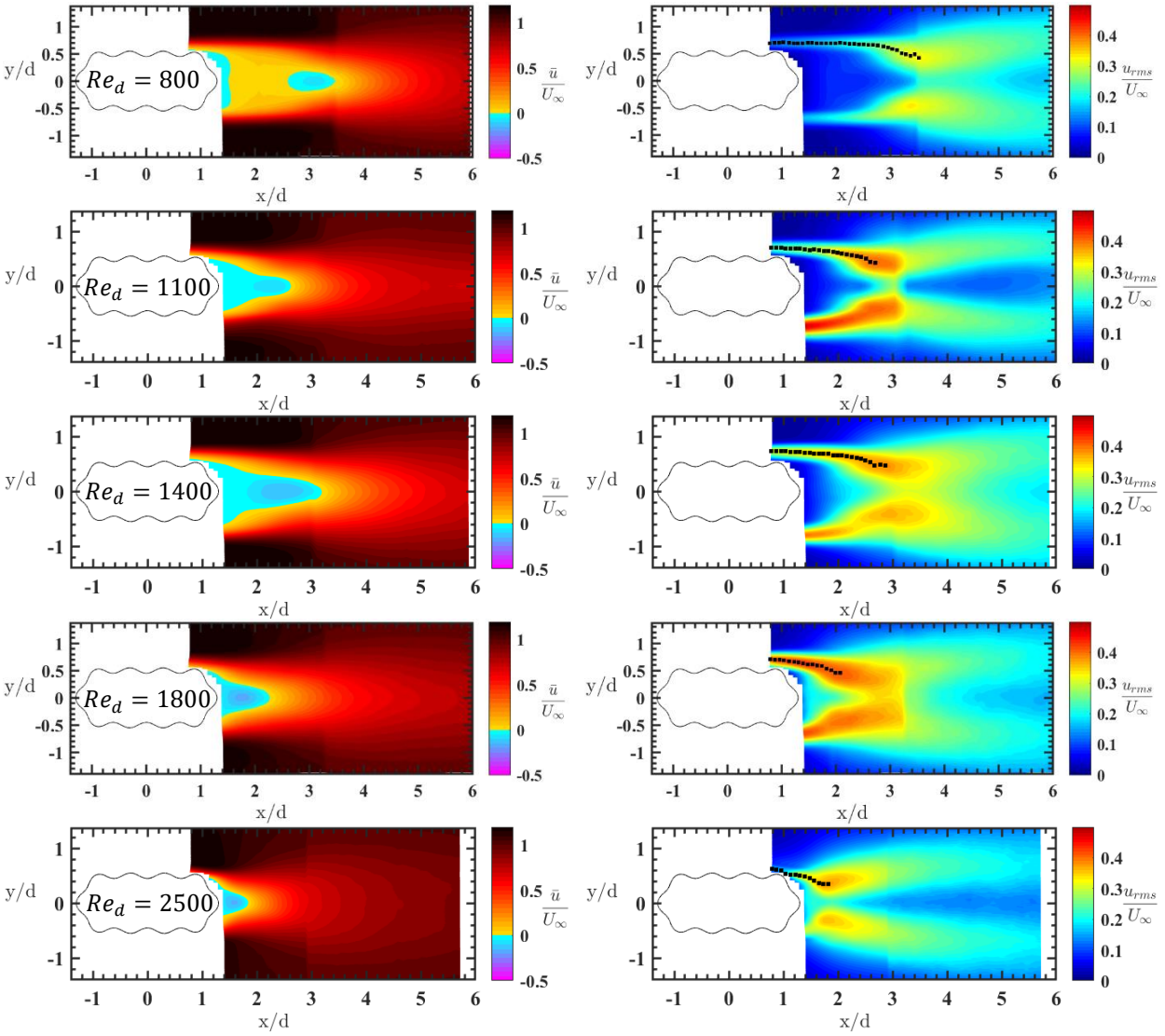

Figure 50. Color contour maps of the mean (left) and rms (right) streamwise velocity normalized by the freestream velocity ($\bar{u}/U_\infty$ and u_{rms}/U_∞, respectively) in the wake of the 3Dp-5% cylinder in the Reynolds number range $Re_d = 800$-2500 in different rows. The trajectory of the peak u_{rms} in the top shear layer is marked, up to the vortex formation length. Flow direction is from left to right.

Mean centerline velocity in the wake of the 3Dp cylinder shown in Figure 51 suggests that closure length trend with Reynolds number flip-flops twice in the range of study. Specifically, l_c first decreases when Re_d is increased from 800 to 1100, then increases at $Re_d = 1400$, before starting to decrease again at higher Reynolds numbers (see Table 2 for numerical values). This is similar to the l_c-Re_d trend of the 2D counterpart.

The maximum reverse flow velocity increases with increasing the Reynolds number up to $Re_d = 1800$ and remains similar within the errorbars at the higher Reynolds number. The location of the maximum reverse flow velocity, however, follows a more similar trend to closure length. It moves upstream with increasing the Reynolds number with an exception of $Re_d = 1400$ case, where it occurs farther downstream. The 2Dp cylinder also showed a similar trend.

The rate of centerline velocity recovery in the far wake of this cylinder shows a closer trend to an asymptotic state $\bar{u}_c/U_\infty \to 1$ at $Re_d = 2500$. The recovery at lower Reynolds numbers is also better compared to the 2D counterpart. Although not shown here directly, but the streamwise evolution of $\bar{u}_c$ after the wake closure for this case, at all Reynolds numbers except $Re_d = 2500$, is lower than the smooth cylinder. At $Re_d = 2500$, this evolution is very similar to the smooth case.

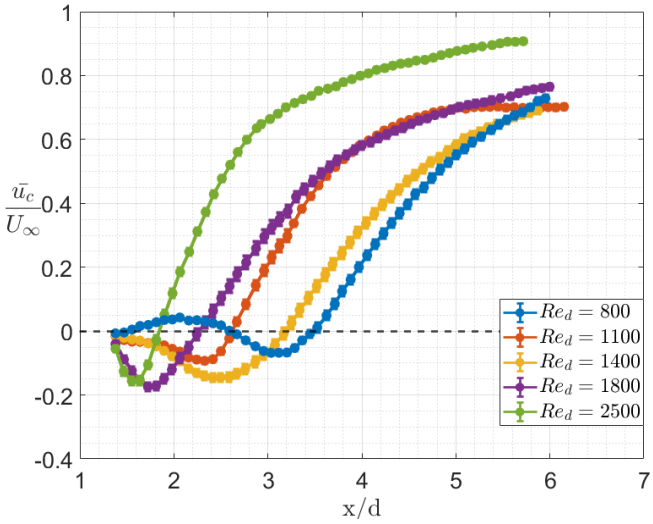

Figure 51. Comparison between the streamwise evolution of the mean centerline velocity in the wake of the 3Dp cylinder at the Reynolds number range $Re_d = 800 - 2500$. The error bars for most cases are smaller than the marker size.

4.1.5 3Dv-5% Cylinder

Figure 52 shows the mean and rms velocity contour maps in the wake of the other cross-section of the three-dimensional geometry, the 3Dv case. The mean velocity contour map at $Re_d = 800$ suggests the vortex formation region is separated from the reverse flow region attached to the trailing edge, which was also observed for the 3Dp case. However, the latter reverse flow region stretches farther downstream from the cylinder's base. This is also true for the secondary reverse flow region associated with the vortex formation region. At higher Reynolds numbers, the two reverse flow regions join together and there is a single reverse flow zone. Increasing the Reynolds number also results in a monotonic decrease in the size of this reverse flow region. This monotonicity was not observed for any other case.

The rms velocity contour maps in Figure 52 show a relatively confined region of high unsteadiness, after a rapid widening of the shear layer. As the Reynolds number increases, the widening of the shear layer monotonically shifts closer to the trailing base of the cylinder.

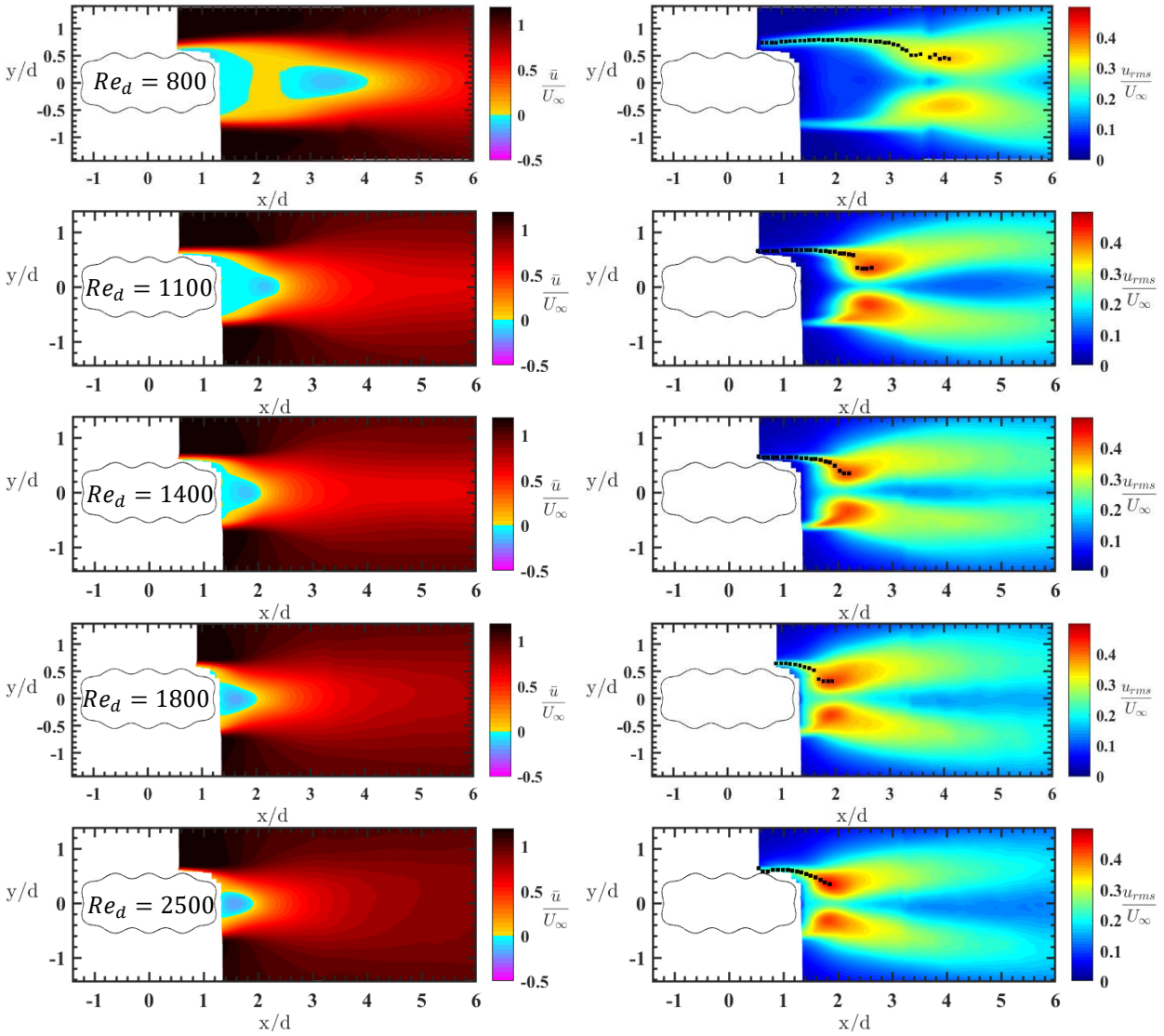

Figure 52. Color contour maps of the mean (left) and rms (right) streamwise velocity normalized by the freestream velocity ($\bar{u}/U_\infty$ and u_{rms}/U_∞, respectively) in the wake of the 3Dv-5% cylinder in the Reynolds number range $Re_d = 800$-2500 in different rows. The trajectory of the peak u_{rms} in the top shear layer is marked, up to the vortex formation length. Flow direction is from left to right.

Mean centerline velocity in the wake of the 3Dv cylinder is presented in Figure 53 and shows a monotonic decrease of closure length with increasing the Reynolds number (see Table 2 for numerical values). The maximum reverse flow velocity remains constant within the error bars from $Re_d = 800 - 1400$ and starts increasing as the Reynolds number further increases. The location of the maximum reverse flow velocity is shifted upstream in a monotonic fashion with

increasing the Reynolds number. In general, both the 2D and 3D geometries with a valley at the leading edge generally seem to show a more systematic trend of the reverse flow shrinkage with increase of the Reynolds number.

As the Reynolds number increases, the rate of centerline velocity recovery in the far wake of this cylinder becomes closer to an asymptotic state. The recovery at lower Reynolds number range $Re_d = 800 - 1400$ is comparable to the 2D counterpart, but the variation of surface topology along the span improves the recovery at the higher Reynolds numbers. In addition, the streamwise evolution of $\bar{u}_c$ after the wake closure is generally faster at higher Reynolds numbers.

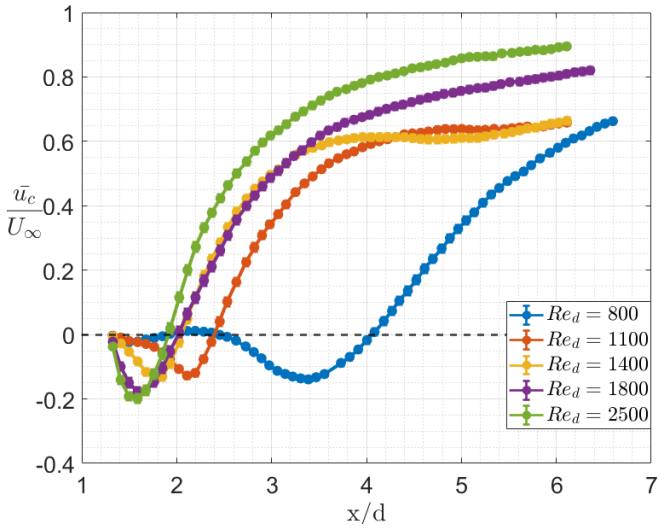

Figure 53. Comparison between the streamwise evolution of the mean centerline velocity in the wake of the 3Dv cylinder at the Reynolds number range $Re_d = 800 - 2500$. The error bars for most cases are smaller than the marker size.

4.1.6 Discussion

Within this subsection, a comparison and discussion will be conducted on the results that have been presented in sections 4.1.1 through 4.1.5. The streamwise evolution of the mean centerline velocity and the mean separation zone boundary for different cylinders discussed before are summarized here in Figure 54 and Figure 55. It can be seen that, except for $Re_d = 800$, the presence of a topology peak at the leading edge of the 2D geometry overall increases the closure

length. The effect of surface topology on the wake closure length is more appreciable at the intermediate Reynolds numbers 1400 and 1800. Based on the boundary layer measurements in Chapter 3 summarized in Figure 55, what is distinct about the 2Dp geometry is that the separation zone is laterally larger compared to the other geometries, with the exception of $Re_d = 2500$. This is consistent with the clear difference in the development of $\bar{u}_c/U_\infty$ for this geometry. In this case, the recovery of the mean centerline velocity downstream of the closure length is slower. Some cases of the geometries with a valley at the leading edge have also shown open separation bubbles over the surface in Chapter 3 (2Dv at $Re_d = 2500$ and 3Dv at all Reynolds numbers), but for these cases, the shear layer becomes very close to reattaching. It is believed that thanks to this, the development of the centerline mean velocity does not vary significantly from that of the geometries with attached flow and with a closed separation bubble on the surface, such as the smooth cylinder. Therefore, it indicates that the wake behavior is not substantially altered solely by the presence of open or closed separation, but rather the size of the separation zone and the proximity of the shear layer to the cylinder surface emerge as critical factors affecting the wake behavior. Moreover, when considering the 3Dv cases, it should be considered that the separation bubble is closed at the other spanwise cross-section corresponding to 3Dp at all Reynolds numbers, therefore the separation bubble is not open along the entire span of the cylinder.

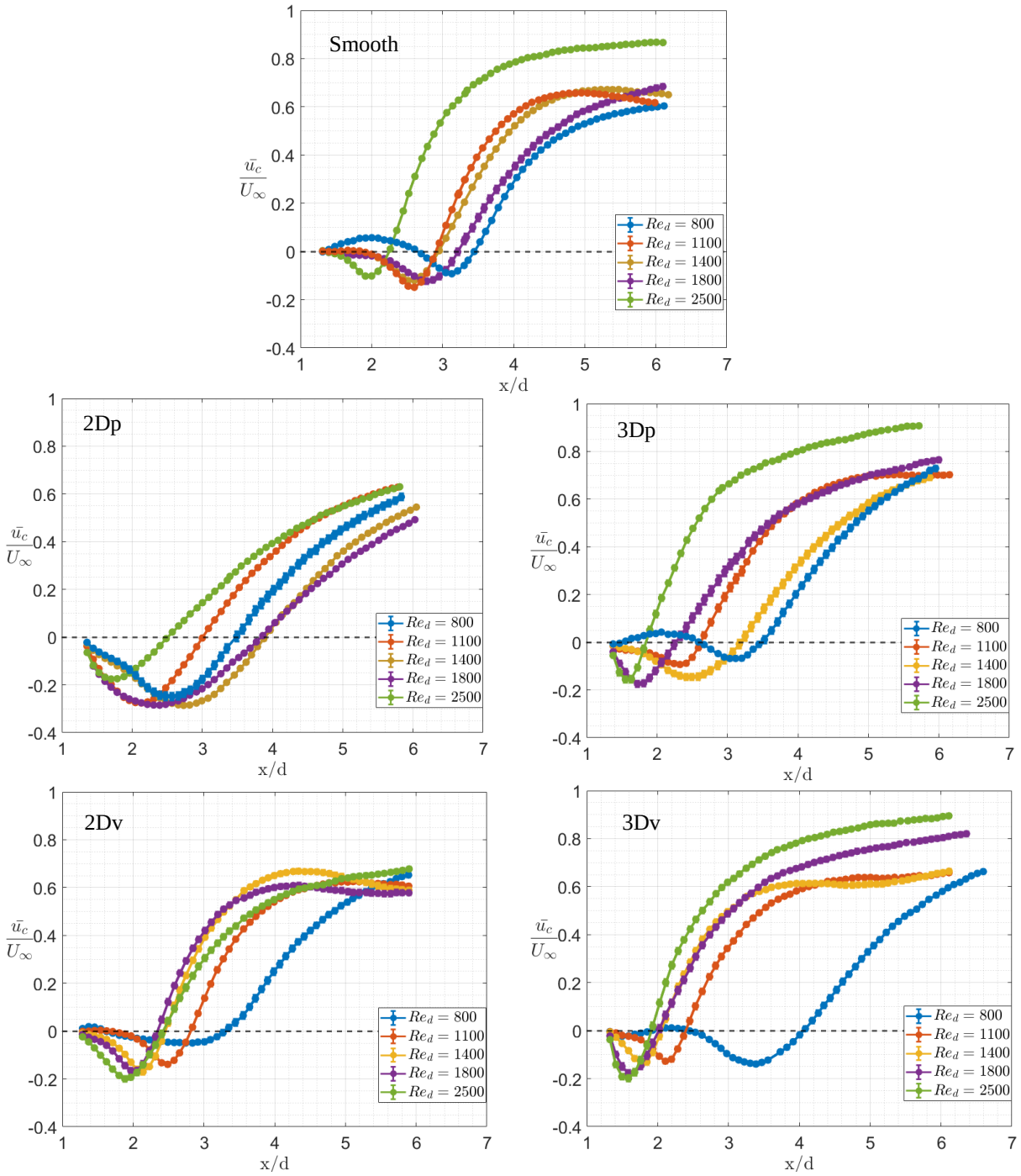

Figure 54. Collection of the streamwise evolution of the mean centerline velocity in the wake of different cylinders in the Reynolds number range $Re_d = 800 - 2500$. The error bars for most cases are smaller than the marker size.

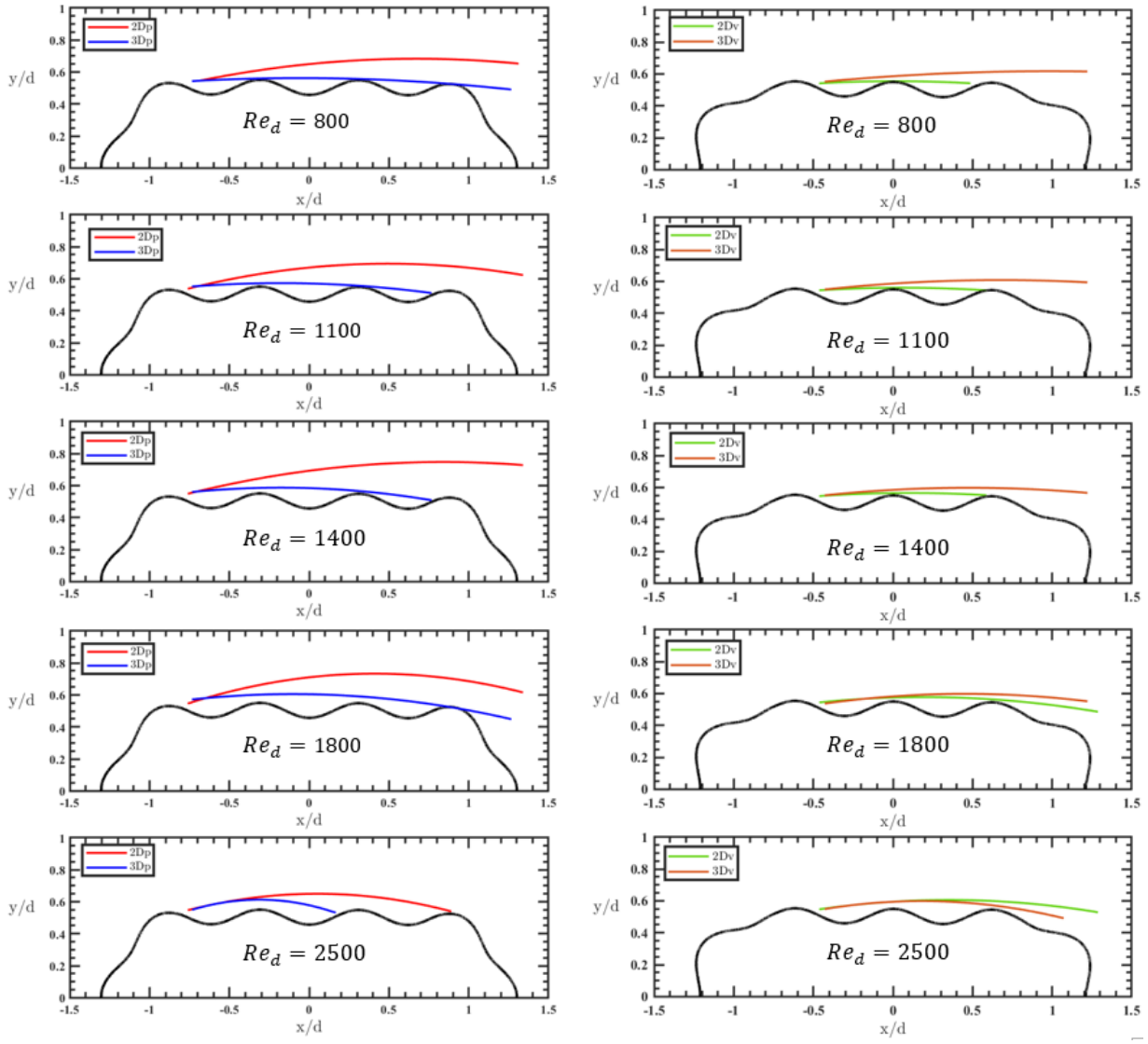

Figure 55. Comparison of the mean separation zone boundary for the cylinders with a peak (left) and a valley (right) at the leading edge at different Reynolds numbers. Flow is from left to right.

Interestingly, the two cross-sections of the 3D geometry show similar trends with the Reynolds number to their 2D counterparts. Overall, the geometries with a peak at the leading edge first show a decrease in l_c at $Re = 1100$, followed by an increase at $Re_d = 1400$, and another subsequent decrease with further increasing the Reynolds number. While the geometries with a valley at the leading edge show a consistent reduction in the closure length as the Reynolds number increases, indicating a faster early development of the wake. The only anomaly in this trend is the 2Dv at the highest Reynolds number, which was seen to have an open boundary layer separation

in Chapter 3. The smooth cylinder follows a similar trend to 2Dp, where increasing the Reynolds number causes l_c to decreases twice at $Re_d = 1100$ and 2500. In addition, for both peak and valley geometries, the presence of the topology variation along the span decreases the closure length at all Reynolds numbers, with the exception of the valley configurations at $Re_d = 800$. In this case, l_c is smaller for the 2D geometry in the absence of the variation along the span.

Considering the reverse-flow magnitude, the maximum negative velocity is nearly the same for the smooth cylinder and keeps increasing with the Reynolds number within the data scatter for the other geometries. The only exception is the 2Dp cylinder, showing a decrease in the maximum negative velocity at $Re_d = 2500$. For this case, flow reattaches to the surface which does not happen at lower Reynolds numbers.

The vortex formation length, l_u, for the smooth cylinder exhibits a consistent monotonic decrease, considering the measurement uncertainty, as the Reynolds number increases. This trend is also observed in geometries with a topology valley at the leading edge. However, for geometries with a topology peak at the leading edge, specifically 2Dp at $Re_d = 1400$ and 1800, and 3Dp at $Re_d = 1400$, higher l_u values are evident at the intermediate Reynolds numbers. Furthermore, among all cases at $Re_d \geq 1400$, 2Dp displays the highest l_u value. It is worth noting that the presence of surface topology variation along the span appears to increase l_u at the lowest Reynolds number, when compared to the 2D counterparts, but this trend reverses at $Re_d \geq 1100$.

Finally, the rate of centerline velocity recovery in the far wake for the smooth cylinder and that with 3D topology at $Re_d = 2500$ indicate very similar behaviors and a wake closer to the asymptotic state $\bar{u}_c/U_\infty \to 1$ than the cylinders with 2D topology. In addition, the streamwise evolution of $\bar{u}_c$ for 3D case at this Reynolds number is very close to the smooth cylinder, which is not the case for the 2D topology. Overall, variation of the surface topology along the span improves

the wake recovery closer to the asymptotic state, compared to the 2D counterparts. It is unclear to what extent the far-field evolution might be affected by the blockage effects of the test section. This can be more extensively studied in future work.

In summary, the data obtained from this study reveals that surface topology can introduce minor or significant variations not only in the quantitative but also in the qualitative behavior of the boundary layer and wake. However, the extent of these variations depends on the specific characteristics of the topology. For instance, when comparing 2Dv and 2Dp with the same amplitude and wavelength but different "phase" topology, significantly different behaviors are observed in the boundary layer and wake. It becomes apparent that predicting the behavior of intermediate phases or other wavelengths, let alone more generalized topology, is challenging based solely on the current data.

4.2 Vortex Shedding Frequency

To measure the vortex shedding frequency, power spectral density (PSD) results are obtained for the fluctuating velocity reported at the cross-stream location showing the highest u_{rms} across the wake far downstream, at $x/d \approx 5.8$. The results are depicted in Figure 56 plotted against the Strouhal number, $St_d = fd/U_\infty$, based on the baseline width of the cylinder, where the St_d uncertainty is ± 0.002. Evidence of vortex shedding can be found from the presence of spectral peaks in the power spectral density (additional evidence based on phase-averaged velocity results will be shown in Chapter 5). Specifically, a clear peak in the spectrum is found for all cases, although the peaks are weaker for some cases. St_d shows a non-monotonic behavior for the smooth cylinder, where it increases with Reynolds number up to $Re_d = 1400$, before it possesses a lower but constant value at higher Reynolds numbers (see Table 2 for numerical values). It was previously observed that the boundary layer is attached in the $800 - 1400$ Reynolds number

range. At $Re_d = 1800$, the peak is less prominent and distributed over a wider band, and this case showed an open boundary layer separation. At $Re_d = 2500$, which showed a reattached boundary layer, the peak regains prominence and becomes narrower.

The 2Dp cylinder shows hardly prominent PSD peaks, and those observed are distributed over a wider band compared to the other geometries at the studied Reynolds numbers. The Strouhal number associated with the vortex shedding is reduced with increasing the Reynolds number up to $Re_d = 1800$, but recovers at $Re_d = 2500$. In Figure 56, it is challenging to distinguish a PSD peak for this geometry at $Re_d = 1800$, and the shedding Strouhal number is here determined at the location of the maximum PSD value. As discussed before, the boundary layer remains separated over the surface of this cylinder at the former Reynolds number range and reattaches at $Re_d = 2500$. Overall, St_d is the lowest for the 2Dp cylinder at all Reynolds numbers. It is noteworthy to mention that a distinctive characteristic of this case is the location of the separation zone boundary, which is farthest from the surface, as observed in Chapter 3.

The 2Dv cylinder shows prominent peaks distributed over a narrow band at all Reynolds numbers, although this prominence starts decaying after $Re_d = 1800$. St_d also increases with increasing the Reynolds numbers up to $Re_d = 1400$, but starts decreasing as the Reynolds number further increases. The boundary layer over the 2Dv cylinder, as discussed in Chapter 3, was seen to reattach to the surface at Reynolds numbers $Re_d = 800 - 1400$, but failed to do so at higher Reynolds numbers and the separation zone boundary became farther from the surface.

St_d is equal for the two cross-sections of the 3D cylinder within the uncertainty, where both show equal strength and narrower peaks at the higher Reynolds number. $Re_d = 1400$ is an exception, where the PSD peak is also strong and narrow for the 3Dv case, but it becomes weak and distributed over a broader band for the 3Dp case. It was also seen in Figure 54 and Table 2

that the mean centerline velocity evolution and closure length are significantly different (over $1.1d$) between the two cross-sections at this Reynolds number.

The Strouhal number associated with the vortex shedding in the wake of the two cross-sections of the 3D cylinder falls in between the St_d values for the 2Dp and 2Dv cases at all of the studied Reynolds numbers. It is also always lower than the value for the smooth cylinder. In fact, the smooth cylinder shows the highest Strouhal number compared to all cases with surface topology over the studied Reynolds number range. It is only at $Re_d = 1800$, where the St_d becomes similar between the smooth and 2Dv cylinders within the uncertainty. At $Re_d = 1400$, the PSD peaks for the valley geometries are strong, while those for the peak geometries decay and become very weak. The latter geometries also have their respective maximum l_c values at this Reynolds number. Overall, the effect of surface topology on the trend of the most wake features is Reynolds number dependent, which suggests there are different flow regimes each cylinder undergoes over the studied range of Reynolds numbers.

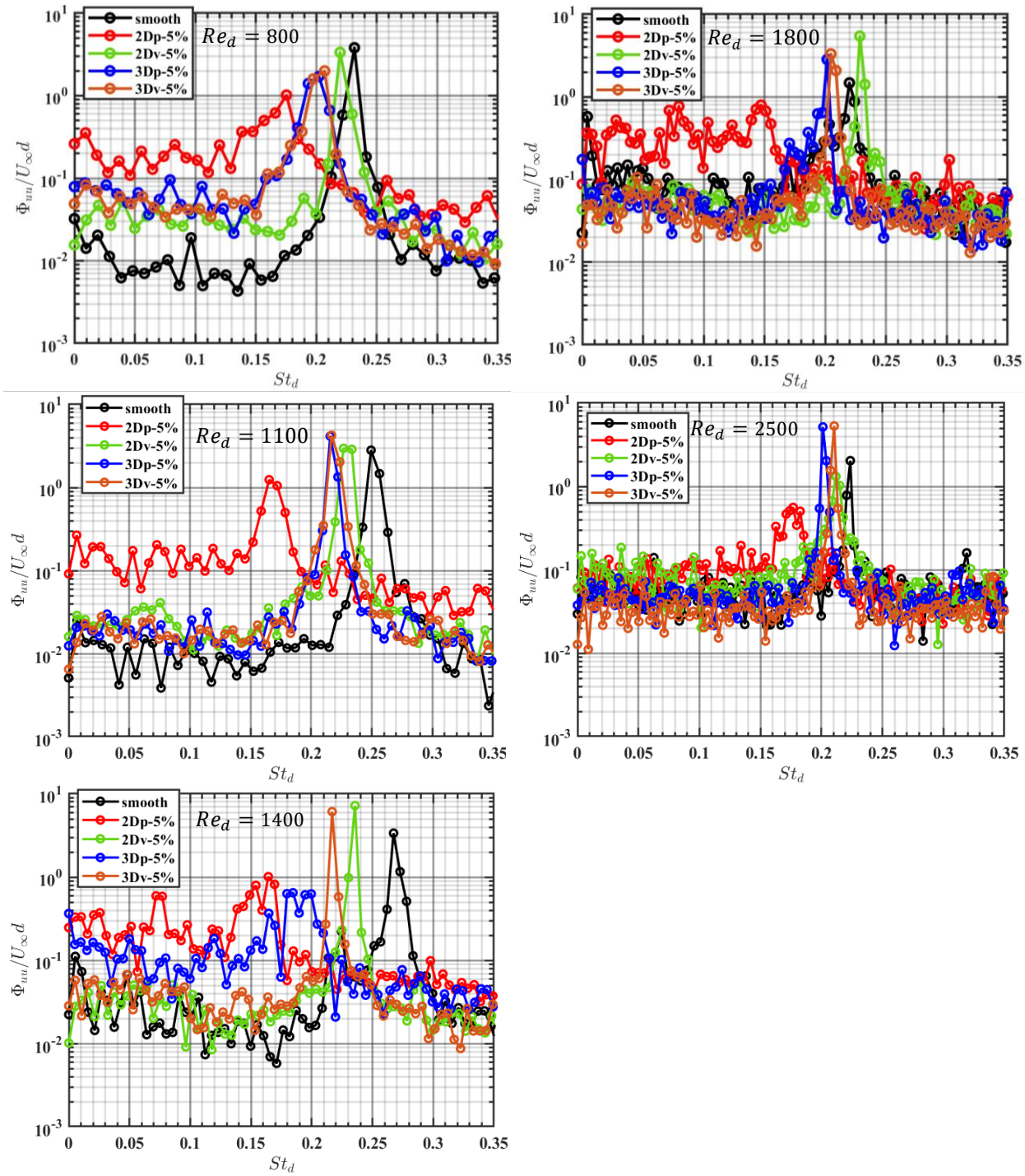

Figure 56. Power spectral density vs. Strouhal number based on the baseline cylinder width for the Reynolds number range $Re_d = 800 - 2500$, measured at $x/d \approx 5.8$ and location of the highest fluctuations along the cross-stream direction.

The influence of surface topology on the St_d values of the PSD peak for different cases, reported in Table 2, is evident. The spread in St_d across the geometries at different Reynolds

numbers can be seen in Figure 57 (top), where many of the datapoints deviate from the average for all geometries by more than 10%. This convergence of the St_d values is also highly sensitive to Reynolds number, which demonstrates the strong Reynolds number dependency of the surface topology effect. A distinct example is the 2Dp cylinder showing the lowest value of $St_d = 0.15$ overall. When the boundary layer characteristics were discussed in Chapter 3, this cylinder was observed to develop an open separation bubble at the lower Re_d, with the shear layer located farthest from the surface compared to the other geometries. With reference to the literature reviewed below, it is thus concluded that one way that the surface topology influences vortex shedding frequency is by displacing the top and bottom shear layers away from each other in the near wake. The presence of surface topology and whether it is 2D or 3D affects the separation/reattachment of the boundary layer and, as a result, alters the spacing between the shear layers in the immediate wake of the cylinders. It is discussed in the existing literature that the latter has a substantial effect on the wake and subsequent vortex shedding frequency.

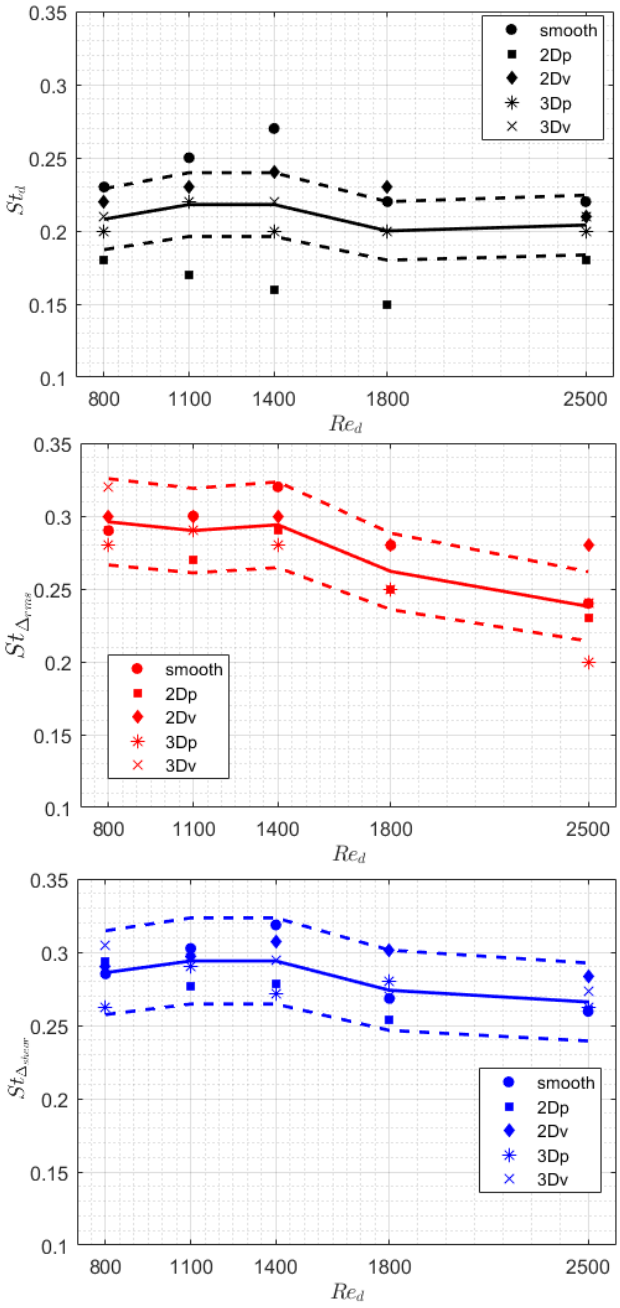

Figure 57. Vortex shedding Strouhal number comparison for all cylinders. St_d (top), $St_{\Delta_{rms}}$ (middle), and $St_{\Delta_{shear}}$ (bottom). The solid line in the plot represents the average value at each Reynolds number, while the broken lines indicate ±10% deviation from the average.

Okajima [5], in his study of rectangular cylinders, infers that the shedding frequency is roughly inversely related to the wake width. This hypothesis was presented earlier by Fage & Johansen [26]. They suggest calculating the Strouhal number using the distance between the shear layers in the near wake when they become parallel before "rolling-up" as the proper length scale

instead of the body dimensions, and postulate that doing so helps correlate the vortex shedding frequency and leads to approaching a universal Strouhal number. Roshko [27] developed an inviscid model based on the free-streamline theory [28] to predict the drag of the bluff bodies and made use of the idea that the Strouhal number becomes universally a function of Reynolds number if scaled based on the separation between the shear layers.

One definition of the center of the shear layer used in the literature is at the transverse location where the maximum streamwise velocity fluctuations occur [23-25]. Thus, the distance between the y locations of the maximum u_{rms} across each x/d can be used as a way to calculate the distance between the shear layers Δ_{rms} (see Figure 44). The studies [23-25] also consider the vortex formation (roll-up) region for circular cylinders to be the immediate wake, up to the streamwise location of the maximum u_{rms}, or up to the streamwise location where the shear layers have the narrowest cross-stream distance from each other. Following the literature, the trajectory of the shear layer center is here defined as the location of the maximum u_{rms} at each streamwise location and is extracted from the boundary layer and wake measurements, up to the formation length l_u (see Figure 44), and subsequently superposed on the color contour maps of the fluctuating velocity u_{rms} in the wake as seen in Figure 42, Figure 46, Figure 48, Figure 50, and Figure 52. The shear layer separation, Δ_{rms}, is then quantified as the cross-stream distance between the u_{rms} maxima on the top and the bottom sides of the cylinder at the most upstream measurement location in wake measurements, $x/d \approx 1.2$ (see Figure 44). The results are listed in Table 2. This location is well within the formation region, since it is located upstream of the location with the highest velocity fluctuations. The Strouhal number values based on Δ_{rms} are also listed in Table 2, and plotted in Figure 57 in red.

A qualitative comparison between the black and red datapoints in Figure 57 demonstrates a significant decrease in the spread of the Strouhal number of the PSD peak for different cylinders when the Strouhal number is calculated based on Δ_{rms} at the lower Reynolds numbers. Such convergence, however, is not seen at the higher Reynolds number of $Re_d = 2500$. As will be further discussed in Chapter 5, the shear layer over the surface of the cylinders becomes unsteady at this Reynolds number and, in some cases, rolls up to form vortices upstream of the wake. Therefore, the vortex shedding mechanism needs to be distinguished for the cases with and without shear layer roll-up upstream of the trailing edge.

In another attempt to further reduce the variability in Strouhal number among different geometries, the maximum separation between the centers of the top and bottom shear layers over the surface of the cylinders Δ_{shear} is used as the length scale to calculate $St_{\Delta_{shear}}$. The center of the shear layer in this analysis is defined as the location of the maximum $\frac{d\overline{u}}{dy}$ from the mean velocity profiles. Results of this analysis are plotted in blue datapoints in Figure 57 (bottom) and compared against the Strouhal numbers calculated using cylinder width d and wake width Δ_{rms}. A qualitative comparison demonstrates an improved collapse of the $St_{\Delta_{shear}}$ datapoints at all Reynolds numbers compared to St_d. However, calculating the Strouhal number this way results in a slightly worse collapse at the intermediate Reynolds numbers $Re_d = 1400$ and 1800.

Comparison of the spread in $St_{\Delta_{rms}}$ and $St_{\Delta_{shear}}$ versus St_d is quantitatively done for all cases, excluding the 3D geometry cases and is reported in Table 3. 3D cases are excluded since Δ_{rms} and Δ_{shear} are found to be different in the two spanwise planes of measurement, i.e., 3Dp and 3Dv, and it is not known which of these values would be more relevant, or how to appropriately define a single shear layer separation distance for the cylinder in the presence of flow three dimensionality which is seen in the preliminary visualizations of the spanwise velocity.

Table 3. Comparison of the Strouhal number spread when calculated based on the baseline width d, wake width Δ_{rms}, and maximum separation of top and bottom shear layers Δ_{shear}. 3D cases are excluded.

	$\frac{(St_d)_{max} - (St_d)_{min}}{\overline{St_d}}$	$\bar{St}_d$	$\frac{(St_{\Delta_{rms}})_{max} - (St_{\Delta_{rms}})_{min}}{\overline{St_{\Delta_{rms}}}}$	$\bar{St}_{\Delta_{\mathrm{rms}}}$	$\frac{(St_{\Delta_{shear}})_{max} - (St_{\Delta_{shear}})_{min}}{\overline{St_{\Delta_{shear}}}}$	$\bar{St}_{\Delta_{shear}}$
$Re_d = 800$	23.8%	0.21	3.4%	0.29	0.1%	0.30
$Re_d = 1100$	36.9%	0.22	10.3%	0.29	6.8%	0.28
$Re_d = 1400$	49.5%	0.22	9.9%	0.30	13.2%	0.30
$Re_d = 1800$	40.0%	0.20	11.1%	0.27	18.3%	0.27
$Re_d = 2500$	19.7%	0.20	20.0%	0.27	7.5%	0.30

The spread is seen to decrease significantly when using length scales representative of the wake width in comparison to the Strouhal number calculated based on the baseline cylinder width at all Reynolds numbers. The only exception is $Re_d = 2500$, where $\bar{St}_{\Delta_{\mathrm{rms}}}$ shows a comparable spread. As mentioned before, the wake width results in a better convergence at the intermediate Reynolds numbers $Re_d = 1400$ and 1800, and the maximum shear layer separation results in the best convergence at other Reynolds numbers.

The spread for each Strouhal number definition is also calculated for all the cylinders, excluding the 3D geometry cases, across the Reynolds number range. It is determined as the difference between the maximum and minimum Strouhal number values, expressed as a percentage of the average value, to assess the independence or sensitivity of the definition to Reynolds number. The results show that the spread is 11.1%, 19.0%, and 12.9% of the average values (0.21, 0.28, and 0.29) for St_d, $St_{\Delta_{rms}}$, and $St_{\Delta_{\mathrm{shear}}}$, respectively. Therefore, defining the

Strouhal number based on the wake width or the separation between the shear layers does not lead to a stronger independence of Reynolds number.

Altogether, these results suggest that changing the initial wake width (shear layers separation in the near wake) and the maximum separation of the top and bottom shear layers are important influences of surface topology on the vortex shedding frequency. This is caused by the topology effect on the boundary layer separation/reattachment behavior on the cylinder's surface. However, altering the wake width and shear layers separation are not the sole influences, and there are other mechanisms through which the topology alters the shedding frequency. For instance, the maximum u_{rms} velocity over the surface of the 2Dp cylinder at $Re_d = 2500$ (see Figure 46) is larger than that in the wake. As noted earlier, there is a signature of vortex formation in the shear layer above the side surface of the 2Dp cylinder towards its trailing edge at this Reynolds number which will be discussed in detail in Chapter 5. In addition, the effect of topology on each of these length scales becomes more significant at certain Reynolds numbers.

Using the wake width and maximum shear layer separation as the length scales in calculating the Strouhal number for the 3D cases might be sufficient at lower Reynolds numbers when the flow is rather two dimensional. However, at higher Reynolds numbers, the flow is likely three-dimensional over the surface and in the wake of the 3D cylinder, and as a result, the behavior over separate cross-sections cannot be studied in isolation.

Chapter 5. On the Unsteady Behavior of the Flow

The previous chapters covered analysis of the main statistics of the boundary layer and the wake flow of the rectangular cylinders without/with surface topology in a range of Reynolds numbers. In this chapter, an attempt is made to complement this investigation to learn more about the flow physics by focusing on some of the key unsteady flow features. Moreover, the connection between the boundary layer and wake flow unsteady characteristics is explored by utilizing a combination of quantitative analysis and qualitative flow visualization.

The findings in Chapter 3 showed a Reynolds number dependent effect on the boundary layer unsteady characteristics (u_{rms}/U_{∞}). However, the question of what drives this unsteadiness remains unanswered. For example, it is unclear if transition of the separating shear layer, wake vortex shedding, some other flow feature, or combination of effects dominate the boundary layer unsteadiness. Chapter 4 demonstrated the effect of surface topology and Reynolds number on the wake flow and the vortex shedding frequency. It is yet to be determined, however, how the boundary layer behavior might connect to the wake vortex shedding frequency, and the wake vortex structure organization and phase-average signature. These points are examined in this chapter. In the interest of conciseness, the focus of this examination is primarily on the smooth cylinder geometry.

Before presenting results, a brief summary is made of the existing understanding of the flow physics over the rectangular cylinder geometry in order to help draw connections between the boundary layer and wake flow characteristics in later discussions. Unfortunately, the existing literature on the rectangular geometry with round corners is very limited. With the exception of the work of Parker & Welsh [6], the relevant information can only be found on the sharp-corner rectangular cylinders. Even the study of Parker & Welsh does not provide basis for a direct

comparison, since it focuses on the effect of side ratio on the shedding frequency and boundary layer behavior at much higher Reynolds numbers compared to the present study. Moreover, the study does not examine Reynolds number effect. Therefore, sharp-corner rectangular cylinders literature will be used as a background to help discuss the key elements of boundary layer and wake connections. While boundary layer separation is fundamentally different between the sharp- and round-corner cylinders (fixed versus non-fixed separation point), subsequent behavior of the separating shear layer upstream of the wake has common qualitative features between the two geometries. This includes the formation of open or closed separation bubble, shear layer transition, and shear layer and wake vortex formation.

Numerous studies have been done on the flow around rectangular cylinders with sharp corners. One important geometrical feature of these cylinders that can strongly affect the flow behavior is the side ratio and the associated length of the afterbody, which is defined as the length of the cylinder's surface downstream of the separation location of the shear layers that roll up into the wake vortices [4]. As illustrated in Figure 58 (top), for a sharp-corner cylinder, the afterbody normalized by d can be either the same as c/d for open separation, or zero for closed separation bubble (i.e. the shear layer reattaches then separates again at the TE to form the wake vortices). For the round-corner cylinder, the length of the afterbody for open separation is less than c/d and depends on Reynolds number. For closed separation, the afterbody length will be larger than zero and depends on where separation occurs after reattachment (Figure 58, bottom).

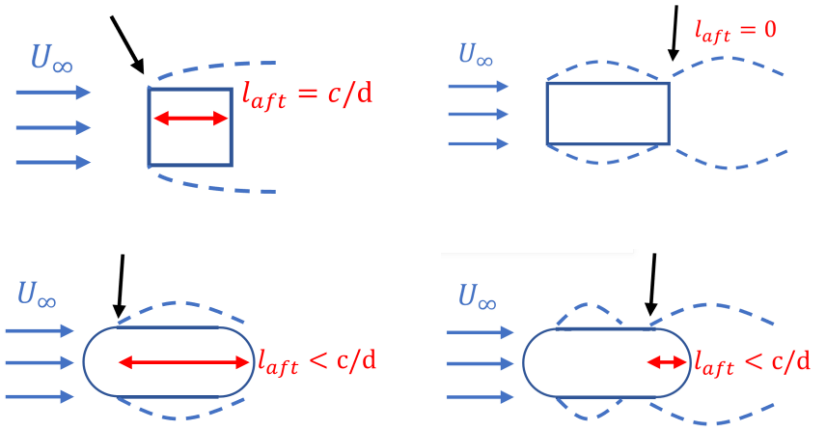

Figure 58. Illustration of the afterbody length l_{aft} for a sharp- (top) and round-corner (bottom) cylinders. The broken blue lines indicate the trajectory of separated shear layers, the black arrow represents the separation point of the shear layer that rolls up into the wake vortices farther downstream. The extent of the afterbody is marked by the red arrows.

Okajima [5] studied the velocity spectra in the wake of sharp-corner rectangular cylinders with different side ratios in the Reynolds number range $Re_d = 70 - 20{,}000$. Measuring the Strouhal number associated with the dominant frequency, he found that the Strouhal number remains approximately in the range $0.12 - 0.14$ for most of the Reynolds number range for a square cylinder ($c/d = 1$). A plot of his results is reproduced in Figure 59.

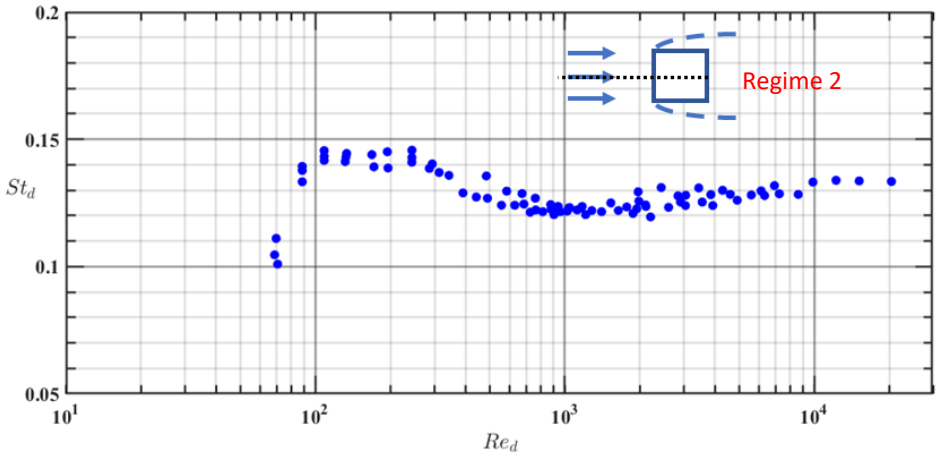

Figure 59. Strouhal number in the wake of rectangular cylinders with side ratio $c/d = 1$ (square). Based on results from Okajima [5]. Sketch depicts the cylinder geometry with the separated shear layers indicated with broken lines.

The cylinders with side ratio $c/d = 2$ and 3 (Figure 60 and Figure 61, respectively) show an abrupt drop of the dominant Strouhal number with increasing Reynolds number. No additional abrupt jump of the Strouhal number is demonstrated with further increase in the Reynolds number for the cylinder with side ratio $c/d = 2$, as can be seen in Figure 60. However, the Strouhal number for the cylinder with $c/d = 3$ recovers at a high enough Reynolds number to a value close to the low-Reynolds-number value before the drop (see Figure 61).

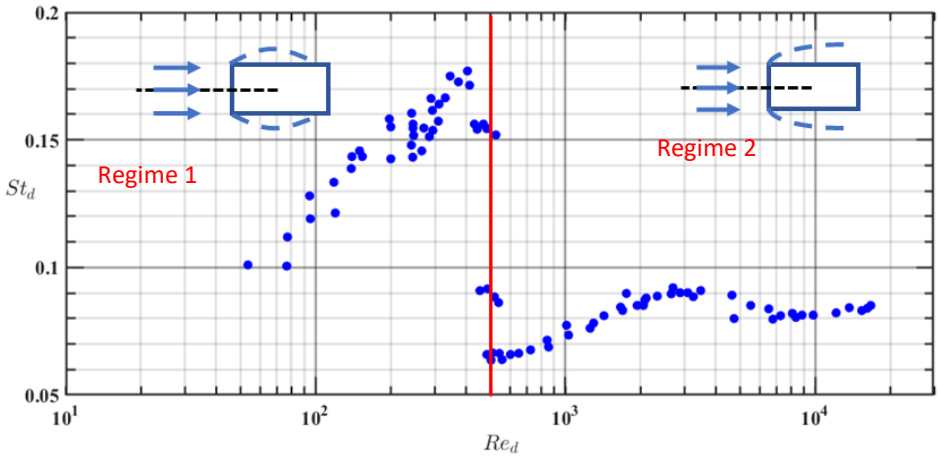

Figure 60. Strouhal number in the wake of rectangular cylinders with side ratio $c/d = 2$. Based on results from Okajima [3]. Sketches depict the cylinder geometry with the separated shear layers indicated with broken lines.

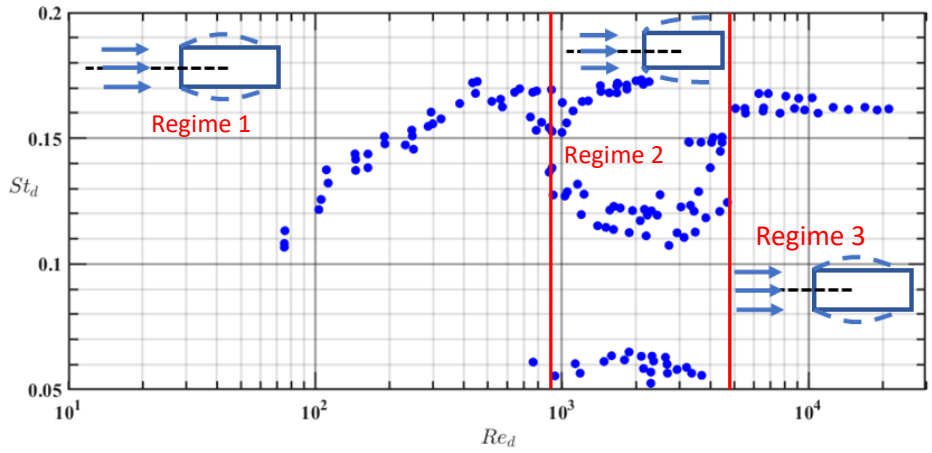

Figure 61. Strouhal number in the wake of rectangular cylinders with side ratio $c/d = 3$. Based on results from Okajima [3]. Sketches depict the cylinder geometry with the separated shear layers indicated with broken lines.

Analyzing flow visualization images, Okajima explains the connection between the boundary layer behavior and the Strouhal number of the wake vortex shedding. He reveals the existence of different flow regimes based on the geometry's side ratio. It is well known that the boundary layer separation point is fixed on the sharp corners of the leading edge. For the cylinders with very small side ratio, there is not enough body length for the separated shear layer to reattach to the surface. Therefore, the open separation of the boundary layer exists over the full range of Reynolds numbers, and the wake is relatively wide and the Strouhal number is generally low and does not show an abrupt change (Figure 59).

For the cylinder with $c/d = 2$, the separated shear layer reattaches to the surface at very low Reynolds numbers (this is labeled as Regime 1 in Figure 60), but the separation bubble lengthens as the Reynolds number increases up to a point that the shear layer fails to reattach. Opening up of the separation bubble is associated with abrupt drop in the Strouhal number and widening of the wake. This situation corresponds to switching from Regime 1 to Regime 2 in Figure 60. Power spectra of the fluctuating velocity however, reveal that in this switch there is a transient range of Reynolds numbers where both the high and low frequencies in the wake co-exist. As the Reynolds number increases in Regime 2, the lower frequency gains energy and the higher frequency gradually fades away. Okajima explains this by pointing out that in this Reynolds number range, the boundary layer intermittently switches between fully open separation and reattachment over different cycles. In other words, although the mean velocity profile may suggest either reattached flow or open separation, instantaneously, the boundary layer may in fact reattach or fail to do so occasionally in this transient region. Further increase of the Reynolds number in the range studied by Okajima does not cause the separated shear layer to reattach again, hence the absence of a Strouhal number recovery.

The same observations hold for the cylinder with the higher side ratio $c/d = 3$, except that in addition to the Strouhal number associated with Regime 1, there are two PSD peaks observed when transitioning from Regime 1 to Regime 2. Okajima reports as many as three Strouhal numbers at some Reynolds numbers. For this cylinder, at a high enough Reynolds number, the shear layer exhibits transition and vortex formation above the cylinder's sidewall, leading to reattachment of the boundary layer and narrowing of the wake, which causes a recovery of the Strouhal number. This is labeled as Regime 3 in Figure 61. When the afterbody is long enough, which is the case for the cylinder with $c/d = 4$ in Okajima's study, the maximum length of the separation bubble over the full range of Reynolds numbers is shorter than c and the separation bubble never becomes open. Therefore, no abrupt changes of the Strouhal number are observed with increasing Reynolds number (these results are not depicted here). Subsequent studies (e.g. Norberg [29] and references therein) confirmed the results of Okajima [3] and provided similar interpretations of the connections between the boundary layer behavior and the vortex shedding Strouhal number. It is notable that generally, previous studies have relied on flow visualization in interpreting the boundary layer behavior. The present work is unique in that it takes advantage of the high-resolution capability of 1c-MTV to analyze the boundary layer using velocity data.

5.1 Nature of the Boundary Layer Unsteadiness

Power spectral density is calculated to investigate the dominant frequencies of the velocity fluctuation in the boundary layer as the first step to analyze the boundary layer unsteadiness. PSD analysis is carried out at two streamwise locations of $x/d = 0$ and 0.71 above the cylinder's surface, and the cross-stream location of the maximum fluctuations (u_{rms}). The streamwise locations are picked to represent the boundary layer behavior at the mid-cord and just upstream of the trailing edge rounded corner (ahead of the start of the wake development), respectively. The

results are then compared against the PSD analysis in the "far" wake at $x/d = 6$ to investigate the extent by which the boundary layer fluctuations are influenced by the wake vortex formation. The results are shown in Figure 62 and Figure 63 using a logarithmic and a linear ordinate, respectively.

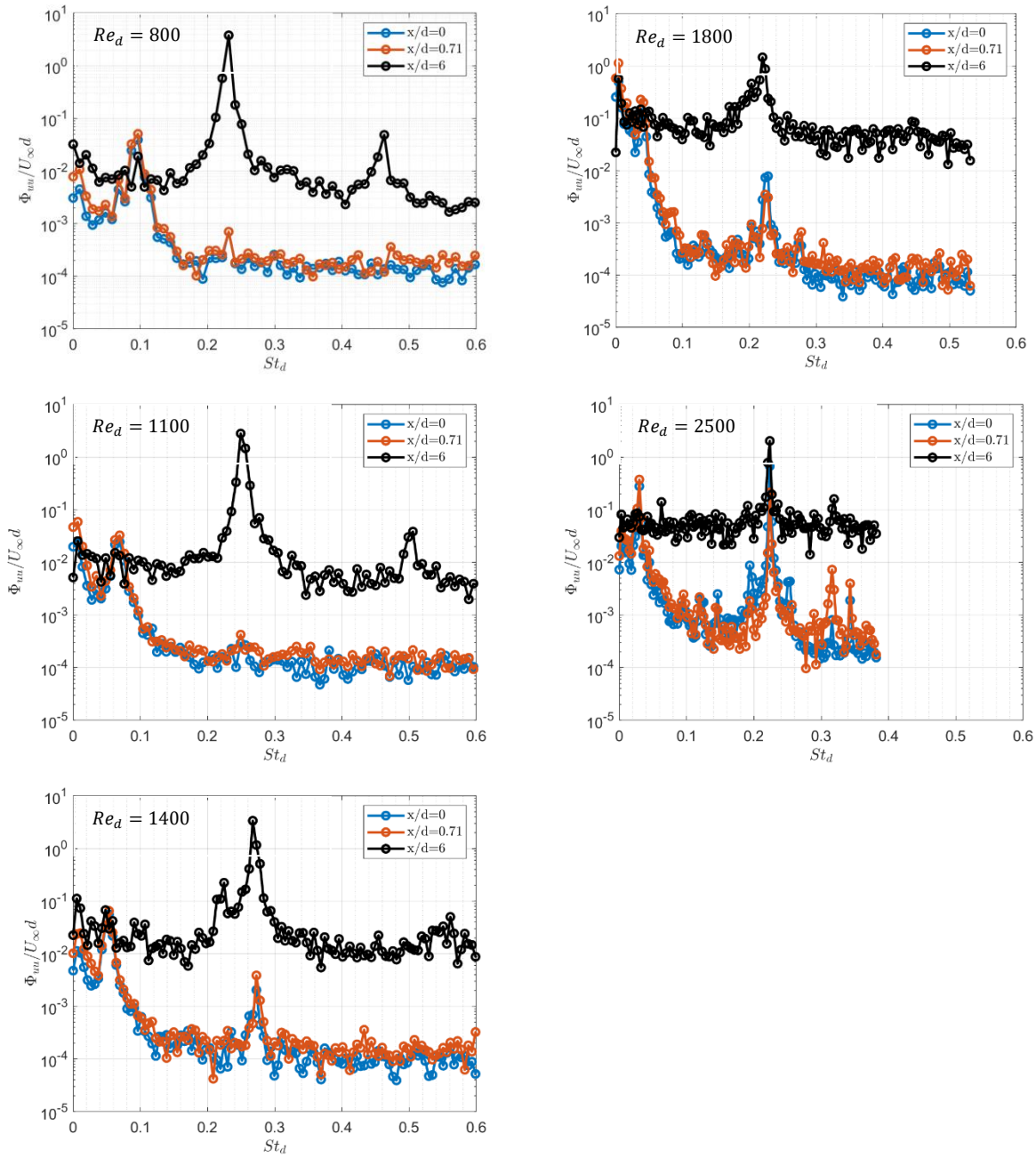

Figure 62. Power spectral density vs. Strouhal number of the smooth cylinder in the Reynolds number range $Re_d = 800 - 2500$ measured at different streamwise locations and at the location of the highest fluctuations along the cross-stream direction. y-axis is logarithimc to make local peaks visible regardless of strength.

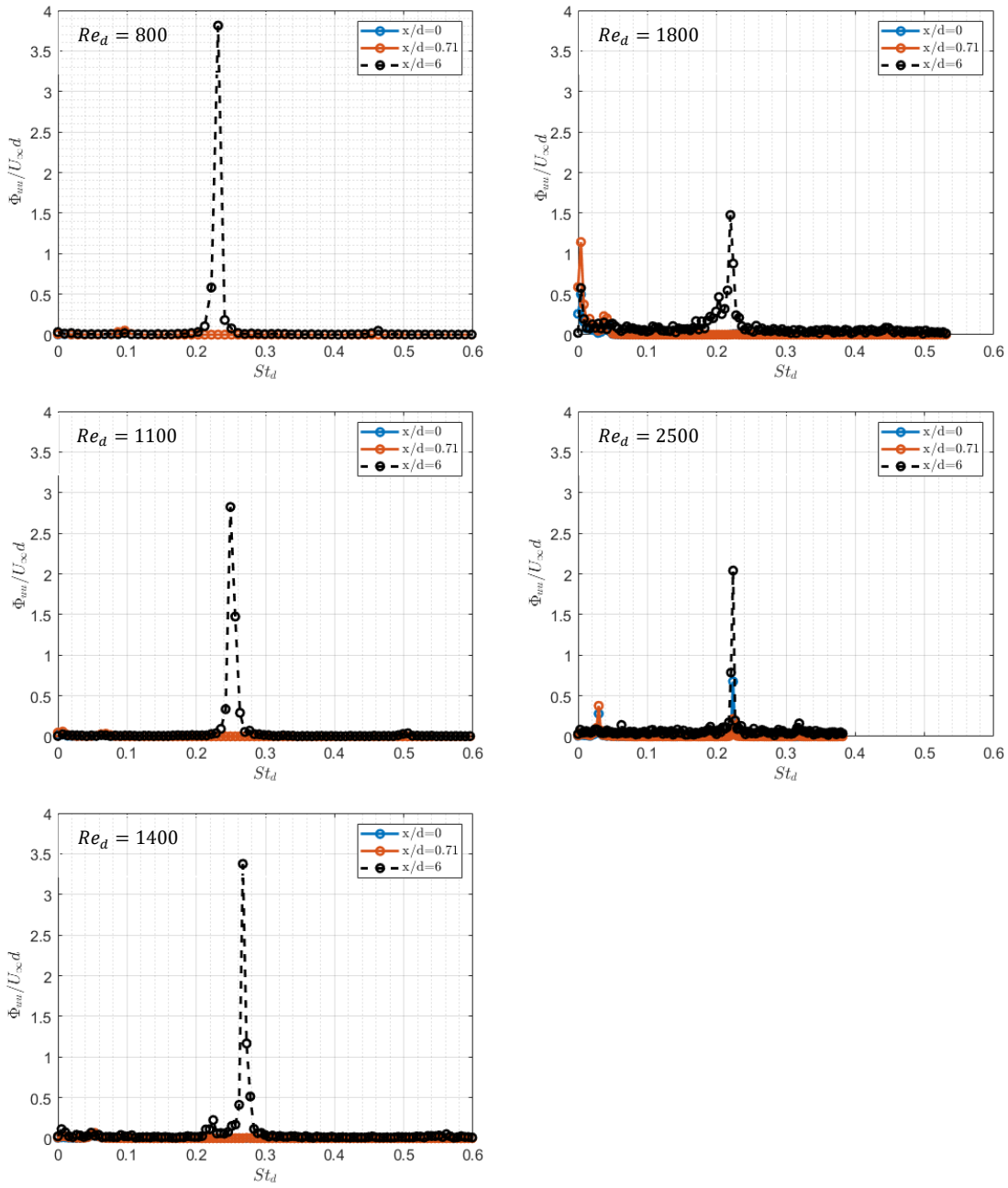

Figure 63. Power spectral density vs. Strouhal number of the smooth cylinder in the Reynolds number range $Re_d = 800 - 2500$ measured at different streamwise locations and at the location of the highest fluctuations along the cross-stream direction. y-axis is linear to better appreciate the relative importance of spectral peaks.

Similar to the results from Chapter 4, Figure 62 and Figure 63 depict a clear and strong spectral peak at $x/d = 6$ corresponding to the vortex shedding frequency for all Reynolds numbers. At the lowest two Reynolds numbers, $Re_d = 800$ and 1,100, no peak is found at the

shedding frequency in the PSD of the boundary layer ($x/d = 0$ and 0.71). This indicates that the boundary layer unsteadiness at these low Reynolds numbers is unaffected by vortex shedding. At $Re_d = 800$, the vortex formation length is $l_u/d = 2.45$ (see Table 1 in Chapter 4), which is significantly larger than the rest of the Reynolds numbers. It is possible that in this case, vortex formation is occurring too far downstream of the cylinder to practically affect the boundary layer flow. The same argument, however, cannot be used for $Re_d = 1{,}100$ since in this case $l_u/d = 1.8$, which is practically the same as $l_u/d = 1.81$ for $Re_d = 1{,}400$. The latter Reynolds number shows signs of the wake vortex formation affecting the boundary layer flow (Figure 62). Thus, the absence of the wake effect at $Re_d = 1100$ is likely not caused by the remoteness of vortex shedding from the cylinder. However, as can be seen from Figure 62 and Figure 63, the strength of the PSD peak of vortex shedding (at $x/d = 6$) is higher at $Re_d = 1400$, compared to 1100, and the associated higher vortex strength may be the cause that vortex shedding unsteadiness is felt at $Re_d = 1400$ but not 1100 despite the similar vortex formation length.

At the higher Reynolds numbers of $Re_d = 1800$ and 2500, the wake vortex shedding frequency is clearly visible in the boundary layer frequency content, indicating an interaction between the wake vortex shedding and boundary layer behavior. In fact, at $Re_d = 2500$, the peak corresponding to vortex shedding is the largest in the PSD of the boundary layer. At this Reynolds number, vortex formation is the closest to the cylinder with $l_u/d = 1.11$.

Irrespective of whether the vortex shedding frequency is present or absent in the PSD of the boundary layer, with the exception of $Re_d = 2500$, the boundary layer unsteadiness is dominated by low frequency fluctuation. Close inspection of Figure 62, shows that the PSD peaks at low Strouhal number systematically shift towards a lower St_d with increasing Reynolds number. Since Re_d is increased by increasing U_∞, this effect could correspond to peaks that are at a fixed

physical frequency in Hz. This point is checked in Figure 64, where the PSD for all Reynolds numbers and $x/d = 0.71$ are plotted versus frequency in Hz on the same graph over a frequency range that is focused at low frequencies. The results do indeed confirm the fixed nature of this frequency, which is tracked to the slushing frequency of the water tunnel (the same frequency is also found in the freestream). These fluctuations, however, are not significant and become smaller at higher Reynolds numbers (e.g. 1.9% and 1.6% of U_∞ at $Re_d = 800$ and 1400, respectively at $x/d = 0.71$) and we expect them to cause low-level low-frequency modulation of the flow without affecting the flow behavior. Thus, in an ideal facility with zero freestream fluctuation, the boundary layer around the cylinder at $Re_d = 800$ and 1100 should be steady. As the Reynolds number is increased to $Re_d = 1400$ and beyond, vortex shedding leads to boundary layer unsteadiness with the effect becoming stronger with increasing Re_d, at least within the range investigated.

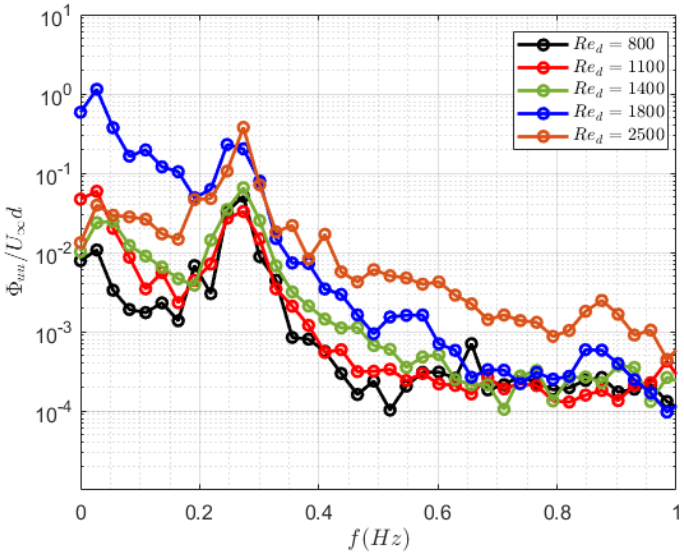

Figure 64. Demonstration of the signature of the sloshing frequency of the water tunnel on the measured velocity spectra. Power spectral density vs frequency of the smooth cylinder in the Reynolds number range $Re_d = 800 - 2500$ measured at $x/d = 0.71$ and at the location of the highest fluctuations along the cross-stream direction. Focusing on low frequencies to zoom on the trace of the tunnel sloshing.

In the Reynolds number range $Re_d = 800 - 1400$, power spectral density in the wake shows a clear sign of vortex shedding at a Strouhal number which keeps increasing with Reynolds number (black lines in Figure 62 and Figure 63). The second harmonic is also seen in the spectrum at twice the shedding frequency for $Re_d = 800$ and 1100. In Chapter 3, the boundary layer mean velocity profile indicated a reattached boundary layer over the surface of this cylinder at these Reynolds numbers. These characteristics of a reattached boundary layer and increasing St_d with Re_d are consistent with Regime 1 behavior of the sharp-corner cylinder in Figure 60 and Figure 61.

As the Reynolds number increases further to $Re_d = 1800$, the boundary layer mean separation bubble becomes open (Chapter 3) and the vortex shedding St_d drops from 0.27 at $Re_d = 1400$ to 0.22 at $Re_d = 1800$. These features are analogous to Regime 1-Regime 2 transition in Figure 60 and Figure 61. It is interesting to note that the PSD in the wake at $Re_d = 1400$ shows the emergence of the lower St_d peak at 0.22. At $Re_d = 1800$, that secondary peak at lower frequency takes over and becomes dominant while the higher frequency disappears. Additional increase in Re_d to 2500 maintains St_d at 0.22, although at this Reynolds number the shear layer reattaches on the cylinder sidewall (Chapter 3).

The switch from open to closed separation bubble with Re_d increase from 1800 to 2500 seems to correspond to Regime 2- Regime 3 change for the sharp-corner cylinder in Figure 61. However, as discussed by Okajima [5], such a regime change is associated with Kelvin-Helmholtz vortex formation in the separated shear layer above the cylinder sidewall. Inspection of flow visualization images in this study shows that such vortex formation does not occur for the smooth cylinder at any of the Reynolds numbers investigated. To demonstrate this point, Figure 65 shows a comparison between instantaneous flow visualization snapshots of the smooth cylinder at $Re_d =$

2500 and the 2Dp-5% cylinder at the same Reynolds number. The latter geometry provides a case in which vortex formation occurs in the separated shear layer above the cylinder. Specifically, a vortex formation (highlighted by a red arrow in Figure 65-a) is observed over a surface topology peak, as inferred from the distortion of the MTV lines in Figure 65-a. This vortex travels downstream and remains close enough to the surface to impose reattachment just downstream of its location, as seen in Figure 65-b. Figure 65-c depicts the shedding of a single shear layer vortex into the wake. Similar MTV lines distortion is absent from the visualization images of the smooth cylinder in Figure 65.

The absence of vortex formation above the cylinder sidewall when the shear layer is reattached for the smooth cylinder at $Re_d = 2500$ is consistent with the flow behavior in Regime 1 in Figure 60 and Figure 61 for the sharp-corner cylinder. This suggests that the rectangular cylinder with fully-round LE does not exhibit monotonic regime transitions with increasing Re_d as the sharp-corner cylinder. Specifically, in terms of the boundary layer behavior, as the Reynolds number increases, we observe transition from Regime 1 ($Re_d = 800$, 1100 and 1400) to Regime 2 ($Re_d = 1800$) then back to Regime 1 ($Re_d = 2500$). This is believed to be due to the more complex nature of separation/reattachment on the cylinder with round LE, where the separation point is not fixed. Moreover, unlike the sharp-corner cylinder where separation occurs on the front face, for the round-LE cylinder separation is always observed on the flat part of the sidewall for the cases investigated here. This generally leads to significantly thinner separation zone for the round-LE cylinder compared to the sharp-corner cylinder. In turn, the difference in the separated shear layer trajectory between open- and closed separation bubble is not as significant, and hence the switch between the two states may be sensitive to various factors, such as movement of the separation point, proximity of wake vortex formation location to the cylinder, etc. It is also

noteworthy that although the boundary layer behavior at $Re_d = 2500$ corresponds to Regime 1 of the sharp-corner cylinder, the Strouhal number remains at 0.22 similar to $Re_d = 1400$ and does not exhibit the increase expected from narrowing of the wake associated with reattachment.

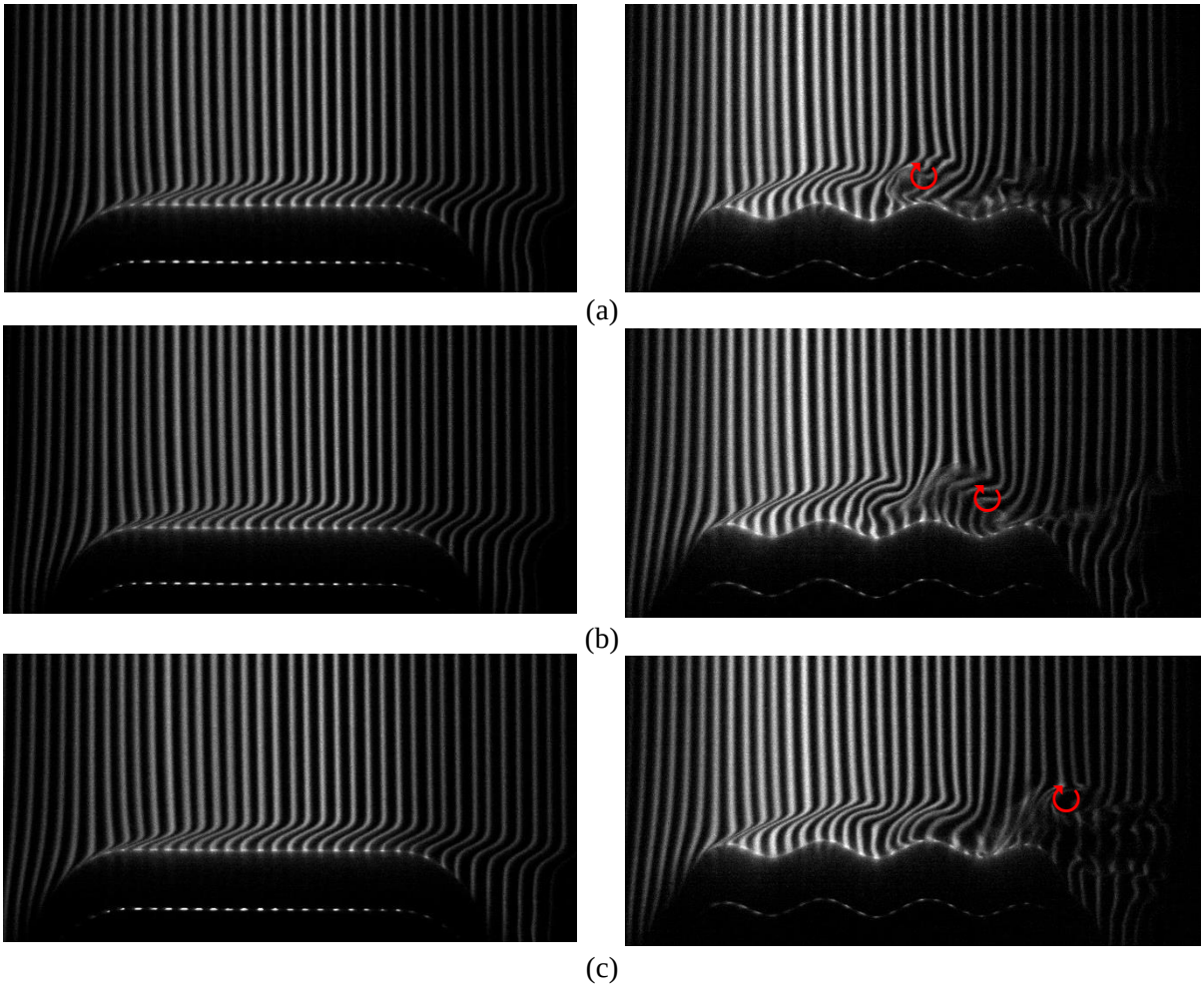

Figure 65. Snapshots from visualization of the boundary layer flow over the smooth cylinder (left) and 2Dp-5% cylinder (right) at $Re_d = 2500$. Red line marks MTV lines distortion implying presence of a vortex.

To achieve insight into the instantaneous separation/reattachment flow behavior, forward flow probability (FFP) is calculated. FFP, which represents the probability of a positive velocity, is calculated at the closest valid pixel to the surface by counting the number of times a positive velocity occurs in a timeseries and dividing the result by the number of points in the time series. The results are demonstrated in Figure 66, plotted versus the streamwise location over the flat

cylinder sidewall. A polynomial curve fit is applied to the data to help visualize the overall trend despite data scatter.

FFP of 50% is sometimes used to indicate locations of separation and reattachment. This works well if the probability density function of the velocity is symmetric at these locations. In Figure 66, the mean separation/reattachment locations based on the mean velocity measurements (from Chapter 3) are superposed as vertical lines on the FFP. These agree well with the locations where the FFP plot crosses 50% level (indicated with the horizontal broken line). Inspecting Figure 66, the FFP is lower than 50% over a certain region of the surface at $Re_d = 800$ and 1400, indicating the presence of separation followed by reattachment. The case of $Re_d = 1100$ shows higher than 50% probability over the whole surface, implying the absence of boundary layer separation *on average*. These observations are completely in line with the mean flow behavior discussed earlier in Chapter 3. Some deviation in the instantaneous behavior from this mean flow picture are however implied from the FFP. Specifically, at $Re_d = 800$, the FFP at the downstream end of the flat sidewall exhibits only 80% FFP, indicating 20% probability of reverse flow. Inspection of instantaneous velocity contour plots does show that indeed occasionally the boundary layer exhibits open, but very thin separation bubble. Also, at $Re_d = 1100$, the flow near the middle of the cylinder exhibit less than 100% FFP but is bounded by 100% FFP on the upstream and downstream sides. This implies a relatively rare occurrence of a closed separation bubble above the middle of the cylinder sidewall.

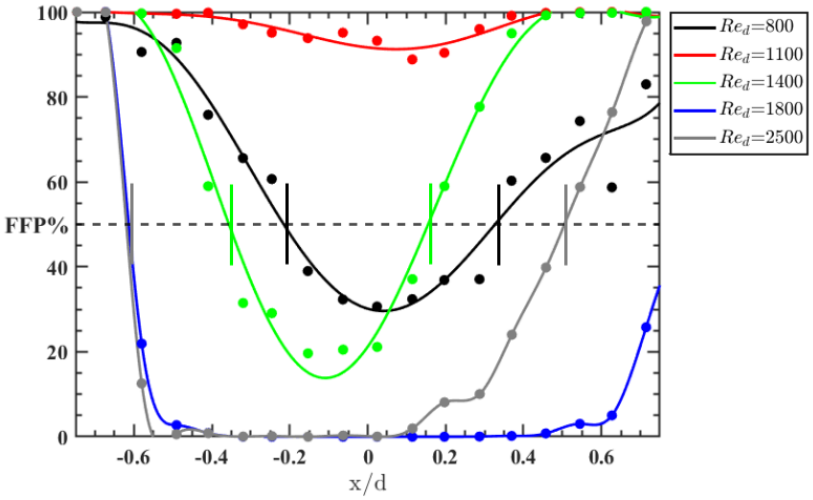

Figure 66. Forward flow probability over the surface of the smooth cylinder at different Reynolds numbers. The vertical lines represent the mean separation and reattachment locations from Chapter 3.

The case of $Re_d = 1800$ had shown a fully separated flow without reattachment based on the mean velocity field analysis. However, it can be seen in Figure 66 that there is 45% probability of reattachment at the most downstream location $x/d = 0.8$. The implication of this observation is that, at this Reynolds number, the boundary layer reattaches to the surface almost half the time, despite of the absence of mean reattachment. Inspection of the velocity field reveals that the flow regime swings between fully separated and reattached states every few cycles, as demonstrated by the two snapshots shown in Figure 67. The top snapshot (Figure 67-a) demonstrates a time snap when the shear layer fails to reattach, corresponding to Regime 2. The bottom snapshot (Figure 67-b) shows a reattached boundary layer on the surface of the cylinder. It is important to note that these snapshots are not taken during the same shedding cycle, but the change of the reattachment behavior of the boundary layer happens every once in a while. Both snapshots correspond to an instant where shedding of positive vorticity at the downstream end of the plot. This is based only on the streamwise velocity in the absence of cross-stream velocity measurements ($\omega_z \approx du/dy$). Therefore, the $Re_d = 1800$ case is not simply a case of an open separation bubble, but an intermittent reattachment of the separated boundary layer.

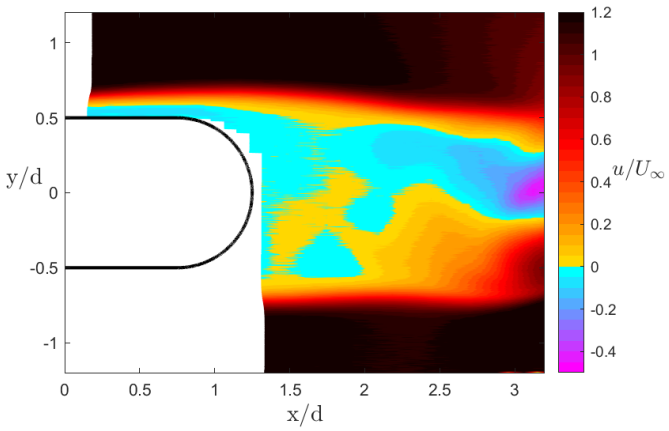

(a)

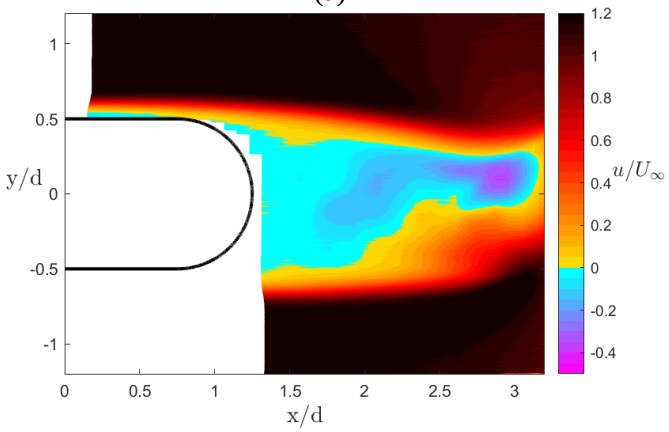

(b)

Figure 67. Instantaneous color contour snapshots of the velocity field in the wake of the smooth cylinder at $Re_d = 1800$. Signatures of (a) separated and (b) reattached boundary layer.

With additional increase to $Re_d = 2500$, the separated boundary layer fully reattaches again to the surface, given that the FFP crosses the 50% threshold at about $x/d = 0.5$ and becomes very close to 100% before the end of the flat surface (gray line in Figure 66). This behavior may also be observed from the instantaneous snapshots in Figure 68, taken at two different phases of the shedding cycle, corresponding to shedding of positive and negative vorticity in the wake. While there is movement of the reattachment point between the two snapshots (the end of the separation zone, light blue color, is visible in the bottom but not the top snapshot), the boundary layer remains reattached on the flat surface. Therefore, the instantaneous behavior at $Re_d = 2500$ is consistent with the separation bubble remaining closed, as implied from the mean velocity field analysis. Although the bubble does fluctuate in size with the unsteadiness dominated by vortex shedding.

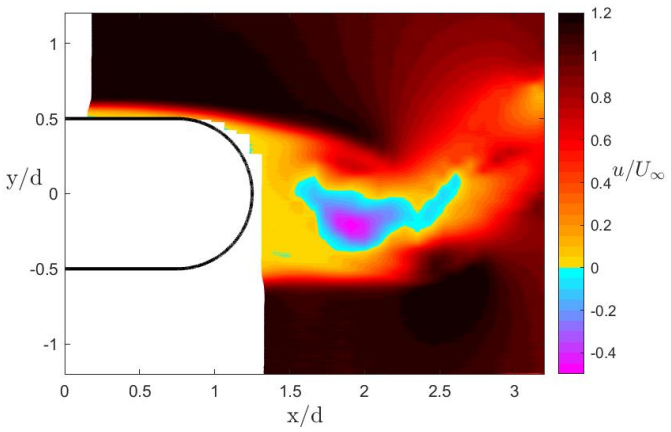

(a)

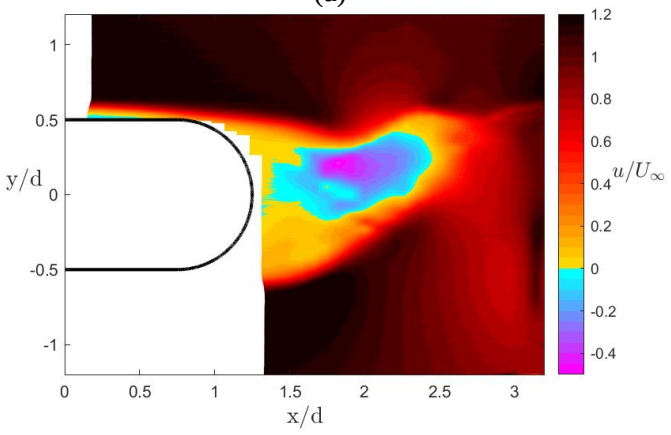

(b)

Figure 68. Instantaneous color contour snapshots of the velocity field in the wake of the smooth cylinder at $Re_d = 2500$. Signatures (a) clockwise and (b) counterclockwise vortices.

To summarize the outcome of the above results, the smooth round-corner cylinder shows a behavior with increasing Reynolds number which is different from the understanding of the sharp-corner cylinder in the literature. The sharp-corner cylinder with a similar side ratio experiences Regimes 1, 2, and 3 consecutively with increasing the Reynolds number. On the other hand, with the range investigated of $800 \leq Re_d \leq 2500$, the round-corner cylinder is seen to undergo Regime 1 at lower Reynolds numbers, "flip-flop" between Regimes 1 and 2 at an intermediate Reynolds number, and jump back to Regime 1 as the Reynolds number is further increased.

There are significant differences between the flow over the smooth round-corner cylinder versus that of a rectangular cylinder with sharp corners. Contrary to the latter case, where the

boundary layer separation point is fixed at the sharp corners, the separation point can move over the surface of the smooth cylinder. Therefore, the flow can separate anywhere over the leading-edge curve, or the flat surface, or in the case of $Re_d = 1100$ even remain attached over the whole forward body (except for possible occasional occurrence of a small separation bubble near $x/d = 0$ as seen from the FFP results in Figure 66).

It is well understood that the reattachment of the boundary layer over the surface of an object is greatly affected by the trajectory of the shear layer. Despite of separation, closed or open, the separated shear layer remains very close to the cylinder sidewall for round-corner smooth cylinder (see Figure 9 in Chapter 3) compared to the sharp corner cylinder. The shear layer also does not undergo transition over the examined Reynolds number range, since flow visualization did not show any sign of vortical structures forming on the surface of the smooth cylinder even at the highest Reynolds number of $Re_d = 2500$. Furthermore, in the latter case, wake vortex formation occurs so close to the cylinder base such that it now largely influences the shear layer unsteadiness over the surface (based on the spectra at $x/d = 0$ and 0.71 in Figure 62 and Figure 63). Flow visualization and velocity snapshots additionally demonstrate the alternate behavior of the boundary layer flow in conjugation with wake vortex formation and shedding. Therefore, the reattachment mechanism for this regime should be differentiated from that of a sharp-corner cylinder, where the shear layer transition causes reattachment.

Comparison of the sharp- and round corner-cylinders in a nutshell shows that the smooth cylinder primarily undergoes Regime 1. A transition to Regime 2 is also observed at an intermediary Reynolds number, but it does not persist all the time. Although the Reynolds number range covered in this study does not capture a case where Regime 2 is fully dominant, it can well take place at a Reynolds number $1400 < Re_d < 1800$ and/or $Re_d > 2500$. Similarly, Regime 3

could occur for sufficiently high Reynolds number. The sharp-corner cylinder, on the other hand, experiences monotonic transition between Regimes 1, 2, and 3 with increasing Reynolds number. It should be noted that for the sharp-corner cylinder the transition from Regime 2 to 3 for $c/d = 2.5$ takes place somewhere in the range $2000 < Re_d < 4000$ (Norberg [29]).

5.2 Phase-Average Analysis of the Wake

As observed from the PSD analysis, Reynolds number affects the strength and the broadness of the spectral peak at the dominant frequency of the velocity fluctuations in the wake of the smooth cylinder. It is assumed that this frequency corresponds to vortex shedding, but this cannot be ascertained from spectral information alone. To extract more details regarding the flow structure corresponding to the spectral peak for different flow regimes discussed above, phase-averaged streamwise velocity profiles are obtained relative to an oscillation cycle at the spectrum-peak frequency. These profiles are used to examine the presence of velocity signatures consistent with the shedding of counter-rotating spanwise vortices into the wake. To obtain the phase average velocity $< u >$, data points in the velocity time series are phase-ordered in 16 phase-bins relative to their location in the oscillation cycle, where each bin contains about 80 datapoints. This location is indicated by the normalized phase ϕ, where $\phi = 0$ is at the start of the cycle and $\phi = 1$ at the end.

The presence of a velocity deficit in bluff body wakes makes it difficult to distinguish the signature of a vortex passing in the phase-averaged velocity profile. To aid the reader in understanding how the vortex signature is identified in the velocity profiles, an idealized velocity profile resulting from the superposition of profiles due to wake deficit $u_d(y)$ and a vortex $u_v(y)$ is demonstrated in Figure 69 for different relative strengths of the vortex (increasing strength from left to right). The top plots correspond to a clockwise vortex with a core center above the wake

centerline, at $y_c/d = 0.25$, while the bottom plots represent a counter-clockwise vortex below the centerline, at $y_c/d = -0.25$. The wake deficit profile is taken as a Gaussian function

$$u_w(y) = \frac{-U_w}{\sigma_w\sqrt{\pi}} e^{-\frac{(y)^2}{2\sigma_w^2}}, \tag{19}$$

where, U_w is the centerline wake deficit and σ_w is a wake width parameter. On the other hand, the vortex profile is based on Gaussian vorticity distribution in the vortex core

$$u_v(y) = \frac{\pi R_o^2 \omega_o}{2\pi(y-y_c)} \left[1 - e^{-\frac{(y-y_c)^2}{R_o^2}}\right], \tag{20}$$

where, R_o is the vortex core radius and ω_o is the maximum vorticity at the vortex core center (located at y_c). The profile parameters are chosen to provide profiles that are comparable to those measured with the increase of the vortex strength achieved by increasing ω_o.

Focusing on the velocity profiles on the top half of Figure 69, each plot contains the wake profile (red broken line), the vortex profile (blue broken line) and the superposed profiles (black line). Examining the case with the weakest vortex signature (left plot), it is clear that the overall signature of vortex presence distorts the wake profile very little, making it difficult to conclude that a vortex is present. This distortion, which can be seen more clearly for the strongest vortex case (right plot) is such that it produces certain asymmetries between the top and the bottom halves of the profile. Specifically, for the clockwise vortex with center above the wake centerline, the asymmetry is such that the magnitude of the maximum positive velocity gradient at the vortex center (above the centerline) is larger than magnitude of the minimum velocity gradient below the centerline. Additionally, instead of the deficit profile smoothly approaching the zero asymptote away from the wake centerline (red line), the overall profile (black line) exhibits an overshoot above the vortex core center and undershoot below (which laterally shifts the minimum profile velocity away from the wake centerline). Similar observations, but with the opposite sense, can be

seen for the presence of a counter-clockwise vortex below the centerline (bottom plots in Figure 69).

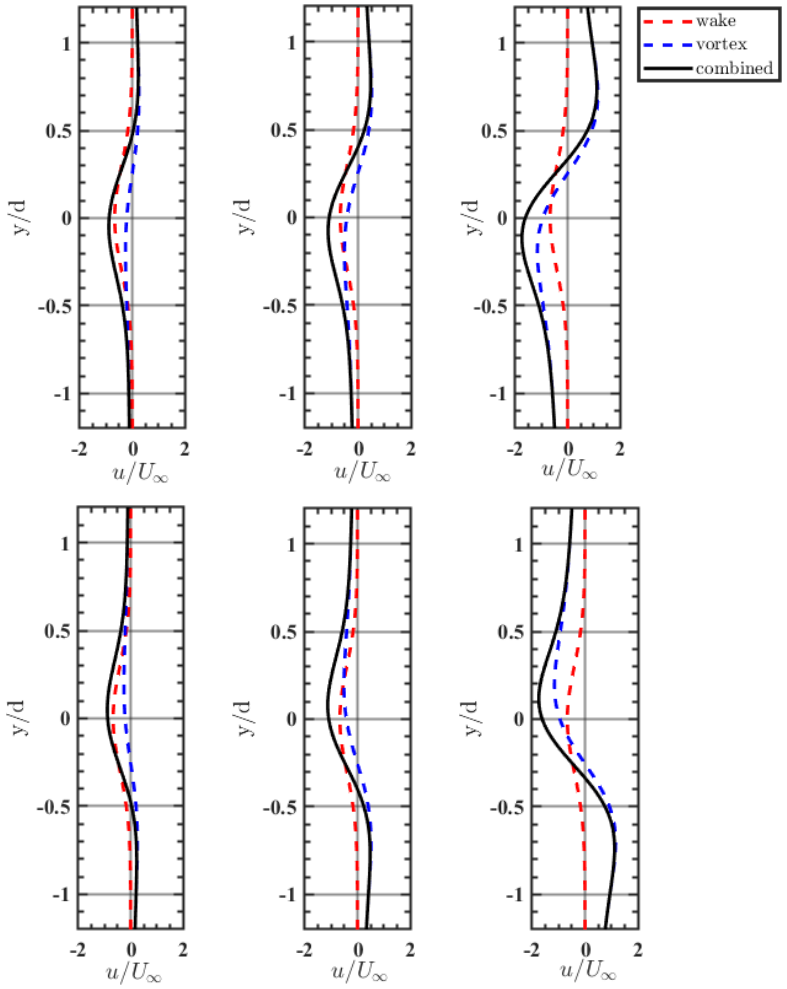

Figure 69. Illustration of synthetic phase-averaged velocity profile constructed from the superposition of wake deficit (red) and Gaussian vortex (blue) streamwise velocity profiles. The vortex strength increases from left to right. The top and bottom rows depict clockwise and counterclockwise vortices with core centers above and under the wake centerline, respectively.

Figure 70 shows the $< u' >=< u > -U_\infty$ profiles for every other ϕ value with an increment of $\Delta\phi = 2 \times 0.0625$ for the smooth cylinder at $Re_d = 800$. ϕ=0 is assigned to the instant with maximum positive velocity gradient $d < u' > /dy$. The phase-average analysis is done at a streamwise location $1d$ distance downstream of the vortex formation location for all cases. This case is discussed as a representative of flow Regime 1.

Following the orientation of Figure 69 , inspection of Figure 70 shows that indeed a $< u' >$ signature typical of the periodic passing of a counter-rotating vortex pair is evident. Specifically, at $\phi = 0$, the velocity profile is qualitatively similar to that of a vortex with clockwise rotation present above the wake centerline. At this phase, the positive velocity gradient is highest, consistent with the presence of the center of a clockwise vortex at the maximum gradient location (identified with a blue circle in Figure 70). Likewise, a similar profile, but with negative velocity gradient, is seen in the middle of the cycle at $\phi = 0.5$, suggesting the passage of a counter-clockwise vortex below the wake centerline. The PSD corresponding to this case, along with other cases considered for the phase-average analysis, is depicted in Figure 71 and exhibits a strong peak that is more than two orders of magnitude above other fluctuations in the spectrum. The PSD results are obtained at the streamwise location of the phase averaging, and the cross-stream location of the maximum u_{rms}.

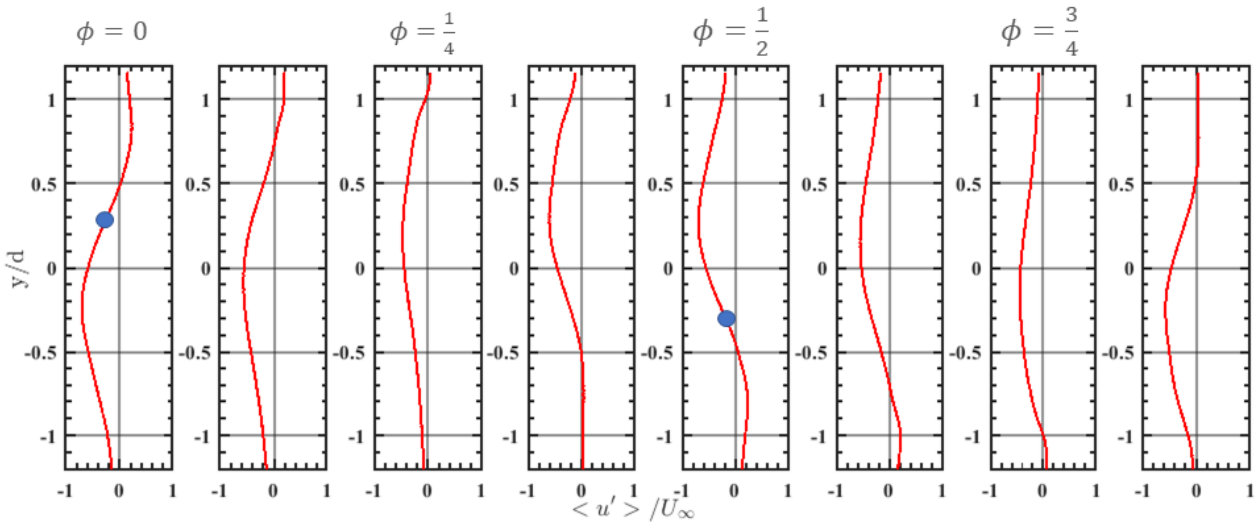

Figure 70. $< u' > /U_\infty$ at different phases measured $1d$ downstream of the formation length at $x/d = 4.7$. Smooth cylinder at $Re_d = 800$. Maximum positive and negative velcoty gradient locations are marked at $\phi = 0$ and 0.5.

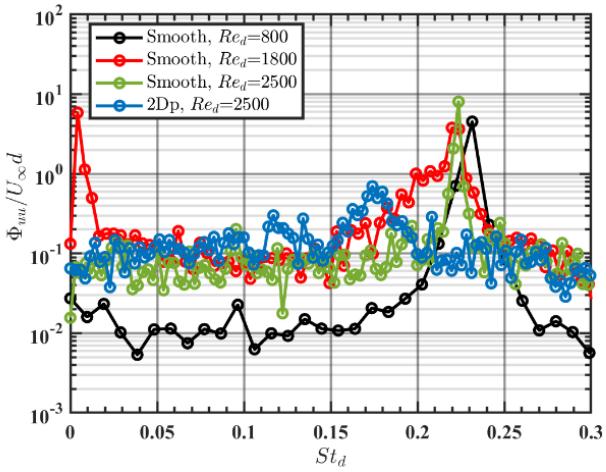

Figure 71. Power spectral density vs. Strouhal number of the smooth cylinder for selected Reynolds numbers at the streamwise location of the phase-average analysis and at the cross-stream location of the highest fluctuations.

To examine the cycle-to-cycle repeatability of the vortex signature, the velocity fluctuations in the wake of the cylinder are decomposed into two components; one accounting for the energy associated with the phase-average velocity, and the other, with the deviation from the phase average. Together with the mean velocity this decomposition is known as triple decomposition, which was first introduced by Hussain and Reynolds [30]. Deviation from the phase average could be the result of variation in the vortex properties from cycle-to-cycle, random fluctuation (such as due to small-scale turbulence), and other possible structures. The decomposition leads to:

$$u_{rms}{}^2 = u'^{\phi}_{rms}{}^2 + u^r_{rms}{}^2 \tag{21}$$

where u'^{ϕ}_{rms} is the rms velocity calculated from the phase-average velocity variation over one cycle, and u^r_{rms} is the rms associated with the remaining fluctuation. Figure 72 depicts this energy decomposition for the smooth cylinder at $Re_d = 800$. A qualitative interrogation of this figure shows that u'^{ϕ}_{rms} accounts for most of the fluctuating energy in the wake of the smooth cylinder at $Re_d = 800$. Therefore, Regime 1 is associated with a well-defined and repeatable wake vortex formation and shedding.

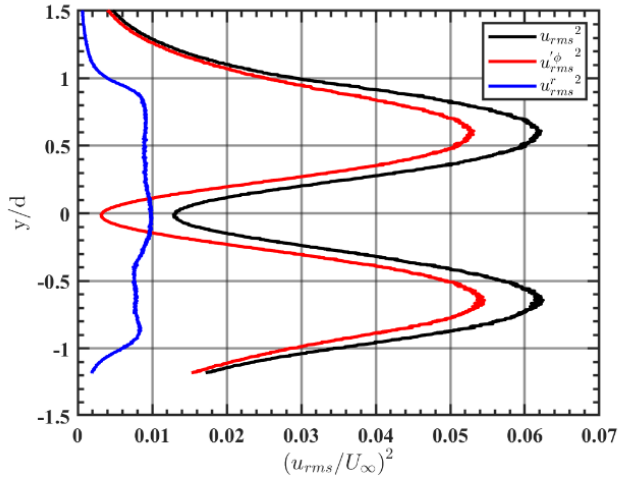

Figure 72. Decomposition of the fluctuating streamwise velocity energy for smooth cylinder at Re_d=800. Measured at $x/d = 4.7$.

$< u' >$ profiles for the smooth cylinder at $Re_d = 1800$ are shown in Figure 73 as a representative of the flow flip-flopping between Regimes 1 and 2. A signature of periodic counter-rotating vortex shedding can be distinguished in the $< u' >$ profiles, although it is much weaker than the signature observed for flow Regime 1. Specifically, the profiles for $Re_d = 800$ in Figure 70 show quite a bit of variation across the phases. In contrast, the profiles for $Re_d = 1800$ predominantly look like wake deficit profiles that do not vary significantly over the phases and do not represent a flow that is dominated by regular vortex formation and shedding. However, the velocity profiles at $\phi = 0$ and 0.5 show a small signature of passing of the vortices with clockwise and counter-clockwise rotation, respectively. The velocity profiles at these phases show the maximum positive and negative velocity gradients $d < u' >/dy$, respectively. Although these gradients are not considerably different from that at the neutral phase $\phi = 0.25$, they represent a small contribution from the organized vortex shedding on the velocity profiles. This observation that phase-averaging the velocity based on the shedding frequency does not result in an obvious vortex signature suggests that the vortex shedding is not highly regular and well-organized. The

PSD for this case shown in Figure 71 supports this conclusion by showing a broader and weaker peak than that of the Regime 1.

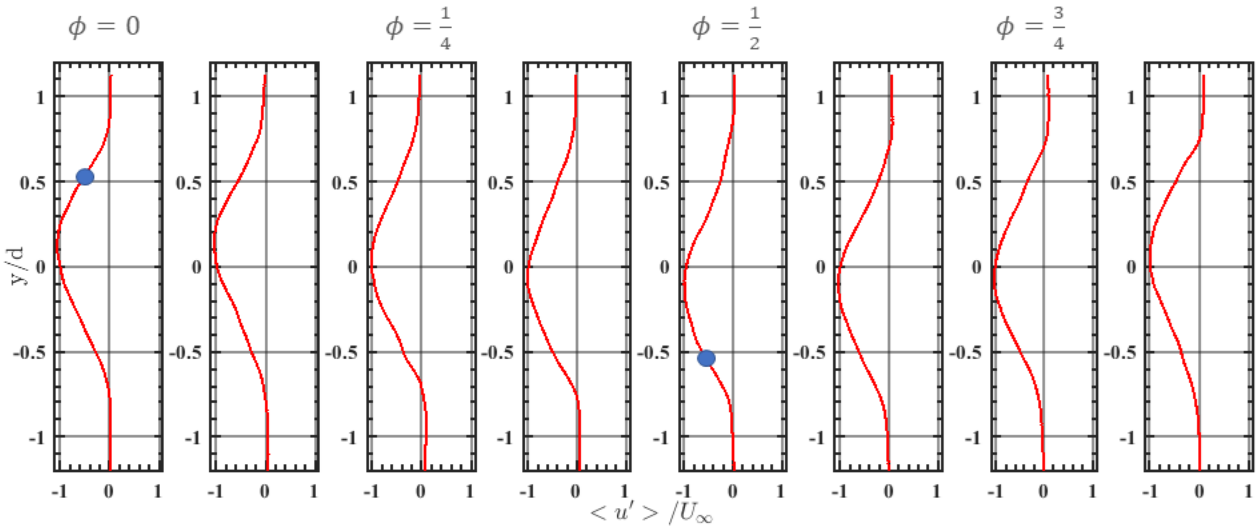

Figure 73.$< u' > /U_\infty$ at different phases measured $1d$ downstream of the formation length at $x/d = 4.1$. Smooth cylinder at $Re_d = 1800$. Maximum positive and negative gradient locations are marked at $\phi = 0$ and 0.5.

Cycle-to-cycle repeatability for the case of smooth cylinder at $Re_d = 1800$ is analyzed by decomposition of the fluctuating streamwise velocity energy and is represented in Figure 74. These results convey a consistent message with the aforementioned analysis that the organized von Karman vortex shedding frequency is weak and does not dominate the velocity fluctuations in the wake of the smooth cylinder at $Re_d = 1800$.

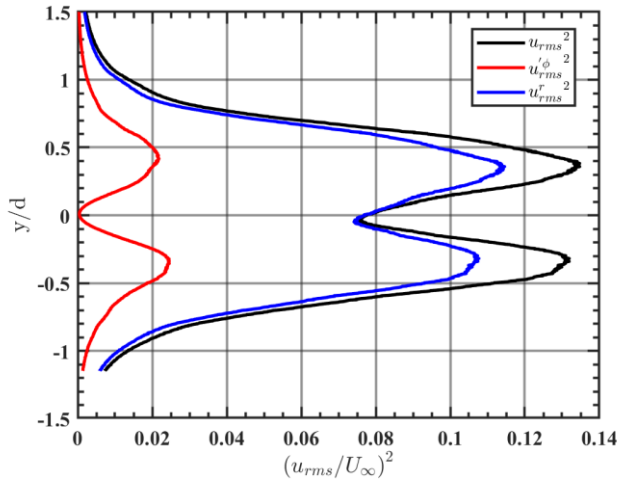

Figure 74. Decomposition of the fluctuating streamwise velocity energy for smooth cylinder at Re_d=1800 measured at $x/d = 4.1$.

As discussed earlier, the case of the smooth cylinder at $Re_d = 2500$ is believed to have the characteristics of the flow Regime 1. Figure 75 demonstrates the $< u' >$ profiles for this case at every other phase bin. The periodic passing of a counter-rotating vortex pair is evident in this figure where the velocity profiles at phases $\phi = 0$ and 0.5 qualitatively resemble the velocity profiles of vortices with clockwise and counter clockwise rotation, respectively. The PSD corresponding to this case shown in Figure 71 shows a narrow and strong harmonic peak, which along with the phase average velocity profiles, suggest a recovery of the von Karman vortex formation and shedding organization from Regime 2 after increasing the Reynolds number from 1800 to 2500.

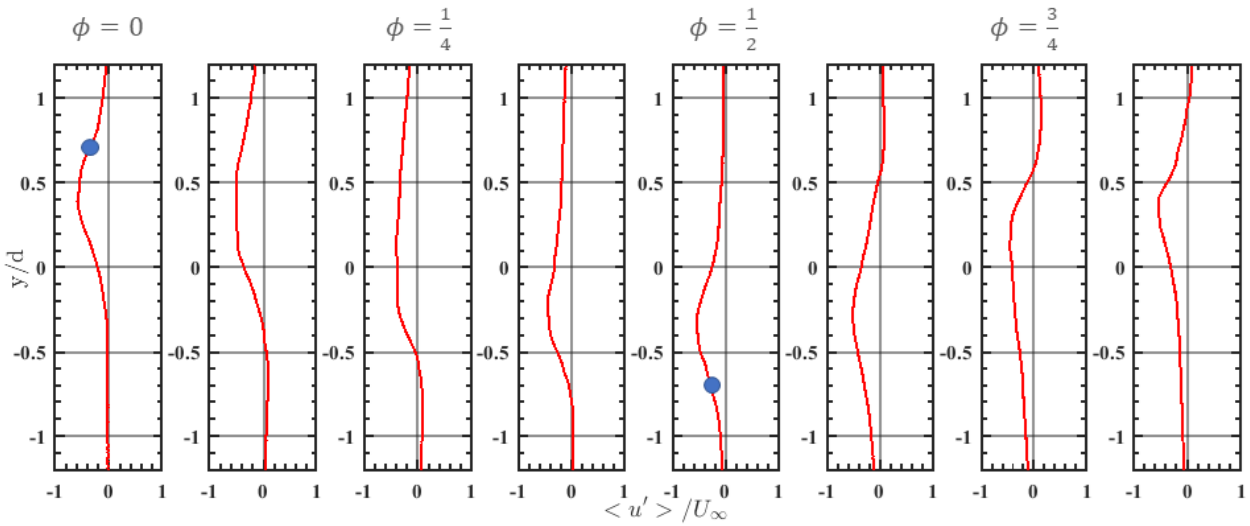

Figure 75.$< u' > /U_\infty$ at different phases measured $1d$ downstream of the formation length at $x/d = 3.4$. Smooth cylinder at $Re_d = 2500$. Maximum positive and negative gradient locations are marked at $\phi = 0$ and 0.5.

The fluctuating streamwise velocity energy is decomposed and shown in Figure 76 for this case. This figure shows that the amount of the energy carried by the coherent von Karman vortex shedding is roughly the same as the that carried by the remaining fluctuations. Although the coherent component carries higher energy compared to the case of $Re_d = 1800$, the recovery of the vortex shedding organization is not as good as for the $Re_d = 800$ case.

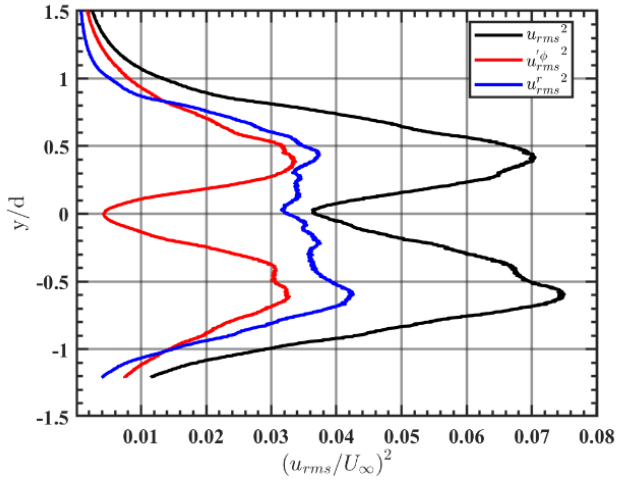

Figure 76. Decomposition of the fluctuating streamwise velocity energy for smooth cylinder at Re_d=2500 at $x/d = 3.4$.

It is also interesting to consider Regime 3 behavior as exemplified by the 2Dp-5% cylinder at $Re_d = 2500$ (see Figure 65). The phase-averaged velocity profiles at every other phase for this case are depicted in Figure 77. Almost no variation of the velocity profiles can be distinguished over different phases, and there is no distinct signature of a counter-rotating vortex shedding. The PSD for this case in Figure 71 shows a peak that is about an order of magnitude weaker than the other cases and is distributed over a wider frequency band. Therefore, it is not surprising that the phase-averaged velocity profiles do not vary significantly from the mean velocity profile, as the coherent structures are very weak.

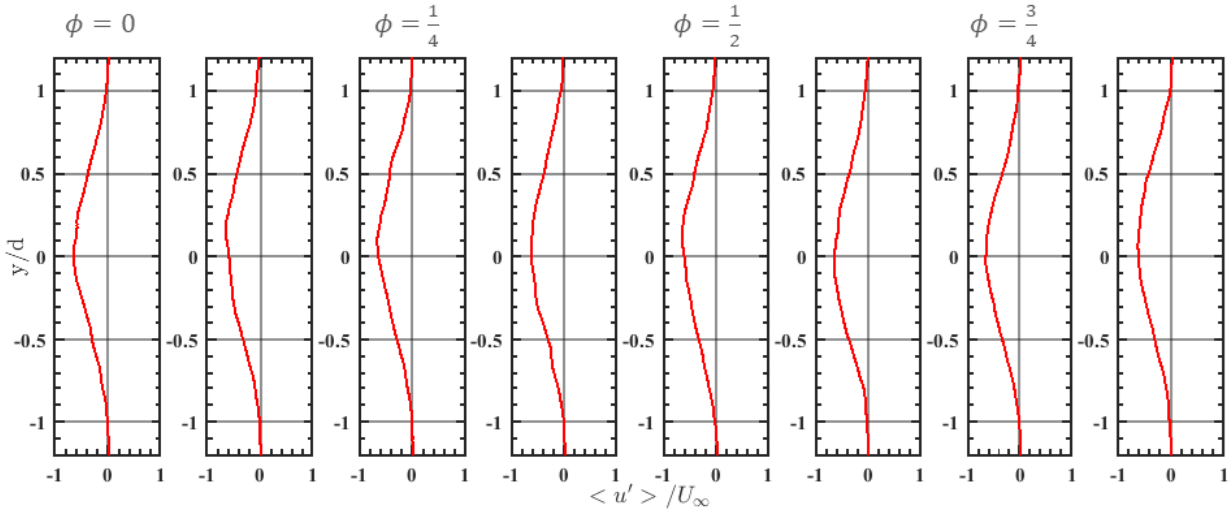

Figure 77. $< u' > /U_\infty$ at different phases measured $1d$ downstream of the formation length at $x/d = 3.8$. 2Dp cylinder at $Re_d = 2500$.

To ascertain this, energy decomposition of the fluctuating velocity is performed and portrayed in Figure 78. It can be seen that the energy carried by the coherent structures associated with von Karman vortex shedding is negligible. Therefore, the wake seems to be significantly turbulent in this regime and there is no persuasive sign of a coherent and organized wake vortex shedding structure.

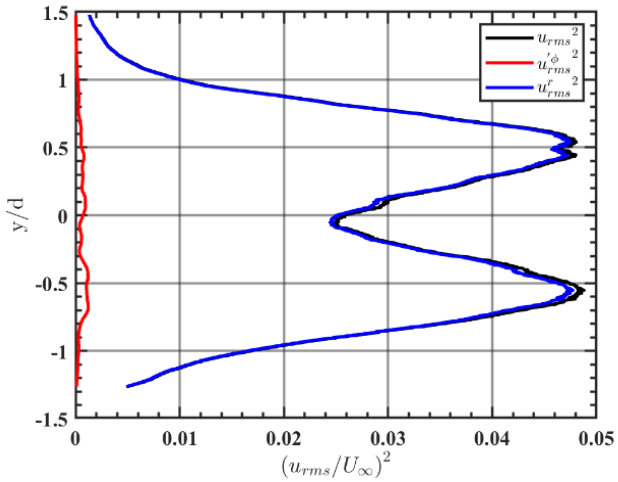

Figure 78. Decomposition of the fluctuating streamwise velocity energy for 2Dp cylinder at Re_d=2500 at $x/d = 3.8$.

The ratio of the phase-average to the total energy at the y location of the maximum u_{rms}^2 is tabulated for the different cases in Table 4. The higher this ratio is, the more repeatable is the vortex shedding from cycle to cycle.

Table 4. Comparison of the ratio of the energy of the phase-average velocity to the total energy of the velocity fluctuations.

	smooth, $Re_d = 800$	smooth, $Re_d = 1800$	smooth, $Re_d = 2500$	2Dp, $Re_d = 2500$
${u'}_{rms}^{\phi\ 2}/{u_{rms}}^2\%$	87%	18%	46%	3%

Inspection of Table 4 shows that Regime 1 has the highest cycle-to-cycle repeatability of the phase average, meaning that the attached/laminarly reattached flow has the best organized wake vortex shedding. Wake vortex shedding is weakly organized, but distinguishable at the transition regime between Regimes 1 and 2, where the separation bubble opens up without vortex formation above the cylinder sidewall, but closes occasionally. The worst repeatability belongs to Regime 3, where there is practically no sign of wake vortex formation. In this case, the shear layer vortex formation upstream of the wake seems to promote turbulent reattachment. However, these vortices seem to disrupt organized wake vortex formation.

Chapter 6. Conclusions

This study experimentally investigates the effect of surface topology and Reynolds number on the fluid flow around a rectangular cylinder with round corners. The main motivation is the recent discovery of the underlying cause of flow-induced vibration that complicates the controllability and compromises the landing accuracy of Precision Airdrop Systems (PADS). It is recently found that the suspension lines of PADS, the shape of which may be approximated as a rectangular cylinder with complex surface geometry, undergo galloping instability: a type of flow-induced vibration seen in non-circular cross-section cylinders. To systematically investigate the effect of the surface geometry, a surface topology is mathematically defined using spatial Fourier modes with parameters closely representing the geometry of the PADS suspension lines. The topology is superposed onto a baseline shape of a smooth-surface rectangular cylinder with fully-round leading and trailing edges.

The study examines the influence of various aspects of surface topology, including amplitude, variation along the span, and orientation relative to the oncoming flow, on the boundary layer and the near-wake flow around a rectangular cylinder. Models with surface topology include topology orientations with a peak or a valley at the leading edge but no variation along the span: these are referred to as 2Dp and 2Dv cases. Cylinders with similar topology but with variation along the span are also examined. In these cases, measurements are done at two planes along the spans, aligned with cross-sections corresponding to largest peak and valley at the leading edge (3Dp and 3Dv cases, respectively). The studied rage of Reynolds numbers, based on the cylinder thickness, is from $Re_d = 800 - 2500$. Utilizing single-component molecular tagging velocimetry (1c-MTV), the research is based on measurements of the streamwise velocity and visualization of the flow field at various locations above the surface and in the wake of the cylinder.

1c-MTV measurement of the mean and rms velocity profiles in the boundary layer of the cylinders reveal that the orientation of the surface topology to the oncoming flow plays a significant role in determining the behavior of the boundary layer. For the specific topology wavelength utilized, the most notable impact occurs when the topology is associated with a peak at the leading edge of the cylinder. In this scenario, a considerably thicker separation zone forms, and the separated shear layer becomes thicker, positioned farther away from the cylinder. Additionally, the shear layer displays the highest level of unsteadiness compared to the smooth cylinder and the cylinder section where a valley is present at the leading edge. Moreover, the effect of surface topology on the separated shear layer behavior is Reynolds number dependent and this dependency is non-monotonic. The effect of topology amplitude is also studied and is seen to generally magnify the deviation of the boundary layer behavior from that of the baseline. Presence of the surface topology variation along the span decreases the separation zone thickness for the cross-sections with a peak at the leading edge, but does the opposite for the cross-sections with a valley at the leading edge. The latter case excludes the high end of the tested Reynolds numbers ($Re_d = 2500$). A monotonic trend does not exist when comparing the fluctuating velocity in the shear layer for these cases.

The separation zone boundaries on the top and bottom surfaces are further studied for the geometries with surface topology amplitude $\varepsilon/d = 5\%$ at several angles of attack from $\alpha = 0° - 2°$ to infer stability to galloping based on the quasi-steady assumption, and to compare the results against force measurements using similar geometries in other studies. In general, it is observed that the introduction of surface topology can lead to earlier separation of the boundary layer on the cylinder, occurring farther upstream compared to the smooth baseline geometry. This phenomenon is evident in both the 2Dp case and when measuring in a spanwise plane with a peak at the leading

edge in the 3D geometry. The present study draws on existing knowledge in the literature regarding galloping to interpret the identified boundary layer behavior and hypothesize that the promotion of earlier separation due to surface topology has a destabilizing effect on galloping. However, this destabilizing influence is counteracted by the stabilizing effect of the reattachment of the shear layer, which is promoted by the presence of spanwise variation in the topology (3D geometry) and increasing Reynolds number. The Reynolds number effect, as inferred from the separation and reattachment characteristics of the top-surface shear layer, is consistent with the recent force data studies on similar geometries.

Investigating the wake flow for the cylinders with smooth surface as well as surface topologies with 5% amplitude at $\alpha = 0°$ reveals that the case of 2Dp-5% has the biggest deviation in the mean and fluctuating wake flow characteristics from the other geometries. In addition, non-monotonic Reynolds number dependency of the wake behavior is also seen across the geometries. Overall, altering the initial wake width and the maximum transverse separation of the shear layers plays a crucial role in surface topology's influence on the vortex shedding frequency. It is specifically seen that the vortex shedding frequency scales better with the wake than with the cylinder width. The wake width variation among different cases stem from changes in the boundary layer separation/reattachment on the cylinder's surface.

Finally, the unsteady behavior of the boundary layer and the wake of the smooth cylinder at $\alpha = 0°$ is studied at different Reynolds numbers. The results reveal different progression of boundary layer separation/reattachment flow regimes with increasing Reynolds number compared to the widely studied sharp-corner cylinder. Despite this different progression, the boundary layer-wake flow relationship is generally consistent with the literature understanding of the sharp-corner cylinder, where Strouhal number and organization of the wake vortex shedding is affected by the

boundary layer separation/reattachment characteristics. An exception to this agreement is found at the highest Reynolds number of 2500, where reattachment of the shear layer does not produce an increase in Strouhal number.

Transition in the shear layer upstream of reattachment of the boundary layer is not observed for the smooth cylinder in the studied Reynolds number range, but is detected for some geometries with surface topology. As a sample result, boundary layer and near-wake flow visualization for the 2Dp-5% case reveals that shear layer vortex formation occurs above the side surface of the cylinder, promoting reattachment. Phase-average velocity analysis of these cases demonstrate sensitivity of the vortex shedding organization to different flow regimes. Specifically, the best organized wake vortex shedding is observed for the attached/laminarly reattached boundary layer flow. Wake vortex shedding is weakly organized but identifiable for the regime with intermittent reattachment of the boundary layer, while reattachment due to transition in the shear layer (2Dp-5% case) exhibits the least organized and barely observable wake vortex shedding. In this scenario, shear layer vortex formation upstream of the wake appears to facilitate turbulent reattachment. However, these vortices also appear to disrupt the organization of wake vortex shedding.

For future research, investigating the impact of surface topology amplitude on the galloping-related boundary layer behavior of 3D surface topologies would be advantageous. Additionally, an analysis of the spanwise velocity can offer deeper insights into the flow behavior over the surfaces of the cylinders with 3D surface topology. Furthermore, building upon the findings of this study, it would be worthwhile to examine the flow regime over the cylinders at various other Reynolds numbers to explore the presence of different flow regimes.

BIBLIOGRAPHY

[1] K. Bergeron, D. Ecklebe, K. McClure, H. Johari, T. Curlett, and B. Pitman, "Parachute suspension line drag analysis," 2009, p. 2982.

[2] T. Siefers, K. Greene, T. McLaughlin, and K. Bergeron, "Wind and water tunnel measurements of parachute suspension line," 2013, p. 64.

[3] R. D. Blevins, "Flow-induced vibration," *New York*, 1977.

[4] G. Parkinson, "Phenomena and modelling of flow-induced vibrations of bluff bodies," *Progress in Aerospace Sciences*, vol. 26, no. 2, pp. 169-224, 1989.

[5] A. Okajima, "Strouhal numbers of rectangular cylinders," *Journal of Fluid mechanics*, vol. 123, pp. 379-398, 1982.

[6] R. Parker and M. C. Welsh, "Effects of sound on flow separation from blunt flat plates," *International Journal of Heat and Fluid Flow*, vol. 4, no. 2, pp. 113-127, 1983.

[7] M. A. Feero, A. M. Naguib, and M. M. Koochesfahani, "Effect of surface topology on the galloping instability of rectangular cylinders," *International Journal of Heat and Fluid Flow*, vol. 86, p. 108721, 2020.

[8] M. A. Feero, A. M. Naguib, and M. M. Koochesfahani, "Surface topology effects on the transverse galloping behavior of rectangular cylinders," in *11th International Symposium on Turbulence and Shear Flow Phenomena (TSFP 11)*, 2019.

[9] M. A. Feero, A. M. Naguib, and M. M. Koochesfahani, "Influence of geometry on the galloping instability of rectangular cylinders in the Reynolds number range 1,000–10,000," *Journal of Fluids and Structures*, vol. 94, p. 102881, 2020.

[10] L. Carassale, A. Freda, and M. Marre-Brunenghi, "Experimental investigation on the aerodynamic behavior of square cylinders with rounded corners," *Journal of Fluids and Structures*, vol. 44, pp. 195-204, 2014.

[11] K. Kalan, A. Safaripour, A. M. Naguib, and M. M. Koochesfahani, "Characterization of the aerodynamics of rectangular cylinders with surface topology," 2021, p. 1322.

[12] K. Kalan, "Experimental Investigation of the Surface Topology Influence on the Boundary Layer and Near-Wake Behavior of Rectangular Cylinders," M.S. Project, Michigan State University, 2020.

[13] T. M. Siefers, "Flow and Vibration Analysis of Parachute Suspension Line," *University of Colorado Colorado Springs M.S. Thesis*, 2013.

[14] C. P. Gendrich, M. M. Koochesfahani, and D. G. Nocera, "Molecular tagging velocimetry and other novel applications of a new phosphorescent supramolecule," *Experiments in fluids,* vol. 23, no. 5, pp. 361-372, 1997.

[15] M. M. Koochesfahani and D. G. Nocera, "Molecular tagging velocimetry," *Handbook of experimental fluid dynamics,* pp. 362-382, 2007.

[16] C. P. Gendrich and M. M. Koochesfahani, "A spatial correlation technique for estimating velocity fields using molecular tagging velocimetry (MTV)," *Experiments in Fluids,* vol. 22, no. 1, pp. 67-77, 1996.

[17] L. H. Benedict and R. D. Gould, "Towards better uncertainty estimates for turbulence statistics," *Experiments in fluids,* vol. 22, no. 2, pp. 129-136, 1996.

[18] M. S. H. Boutilier and S. Yarusevych, "Separated shear layer transition over an airfoil at a low Reynolds number," *Physics of Fluids,* vol. 24, no. 8, p. 084105, 2012.

[19] L. M. Hudy, A. Naguib, and W. M. Humphreys, "Stochastic estimation of a separated-flow field using wall-pressure-array measurements," *Physics of Fluids,* vol. 19, no. 2, p. 024103, 2007.

[20] N. Djilali and I. S. Gartshore, "Turbulent flow around a bluff rectangular plate. Part I: Experimental investigation," 1991.

[21] E. Naudascher and D. Rockwell, *Flow-induced vibrations: an engineering guide*. Courier Corporation, 2012.

[22] R. L. Panton, *Incompressible flow*. John Wiley & Sons, 2013.

[23] P. W. Bearman, "Investigation of the flow behind a two-dimensional model with a blunt trailing edge and fitted with splitter plates," *Journal of fluid mechanics,* vol. 21, no. 2, pp. 241-255, 1965.

[24] O. M. Griffin, "A note on bluff body vortex formation," *Journal of Fluid mechanics,* vol. 284, pp. 217-224, 1995.

[25] J. W. Schaefer and S. Eskinazi, "An analysis of the vortex street generated in a viscous fluid," *Journal of Fluid Mechanics,* vol. 6, no. 2, pp. 241-260, 1959.

[26] A. Fage and F. C. Johansen, "XLII. The structure of vortex sheets," *The London, Edinburgh, and Dublin Philosophical Magazine and Journal of Science,* vol. 5, no. 28, pp. 417-441, 1928.

[27] A. Roshko, "On the drag and shedding frequency of two-dimensional bluff bodies," 1954.

[28] I. G. Currie, *Fundamental mechanics of fluids*. CRC press, 2016.

[29] C. Norberg, "Flow around rectangular cylinders: pressure forces and wake frequencies," *Journal of wind engineering and industrial aerodynamics,* vol. 49, no. 1-3, pp. 187-196, 1993.

[30] A. K. M. F. Hussain and W. C. Reynolds, "The mechanics of an organized wave in turbulent shear flow," *Journal of Fluid mechanics,* vol. 41, no. 2, pp. 241-258, 1970.

APPENDIX

The MATLAB code to generate the surface topology is enclosed here. It consists of a main script and a function.

```
clear;
clc;
dx = .01;    %interval
l =  139.6;      %span

for z = 1:(l/dx)+1
coor(z) = {topol2((z-1)*dx)};
end

B = cell2mat (coor)';

csvwrite('rotate.txt',[B(:,1,:),B(:,2,:),B(:,3,:)])

p_mid = round(numel(B(:,1))/2);

range = (B(:,2)>0);

x_surface = B(:,1);
y_surface = B(:,2);
z_surface = B(:,3);

x_s = reshape(x_surface,1900,[]);
y_s = reshape(y_surface,1900,[]);
z_s = reshape(z_surface,1900,[]);

figure
s=surf(x_s,z_s,y_s)
s.EdgeColor = 'none';
axis on
l = light('Position',[-50 -15 29])
set(gca,'CameraPosition',[208 -50 7687])
lighting phong
shading interp
colorbar EastOutside
```

```
function [finalcoordinates] = topol2(z)

sr = 2.5; %side ratio
d = 1.5;  %chord
c = d*sr; %diameter
l = 139.6; % span
r = 0.5*d; %corner radius
es = 0.05*d;   %topology amplitude
cycle = 10; %number of wavelengths around the perimeter
p = 2*(c+d) + r*(2*pi-8); %perimeter of the baseline
lamx = p/cycle; %wavelength around the perimeter
lamz = lamx*1.5;   %wavelength along the span
gama = atan (lamz / lamx);
phi = 2*pi*z/lamz; %phase of the topology at 0
dx = 0.0020;    %interval
dt = dx / r;

%% 1

y1 = 0:dx:d/2-r;
x1 = zeros(size(y1)) ;
s1 = y1;
cosarc = es * (cos(2*pi*cycle*s1/p + phi) + cos(2*pi*cycle*s1/p
- phi));
n1=[zeros(size(y1))-1;zeros(size(y1))];
xt1 = -cosarc + x1 - c/2;
yt1 = y1;

eptest1 = sqrt( (xt1 - x1 +c/2).^2 + (yt1 - y1).^2);

%% 2
 t2 = pi-dt:-dt:pi/2;
 x2 = r * cos(t2) ;
 y2 = r * sin(t2) ;
 s2 = d/2-r + r * (pi-t2);
 n2 = [cos(t2);sin(t2)];
 a = [x2 ; y2];
 f2 = es *(cos(2*pi*cycle*s2/p + phi) + cos(2*pi*cycle*s2/p -
phi));
 cosarc = (f2 .* n2) + a;
 xt2 = cosarc(1,:) - c/2 + r;
 yt2 = cosarc(2,:) + d/2 - r;

 eptest2 = sqrt( ((xt2+ c/2 - r - x2).^2) + ((yt2-d/2 +r -
y2).^2));
```

```
%% 3
x3 = -c/2+r +dx : dx :c/2-r   ;
y3 = zeros(size(x3));
s3 = d/2-r +r*pi/2 + x3 + c/2 - r;
cosarc3 = es * (cos(2*pi*cycle*s3/p + phi) + cos(2*pi*cycle*s3/p
- phi));

n3 = [zeros(size(x3));zeros(size(x3))+1];

xt3 = x3;
yt3 = cosarc3 + d/2;
eptest3 = sqrt( (xt3 - x3).^2 + ((yt3-d/2 - y3).^2));

%% 4
t4 = pi/2 -dt:-dt:0;
 x4 = r * cos(t4) ;
 y4 = r * sin(t4) ;
 s4 = d/2-r +r*pi/2 +c - 2*r + r * (pi/2-t4);
 n4 = [cos(t4);sin(t4)];
 a = [x4 ; y4];
 f4 = es * (cos(2*pi*cycle*s4/p + phi) + cos(2*pi*cycle*s4/p -
phi));
 cosarc = (f4 .* n4) + a;
 xt4 = cosarc(1,:) + c/2 - r;
 yt4 = cosarc(2,:) + d/2 - r;

 eptest4 = sqrt( ((xt4-c/2+r - x4).^2) + ((yt4-d/2+r - y4).^2));

%% 5

y5 = d/2-r -dx:-dx:-d/2+r;
x5 = zeros(size(y5)) ;
s5 = d/2-r +r*pi +c - 2*r - y5 +d/2 -r;
cosarc = es * (cos(2*pi*cycle*s5/p + phi) + cos(2*pi*cycle*s5/p
- phi));
n5=[zeros(size(y5))+1;zeros(size(y5))];
xt5 = cosarc + x5 + c/2;
yt5 = y5;

eptest5 = sqrt( (xt5 - x5-c/2).^2 + (yt5 - y5).^2);

%% 6

t6 = 0-dt:-dt:-pi/2;
 x6 = r * cos(t6) ;
 y6 = r * sin(t6) ;
 s6 = d/2-r +r*pi +c - 2*r +d -2*r - r * t6;
```

```
 n6 = [cos(t6);sin(t6)];
 a = [x6 ; y6];
 f6 = es * (cos(2*pi*cycle*s6/p + phi) + cos(2*pi*cycle*s6/p -
phi));
 cosarc = (f6 .* n6) + a;
 xt6 = cosarc(1,:) + c/2 - r;
 yt6 = cosarc(2,:) - d/2 + r;
 eptest6 = sqrt( (xt6-c/2+r - x6).^2 + (yt6+d/2 -r - y6).^2);

%% 7

x7 = c/2-r -dx: -dx :-c/2+r   ;
y7 = zeros(size(x7));
s7 = d/2-r +r*pi*3/2 +c - 2*r +d -2*r - x7 + c/2 - r;
cosarc7 = es * (cos(2*pi*cycle*s7/p + phi) + cos(2*pi*cycle*s7/p
- phi));

n7 = [zeros(size(x7));zeros(size(x7))-1];

xt7 = x7;
yt7 = -cosarc7 - d/2;
eptest7 = sqrt( (xt7 - x7).^2 + ((yt7+d/2 - y7).^2));


%% 8

t8 = -pi/2-dt:-dt:-pi;
 x8 = r * cos(t8) ;
 y8 = r * sin(t8) ;
 s8 = d/2-r +r*pi*3/2 +c - 2*r +d -2*r + c - 2*r + r * (-pi/2 -
t8);
 n8 = [cos(t8);sin(t8)];
 a = [x8 ; y8];
 f8 = es * (cos(2*pi*cycle*s8/p + phi) + cos(2*pi*cycle*s8/p -
phi));
 cosarc = (f8 .* n8) + a;
 xt8 = cosarc(1,:) - c/2 + r;
 yt8 = cosarc(2,:) - d/2 + r;

 eptest8 = sqrt( ((xt8+c/2 - r - x8).^2) + ((yt8+d/2 - r -
y8).^2));

%% 9

y9 = -d/2+r+dx:dx:0;
x9 = zeros(size(y9));
s9 = d/2-r +r*pi*2 +c - 2*r +d -2*r + c - 2*r + y9 + d/2 -r;
```

```
cosarc = es * (cos(2*pi*cycle*s9/p + phi) + cos(2*pi*cycle*s9/p
- phi));
n9=[zeros(size(y9))-1;zeros(size(y9))];
xt9 = -cosarc - c/2;
yt9 = y9;

eptest9 = sqrt( (xt9 - x9+c/2).^2 + (yt9 - y9).^2);

xtot=[xt1,xt2,xt3,xt4,xt5,xt6,xt7,xt8,xt9];
ytot=[yt1,yt2,yt3,yt4,yt5,yt6,yt7,yt8,yt9];
x_n = [x1,x2,x3,x4,x5,x6,x7,x8,x9];
y_n = [y1,y2,y3,y4,y5,y6,y7,y8,y9];
stotal = [s1,s2,s3,s4,s5,s6,s7,s8,s9];
stotal(1)
stotal(end)
ntotal = [n1,n2,n3,n4,n5,n6,n7,n8,n9];
epstesttotal =
[eptest1,eptest2,eptest3,eptest4,eptest5,eptest6,eptest7,eptest8
,eptest9];
ftotal = es * cos(2*pi*cycle*stotal/p + phi);
sur_face = (ftotal .* ntotal) + ntotal *r;
ztot=zeros(size(xtot)) + z;
finalcoordinates = [xtot;ytot;ztot];

end
```